# SPIN DYNAMICS IN MAGNETIC THIN FILMS AND SPINTRONICS DEVICES

by

Yunpeng Chen

A dissertation submitted to the Faculty of the University of Delaware in partial fulfillment of the requirements for the degree of Doctor of Philosophy in Physics

Spring 2016

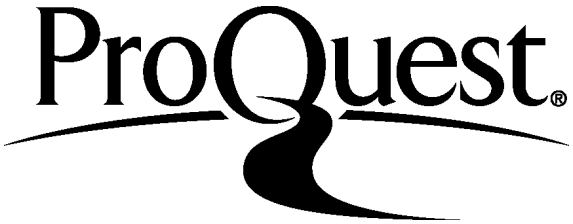

**SPIN DYNAMICS IN MAGNETIC THIN FILMS AND SPINTRONICS DEVICES**

by

Yunpeng Chen

Approved: _____
Edmund R. Nowak, Ph.D.
Chair of the Department of Physics and Astronomy

Approved: _____
George H. Watson, Ph.D.
Dean of the College of Arts and Sciences

Approved: _____
Ann L. Ardis, Ph.D.
Senior Vice Provost for Graduate and Professional Education

I certify that I have read this dissertation and that in my opinion it meets the academic and professional standard required by the University as a dissertation for the degree of Doctor of Philosophy.

Signed: _____

John Q. Xiao, Ph.D.
Professor in charge of dissertation

I certify that I have read this dissertation and that in my opinion it meets the academic and professional standard required by the University as a dissertation for the degree of Doctor of Philosophy.

Signed: _____

Matthew Doty, Ph.D.
Member of dissertation committee

I certify that I have read this dissertation and that in my opinion it meets the academic and professional standard required by the University as a dissertation for the degree of Doctor of Philosophy.

Signed: _____

Yi Ji, Ph.D.
Member of dissertation committee

I certify that I have read this dissertation and that in my opinion it meets the academic and professional standard required by the University as a dissertation for the degree of Doctor of Philosophy.

Signed: _____

Stanley Owocki, Ph.D.
Member of dissertation committee

## ACKNOWLEDGMENTS

First of all, I would like to thank my adviser, Professor John Q. Xiao, for all his guidance, encouragement and inspiration throughout the entire course of my Ph.D. study. It is an excellent opportunity to study physics and conduct creative researchers. What I have learned from him are not only the knowledge, but also the ways to attach problems, taking the responsibility and how to work independently.

My sincere gratitude also goes to Dr. Xin Fan and Professor Siu-Tat Chui for their tremendous theoretical contribution to this work and the stimulus discussions.

I am thankful to my thesis committee, Dr. John Q. Xiao, Dr. Matthew Doty, Dr. Yi Ji and Dr. Stanley Owocki, who peer reviewed my dissertation and gave me valuable feedbacks.

I would like to thank all my colleagues and collaborators, including Dr. Yi Ji, Dr. Edmund Nowak, Dr. Stephanie Law, Dr. Matthew Doty, Dr. Rainee N. Simons, Dr. Jeffrey D. Wilson, Dr. Christian Binek, Dr. Ilya Krivorotov, Dr. Qi Lu, Dr. Xiaoming Kou, Dr. Yang Zhou, Dr. Xinran Zhou, Jun Wu, Yunsong Xie, Harsha Kannan, Tao Wang, Halise Celik, Asif Warsi, Rasoul Barri, Shoaib Khalid, Hang Chen, Chuan Qin, Yunjiao Cai, Kevin Haughey, Theresa Ginley. I also want to thank all staff members in Physics Department, most notably Maura Perkins and Debra Morris, for their kindly help.

Finally, I wish to thank my parents for their love and support. I owe my sincere regards to my dear wife, Mengting Du, without whom I would not able to finish my Ph.D. study.

## TABLE OF CONTENTS

Appendix

## LIST OF TABLES

## LIST OF FIGURES

## ABSTRACT

Magnetic materials are the essential parts of advanced magnetic recording and microwave devices. All the applications require the control of the magnetization orientation that is studied as magnetic dynamics.

In a magnetic recording device, such as hard disk drive (HDD), the digital information is stored as the magnetization direction of magnetic domains. To rewrite the information, one needs to reverse the magnetization. With the increase of areal density, the magnetic anisotropy is enhanced to overcome the thermal fluctuations. Consequently, the magnetic switching becomes more difficult. Microwave assisted magnetization reversal (MAMR) is developed to lower the switching field by exciting large angle precession of magnetization. Damping constant, as a parameter describing the dissipation of magnetic materials, plays a critical role in MAMR. In this thesis, I theoretically and experimentally study the damping dependence of MAMR in micro-size magnetic dots. Based on the study, MAMR is more efficient when the damping of the magnetic dot is small.

Magnetic random access memory (MRAM) based on magnetic tunnel junctions (MTJs) is a novel magnetic recording device that has the potential to replace HDD due to its fast read/write rate. Moreover, to keep increasing the recording density, the magnetic media with perpendicular magnetic anisotropy (PMA) replaced the in-plane magnetic recording media. In this work, the magnetic thin films such as Co/Pd multilayers and Ta/CoFeB/MgO were fabricated to be with PMA. Based on the PMA thin films, the MTJs were developed with optimized deposition conditions and post-

annealing. We observed above 60% TMR in Ta/CoFeB/MgO/CoFeB based perpendicular junctions. The voltage controlled magnetic anisotropy (VCMA) was demonstrated in those MTJs, which is an efficient technique to control the magnetization via an electric field. The spin transfer torques were also characterized in Ta/CoFeB/MgO structures with PMA.

The microwave response is another useful property of magnetic materials. The ferromagnetic resonance (FMR) of typical ferromagnetic materials like Fe, Co, Ni and their alloys are in the gigahertz range. Therefore, the magnetic thin films have been widely utilized in microwave devices such as bandpass filters, insulators, and oscillators. Conventionally, electromagnets generate a magnetic field to control the resonance frequency, which is bulky, noisy, slow and energy consuming. By realizing the huge effective field due to exchange interaction, a novel scheme was demonstrated to shift the resonance frequency of the optical mode in magnetic bilayers with interlayer exchange interaction. A maximum 20 GHz tunable range was achieved in a spin-valve base spintronics microwave device in the experiment. A dynamic tuning of the resonance frequency as high as 9 GHz was demonstrated via temperature controlled exchange interaction.

# Chapter 1

# INTRODUCTION

Magnetism is an ancient science. For centuries, people have known certain natural materials, like loadstone and iron, that attract or repel each other. In ancient China, people first invented magnetic needle compass for navigation in the 11$^{th}$ century. The origin of magnetism was still a mystery until the 19$^{th}$ century. In 1819, Hans Oersted observed an electric current could affect a compass needle, implying an electric current can generate a magnetic field. After that, scientists, such as André-Marie Ampère, Carl Friedrich Gauss, Jean-Baptiste Biot, and Michael Faraday, discovered the link between magnetism and electricity in various aspects. Finally, the relationship between magnetism and electricity was completely revealed in Maxwell's equations, named after James Clerk Maxell, who developed these equations in between 1861 and 1862. Electric current as a source of magnetism, the well-known charge carriers, electrons, were found to carry intrinsic spin magnetic moments during the early development of quantum physics in 1920's. More recently, the duality of charge and spin of electrons give rise to a remarkably broad and fertile research area as spintronics (a portmanteau meaning spin electronics) that explores the interplay between spin and charge properties of the electron. In past 30 years, the research in spintronics keeps reinventing itself and germinates new research areas and applications.

One of the most important phenomena in spintronics is the spin-dependent electronic transport [1] that gave the birth to the advanced magnetics memory devices such as hard disk drive [2, 3]. In a hard disk drive (HDD), the bit information is

encoded as the magnetization orientation of magnetic grains on a disk. The information stored in an HDD is non-volatile since the magnetization orientation is stable in the power-off state. A recording head flies over the disk at a distance of a few nanometers to detect the magnetic direction of the magnetic bits and rewrite the information via switching the magnetization direction through the magnetic field generated by a ring-shaped electromagnet. The areal recording density has dramatically increased from 2 Kbit/in$^2$ in 1956 to 1.34 Tbit/in$^2$ in 2015 [4] with the development of spintronics. The conventional recording media, made of magnetic materials with in-plane magnetic anisotropy, was recently replaced by materials with perpendicular magnetic anisotropy [5-7], which theoretically has more recording density. The primary challenge to keep increasing the recording density is due to the competing requirements of readability, writeability, and stability. With the reduction in bit size, the magnetic anisotropy energy density, which stabilizes the magnetization orientation, needs to be increased to satisfy the thermal stability following $KV > 50 - 60k_BT$, where $K$ is the anisotropy energy per unit volume, $V$ is the volume of a bit, $k_B$ is the Boltzmann constant, and $T$ is the temperature. The increase in the magnetic anisotropy energy density will make it difficult to rewrite the information because the switching field is also proportional to the energy barrier as $H_c \propto KV$. One solution is to apply microwaves during the writing process to help to switch the bit, which is known as microwave-assisted magnetic recording [8-11]. Understanding the role of magnetic properties in the reversal process is crucial to optimize the efficiency of microwaves. The study in this thesis will provide more insights into the issue.

Comparing with relatively slow read-write speed (millisecond) of hard disk drive due to the mechanical movement of the recording head in the read/write

procedures, random access memories (RAMs) [12] allows faster processing speed (nanosecond) to match the operation rate of computer processors. However, almost all commercial RAMs are volatile which means an electric power is always necessary to keep the information. Therefore, developing new memory devices that combine the advantages of HDD and RAMs as cheap, non-volatile, fast-access information storage is seeing serious efforts from both academia and industry. The spin-transfer-torque magnetic RAM (STT-MRAM) [13, 14] is one of the most promising memory techniques. A central element in MRAMs is a magnetic tunnel junction [15-17] that is composed of a thin insulating layer sandwiched between two ferromagnetic electrodes. The electrical resistance of an MTJ, which is bit cell in MRAM, depends on the relative magnetic orientations of the ferromagnetic electrodes. If the magnetic moment in two ferromagnetic electrodes are in parallel, the resistance is low, and this state can represent logic '0'; if the magnetic moment in the two ferromagnetic electrodes are antiparallel, the resistance is high, and the bit means a logic '1'. The reading of the information is accomplished by measuring the resistance of each bit. The spin transfer torque (STT) is a new technique to electrically manipulate the magnetization with high efficiency. When a spin-polarized current, in which the number of electrons with spin-up or spin-down are not the same, flows through a magnetic layer that is not aligned with the net spin direction, the spin-polarized current transfers spin angular momentum to the local magnetization and alters its direction. If the spin polarized current density is high enough, it would eventually reverse the magnetization direction of the magnetic layer. The switching time for a STT-MRAM bit cell is typically 2 ns [18]. To further reduce the energy consumption of magnetic switching, scientists have also proposed voltage controlled magnetism in magnetic tunnel junctions [19, 20] and

multiferroic material [21, 22]. In this thesis, we developed high-performance magnetic tunnel junctions with perpendicular magnetic anisotropy and investigated STT in magnetic structures with perpendicular anisotropy.

Since the resonance frequency of a typical ferromagnetic material is in gigahertz range [23], magnetic materials have been widely used in microwave applications such as isolators and circulators [24]. Due to the requirements of increasing bandwidth and high speed, microwave devices operated at higher frequency are in high demands. The traditional method to increase the resonance frequency is to utilize magnetic fields generated by an electromagnet, which is bulky and energy consuming. By realizing the strong exchange interaction inside and between ferromagnetic thin films, we proposed and demonstrate a new method of tuning the magnetic resonance frequency via exchange interaction.

The main results of this thesis are following. (1) A numerical algorithm for solving Landau-Lifshitz-Gilbert (LLG) equation was developed to simulate the time-domain magnetic dynamics in magnetic dots. We measured the microwave-assisted magnetic reversal (MAMR) with microwave transmission technique in magnetic dots with controlled damping constant. From the simulation and experiment, we found the materials with low damping benefit the efficiency of MAMR but increase the noise. (2) The magnetic thin films with perpendicular magnetic anisotropy (PMA) was fabricated. The PMA is manipulated by the thickness of the films and annealing conditions. (3) We demonstrated MgO-based magnetic tunnel junction with PMA. The TMR ratio was optimized to be 60%, through reducing $H_2O$ partial pressure and the sputtering rate of MgO during the growth. We observed a shift of the magnetic anisotropy as 45 Oe, caused by 1 V/nm electric field at the junction. (4) The

spin-orbital torques in Ta/CoFeB/MgO thin films with PMA were quantitatively measured via magneto-optical Kerr effect. The results suggest that the Rashba effect is the primary mechanism to generate the spin-orbital torques in Ta/CoFeB/MgO. (5) The high-frequency optical resonance mode was predicted and observed in the magnetic bilayer. The frequency of the optical mode is highly sensitive to the interlayer exchange interaction. Based on such effect, a tunable spintronics microwave detector was achieved with a frequency range of 9 GHz. This tuning range is the largest among the reported results. (6) An analytical solution of the LLG equation was developed to find the dispersion relation and magnetic susceptibility of the magnetic bilayer.

This thesis is organized as follows. Chapter 2 introduces some fundamental concepts and theories of magnetic dynamics and spintronics devices. Then we discuss the detailed sample fabrication and characterization techniques in Chapter 3. Chapter 4 consists of the investigation of the microwave assisted magnetic reversal. Chapter 5 discuss the fabrication of the magnetic multilayers as well as tunnel junctions with perpendicular magnetic anisotropy. The research on quantifying the spin-orbital torques is presented in Chapter 6. In Chapter 7, we predict and demonstrate the enhancement and control of the magnetic resonance frequency in magnetic bilayer via exchange interaction.

## REFERENCES


[1] S. Maekawa and T. Shinjo, Spin dependent transport in magnetic nanostructures: CRC Press, 2002.

[2] P. G. Audia and J. A. Goncalo, "Past success and creativity over time: A study of inventors in the hard disk drive industry," Management Science, vol. 53, pp. 1-15, Jan 2007.

[3] S. N. Piramanayagam and K. Srinivasan, "Recording media research for future hard disk drives," Journal of Magnetism and Magnetic Materials, vol. 321, pp. 485-494, Mar 2009.

[4] T. Register. (10 Apr 2015). IBM claims new areal density record with 220TB tape tech. Available: http://www.theregister.co.uk/2015/04/10/ibm_claims_new_areal_density_record_with_220tb_tape_tech/

[5] A. Moser, K. Takano, D. T. Margulies, M. Albrecht, Y. Sonobe, Y. Ikeda, et al., "Magnetic recording: advancing into the future," Journal of Physics D-Applied Physics, vol. 35, pp. R157-R167, Oct 7 2002.

[6] S. Iwasaki, "PERPENDICULAR MAGNETIC RECORDING," Ieee Transactions on Magnetics, vol. 16, pp. 71-76, 1980 1980.

[7] S. N. Piramanayagam, "Perpendicular recording media for hard disk drives," Journal of Applied Physics, vol. 102, Jul 1 2007.

[8] J.-G. Zhu, X. Zhu, and Y. Tang, "Microwave assisted magnetic recording," Ieee Transactions on Magnetics, vol. 44, pp. 125-131, Jan 2008.

[9] S. Li, B. Livshitz, H. N. Bertram, M. Schabes, T. Schrefl, E. E. Fullerton, et al., "Microwave assisted magnetization reversal in composite media," Applied Physics Letters, vol. 94, May 18 2009.

[10] S. Okamoto, M. Igarashi, N. Kikuchi, and O. Kitakami, "Microwave assisted switching mechanism and its stable switching limit," Journal of Applied Physics, vol. 107, Jun 15 2010.

[11] G. Winkler, D. Suess, J. Lee, J. Fidler, M. A. Bashir, J. Dean, et al., "Microwave-assisted three-dimensional multilayer magnetic recording," Applied Physics Letters, vol. 94, Jun 8 2009.

[12] R. E. Baldwin and P. Krugman, "Market access and international competition: a simulation study of 16K random access memories," National Bureau of Economic Research1986.

[13] Y. Huai, "Spin-transfer torque MRAM (STT-MRAM): Challenges and prospects," AAPPS Bulletin, vol. 18, pp. 33-40, 2008.

[14] A. Khvalkovskiy, D. Apalkov, S. Watts, R. Chepulskii, R. Beach, A. Ong, et al., "Basic principles of STT-MRAM cell operation in memory arrays," Journal of Physics D: Applied Physics, vol. 46, pp. 74001-74020, 2013.

[15] S. Parkin, K. Roche, M. Samant, P. Rice, R. Beyers, R. Scheuerlein, et al., "Exchange-biased magnetic tunnel junctions and application to nonvolatile magnetic random access memory," Journal of Applied Physics, vol. 85, pp. 5828-5833, 1999.

[16] Y. Lee, J. Hayakawa, S. Ikeda, F. Matsukura, and H. Ohno, "Effect of electrode composition on the tunnel magnetoresistance of pseudo-spin-valve magnetic tunnel junction with a MgO tunnel barrier," Applied physics letters, vol. 90, p. 2507, 2007.

[17] S. Ikeda, K. Miura, H. Yamamoto, K. Mizunuma, H. Gan, M. Endo, et al., "A perpendicular-anisotropy CoFeB–MgO magnetic tunnel junction," Nature materials, vol. 9, pp. 721-724, 2010.

[18] M. Hosomi, H. Yamagishi, T. Yamamoto, K. Bessho, Y. Higo, K. Yamane, et al., "A novel nonvolatile memory with spin torque transfer magnetization switching: Spin-RAM," in Electron Devices Meeting, 2005. IEDM Technical Digest. IEEE International, 2005, pp. 459-462.

[19] W.-G. Wang, M. Li, S. Hageman, and C. Chien, "Electric-field-assisted switching in magnetic tunnel junctions," Nature materials, vol. 11, pp. 64-68, 2012.

[20] T. Maruyama, Y. Shiota, T. Nozaki, K. Ohta, N. Toda, M. Mizuguchi, et al., "Large voltage-induced magnetic anisotropy change in a few atomic layers of iron," Nature Nanotechnology, vol. 4, pp. 158-161, 2009.

[21] N. X. Sun and G. Srinivasan, "Voltage control of magnetism in multiferroic heterostructures and devices," in Spin, 2012, p. 1240004.

[22] W. Eerenstein, N. Mathur, and J. F. Scott, "Multiferroic and magnetoelectric materials," nature, vol. 442, pp. 759-765, 2006.

[23] C. Kittel, "On the theory of ferromagnetic resonance absorption," Physical Review, vol. 73, p. 155, 1948.

[24] M. Pardavi-Horvath, "Microwave applications of soft ferrites," Journal of Magnetism and Magnetic Materials, vol. 215, pp. 171-183, 2000.

# Chapter 2

# BACKGROUND OF MAGNETIC RESONANCE AND SPIN-DEPENDENT TRANSPORT

## 2.1 Landau-Lifshitz-Gilbert Equation

The Landau-Lifshitz-Gilbert (LLG) equation is a nonlinear evolution equation that describes how the magnetization in magnetic material changes in magnetic field. When placed in a magnetic field, the electron spin angular momentum and/or orbital angular momentum interact with the magnetic field, leading to Zeeman energy. In ferromagnetic materials, the exchange interaction leads to parallel spin alignment. Additional types of interactions include magnetocrystalline anisotropy, demagnetization field, biquadratic exchange and other weak interactions. By adding all these interactions, one can write down the Hamiltonian of a spin angular momentum $\vec{S}(t)$ as follow

$$H_s = -\frac{g\mu_B\mu_0}{\hbar}\vec{S}\cdot\vec{H} \tag{2.1}$$

where $g$ is the g-factor of the electron, $\mu_B$ is the Bohr magneton, $\mu_0$ is the permeability of vacuum, and $\vec{H}$ is the total effective magnetic field from all interactions described above. Based on the commutation relations of angular momentum, the expectation valve of the spin operator can be expressed as

$$\frac{d}{dt}<\vec{S}(t)>=\frac{g\mu_B\mu_0}{\hbar}<\vec{S}(t)>\times<\vec{H}(t)> \tag{2.2}$$

The magnetization is defined as

$$\vec{M} = \frac{g\mu_B}{\hbar} < \vec{S}(t) > \equiv \gamma < \vec{S}(t) > \tag{2.3}$$

where the gyromagnetic ratio $\gamma = \frac{g\mu_B\mu_0}{\hbar}$ and is equal to 28 GHz/T for the free electron. From Eq. (2.2) and (2.3), one can obtain the evolution equation for magnetization as

$$\frac{d\vec{M}}{dt} = -\gamma[\vec{M}(t) \times \vec{H}(t)] \tag{2.4}$$

The magnetization precesses around the effective field $\vec{H}$ . In reality, the magnetization will finally align with the magnetic field direction due to the dispassion in the material. To describe this empirical fact, one can add an empirical damping term into to Eq. (2.4)

$$\frac{d\vec{M}}{dt} = -\gamma\left[\vec{M}(t) \times \vec{H}(t)\right] + \frac{\alpha}{M_s}\vec{M} \times \frac{d\vec{M}}{dt} \tag{2.5}$$

where $\alpha$ is a dimensionless damping constant and $M_s$ is the saturation magnetization. On the right-hand side of the Eq. (2.5), the first term describes the magnetization precession around magnetic field $\vec{H}$ and the second term describes the dissipation process.

Figure 2.1 shows the schematic configuration of the LLG equation. The precession torque $T_{precession}$ equals to $-\left(\vec{M} \times \vec{H}\right)$is along the tangential direction of the precession corn. The damping torque points to the axis of $\vec{H}$ reducing the precession angle. By substituting the $\frac{d\vec{M}}{dt}$ into the second term on the left-hand side of Eq. (2.5), it can be rewritten as

$$\frac{d\vec{M}}{dt} = -\gamma'\left[\vec{M} \times \vec{H} + \frac{\alpha'}{M_s}\vec{M} \times \left(\vec{M} \times \vec{H}\right)\right] \tag{2.6}$$

with the modified gyromagnetic ratio $\gamma' = \frac{\gamma}{1+\alpha^2}$ and modified damping constant $\alpha' = \frac{\alpha}{1+\alpha^2}$. Eq.(2.6) is known as Landau-Lifshitz (LL) equation. Because the value of $\alpha$ is usually much smaller than 1, $\alpha' \approx \alpha$ and $\gamma' \approx \gamma$. Hence, the gyromagnetic ratio and damping constant are equal in the two expressions of LLG equation.

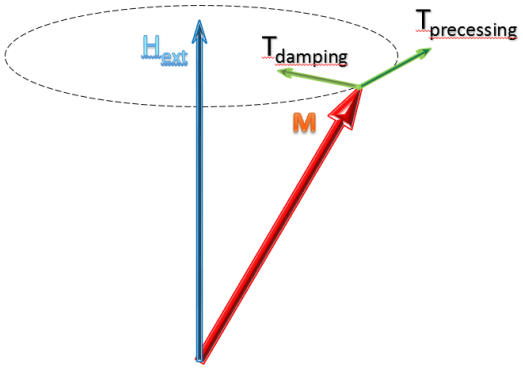


Figure 2.1 Schematics of a magnetization precession

## 2.2 Ferromagnetic Resonance

Ferromagnetic resonance (FMR) is a powerful technique to investigate the magnetic dynamics and characterize magnetic materials. In a single magnetic thin film shown in Figure 2.2 (a), the magnetization is aligned by a small in-plane dc magnetic field $H_{ext}$ in the $z$-axis. We apply small radio-frequency (RF) magnetic fields $h_{rf}e^{i\omega t}$ in the x direction. The magnetization precesses at the same frequency as the RF magnetic field.

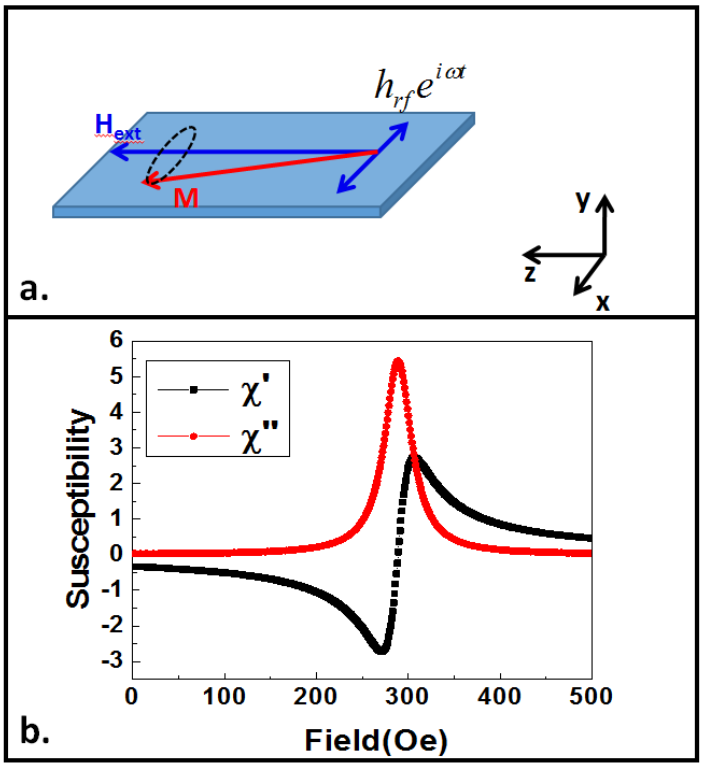


Figure 2.2 (a) Configuration of a magnetization precession excited by RF magnetic field, (b) An example of susceptibility spectrum. The black curve is the real part of susceptibility $\chi'$, and the red curve is the imaginary part of susceptibility $\chi''$.

The magnetic thin film response to the RF magnetic field as a single spin and the precession is uniform throughout the entire film. Considering the demagnetizing field $\mathbf{H}_a$ and magnetic anisotropy $\mathbf{H}_d$, we can write the express of effective field as

$$\mathbf{H} = \mathbf{H}_{ext} + \mathbf{H}_a + \mathbf{H}_d + \mathbf{h}_{rf} e^{i\omega t} \tag{2.7}$$

Because the precession angle is tiny, the $z$ component of the magnetization is an approximate equation for the saturation magnetization. Thus, the magnetization vector can be expressed as

$$\mathbf{M} = (m_x e^{i\omega t}, m_y e^{i\omega t}, M_s) \tag{2.8}$$

where $m_x$ and $m_y$ are the precession amplitude in the $x$ and $y$-direction, respectively.

The magnetic precession relates to the excitation RF magnetic field through a susceptibility tensor as

$$\begin{pmatrix} m_x \\ m_y \end{pmatrix} = \chi \begin{pmatrix} h_{rf} \\ 0 \end{pmatrix} \tag{2.9}$$

Substituting (2.8) and (2.9), into Eq. (2.5), one can drive susceptibility and ferromagnetic resonance frequency as

$$\chi_{xx} = \frac{m_x(t)}{h_{rf}e^{i\omega t}} = \frac{\gamma M_s\left[\gamma H + \gamma\left(N_y - N_z\right)M_s + i\alpha\omega\right]}{\left[\gamma H + \gamma\left(N_x - N_z\right)M_s + i\alpha\omega\right]\left[\gamma H + \gamma\left(N_y - N_z\right)M_s + i\alpha\omega\right] - \omega^2} \tag{2.10}$$

$$\frac{d\vec{M}}{dt} = -\gamma'\left[\vec{M}\times\vec{H} + \frac{\alpha'}{M_s}\vec{M}\times\left(\vec{M}\times\vec{H}\right)\right] \tag{2.11}$$

where $N_x$, $N_y$ and $N_z$ are the demagnetizing factors along $x$, $y$ and $z$ directions, respectively.

The demagnetizing factors originate from dipolar interaction and are only related to the shape of the magnetic material. The sum of the three components equals to 1, as $N_x + N_y + N_z = 1$. For thin film structure, because the thickness is far small than the width and length of the film, one has $N_x = N_z = 0, N_y = 1$. For a magnetic nanowire, the demagnetization factors are $N_x = N_y = \frac{1}{2}$ and $N_z = 0$.

From Eq. (2.11), one can find that the resonance frequency is determined by effective field and the saturation magnetization. The magnetic anisotropy and saturation magnetization can be extracted by fitting the $H_{res}$ vs. frequency curves using Formula (2.11). The advantage of using FMR to measure the saturation magnetization of materials is that that one does not need to determine the volume or mass of the sample, which is very inaccurate for thin film samples.

The magnetic susceptibility is a complex number that carries the information of precession angle and the phase difference between the magnetization precession and the RF magnetic field. Figure 2.2 (b) shows a typical susceptibility spectrum of a ferromagnetic thin film. The frequency of RF field is fixed, and the external magnetic field varies from 500 Oe to 0 Oe. Near the resonance field, the curve of the imaginary part of susceptibility has Lorentzian shape; while the real part of susceptibility has a dispersive lineshape. At the resonance field, the relative phase between magnetization precession and RF field is $90^\circ$. The relative phase of the off-resonance case is $180^\circ$ or $-180^\circ$ below or above the resonance field, respectively. The linewidth $\Delta H$, determined from the peak-to-peak value of the real part of susceptibility or derivative of imaginary part of susceptibility $d\chi''/dH$, relates to the Gilbert damping constant α via [1]

$$\Delta H = \Delta H_0 + \frac{4\pi\alpha f}{\gamma} \tag{2.12}$$

where $\Delta H_0$ is the inhomogeneous broadening due to sample imperfections such as defects and impurities, surface anisotropy and two-magnon scattering. The Gilbert damping constant α can be extracted from the linear fitting of the linewidth $\Delta H$ versus frequency $f$.

## 2.3 Spin Wave

Above, we only discussed spatially uniform precession. In the general case, the magnetic precession can be spatially non-uniform throughout the magnetic sample. The non-uniform precession is usually expanded into many spin-wave modes through spatial Fourier transformation [2] as $m(x,t) = \sum_k m_k e^{jk\cdot x} e^{j\omega t}$, where $k$ is the wave number of each mode. $k = 0$ corresponds to the spatially uniform coherent FMR mode.

It is contemplated that the spin-wave modes $k \neq 0$ are less energetically favorable due to the large exchange energy. Therefore, for small angle uniform microwave excitation, the coherent precession is the dominant mode, and other spin wave modes are only at a thermal fluctuation level. However, the non-uniform spin-wave modes will be excited when the magnetization precession exceed a threshold, which is known as the spin-wave instability effect [3]. The macrospin approximation cannot be applied in this case, and the LLG equation has to be solved in both the time and spatial domains. Due to the non-uniform precession, the effective dipolar field and exchange interaction have to be reconsidered. Maxwell equations have to be solved with appropriate boundary conditions to find the effective dipolar field. The dipolar field $h_d$ and magnetization must satisfy the magnetostatic form of Maxwell's equations [4]

$$\nabla \cdot (\mathbf{h_d} + 4\pi \mathbf{M}) = 0 \tag{2.13}$$

$$\nabla \times \mathbf{h_d} = 0 \tag{2.14}$$

In the case of the uniform precession, the exchange interaction does not affect the magnetic dynamics since the precession is coherently in-phase throughout the sample. In a non-uniform case, the spin orientations of each atom are different. The exchange Hamiltonian can be written as

$$H = -\sum_{i,j} J_{ij} S_i \cdot S_j \tag{2.15}$$

The length scale of dipole-dipole interaction and exchange interaction are quite different. The exchange interaction is short range, because of the quantum mechanical exchange due to the overlap of electron wavefunctions. One can only consider the exchange interactions between neighboring electron spins. The dipole-dipole interaction is much smaller than the exchange interaction in short range but

becomes important for the spin dynamics at long wavelength. Therefore, the spin wave is categorized into three types based on the wavelength [5]. In the exchange region $10^6 cm^{-1} < |k| < 10^8 cm^{-1}$, the exchange contribution to the spin wave energy is dominant, and the dipolar interaction can be neglected. In the dipole-exchange region $10^5 cm^{-1} < |k| < 10^6 cm^{-1}$, both exchange and dipole interactions contribute to the spin-wave energy. In the magnetostatic region $10^6 cm^{-1} < |k| < 30 cm^{-1}$, the dipole-dipole interaction dominates, and the exchange interaction is negligible.

The dispersion relation is very crucial to understand spin waves. Dispersion relation relates the spin wave energy or frequency to the wavevector. In the exchange region, the spin-wave dispersion relation can be written as

$$\omega = D_{sw} k^2 \tag{2.16}$$

where $D_{sw}$ is the spin-wave stiffness parameter, which relates to the exchange interaction strength.

In the magnetostatic region, the spin wave modes depend on the relative orientation of magnetic field and wavevector. When the magnetization is aligned in the direction normal to the film plane, the spin waves that propagate in the film plane are called magnetostatic forward volume waves (MSFVW). When the magnetization is in the film plane, the spin wave that propagates perpendicular to the in-plane magnetization is called magnetostatic surface wave (MSSW). The surface spin wave will propagate either on the top surface of the film or the bottom surface depending on the direction of the wavevector. The spin wave that propagates parallel to the in-plane magnetization is called magnetostatic backward volume wave (MSBVW). In this case, the group velocity is opposite to the phase velocity. In addition to the spin waves that propagate in the film plane, there is also a type of perpendicular standing spin-wave

(PSSW). Its propagating direction is normal to the film plane. In PSSW geometry, the short-range exchange interaction dominates because of the small thickness of the thin films. The dispersion relation of MSFVW, MSSW, MSBVW, and PSSW are

$$\omega_{MSFVW}^2 = \omega_0\left[\omega_0 + \omega_M\left(1-\frac{1-e^{-k_{//}t}}{k_{//}t}\right)\right] \tag{2.17}$$

$$\omega_{MSSW}^2 = \omega_H(\omega_H + \omega_M) + \frac{\omega_M^2}{4}(1-e^{-2k_{//}t}) \tag{2.18}$$

$$\omega_{MSBVW}^2 = \omega_H\left[\omega_H + \omega_M\left(\frac{1-e^{-k_{//}t}}{k_{//}t}\right)\right] \tag{2.19}$$

and

$$\omega_{PSSW}^2 = (\omega_H + a\omega_M k_n^2)(\omega_H + \omega_M + a\omega_M k_n^2) \tag{2.20}$$

where $\omega_H = \gamma H$, $\omega_M = \gamma M_s$, $\omega_0 = \omega_H - \omega_M$, $t$ is the thickness of the film, $k_n$ is the quantized wavevector in the form of $k_n = \frac{n\pi}{t}$ which contains in-plane component $k_{//}$ and out-of-plane component $k_\perp$, $a$ is the exchange parameter. The detailed derivation of the dispersion relations can be found in Ref. [6].

## 2.4 Spin Transfer Torque

The spin transfer torque (STT) allows an efficient way to control magnetization electrically [7-10], which have resulted in the development of magnetic random access memory (MRAM) [11] and nanoscale oscillators at microwave frequency [12]. STT can be observed in a spin valve structure composed of two ferromagnetic (FM) layers separated by a nonmagnetic metal, illustrated in Figure 2.3.

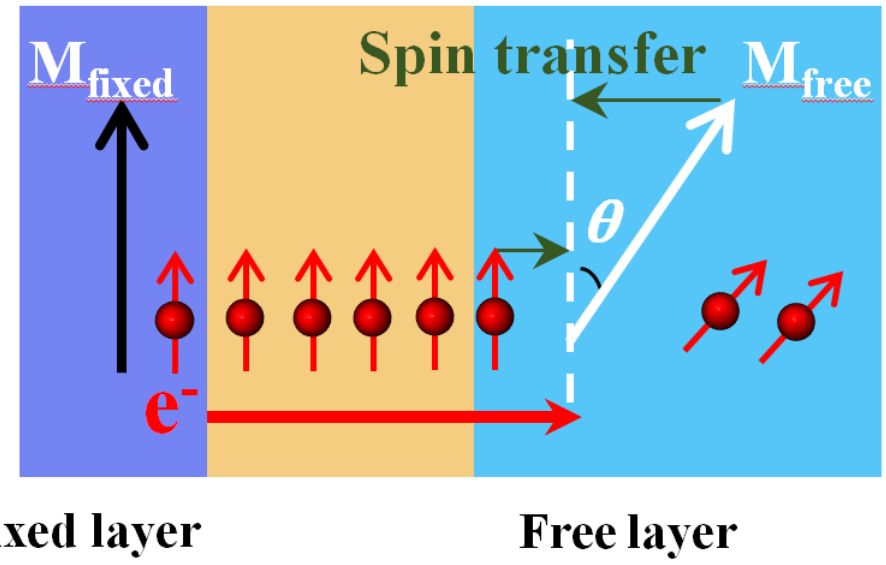


Figure 2.3 Schematics of spin transfer torque in a spin valve

One of the FM layers usually has its magnetic moment ($M_{fixed}$) fixed by a neighboring antiferromagnetic (AFM) layer through the exchange bias. The other FM layer ($M_{free}$) is free to rotate by magnetic fields. When a current is passing through the stack, the electron spins are polarized along the direction of $M_{fixed}$. If the $M_{free}$ is not collinear with $M_{fixed}$, the electrons with polarized spins passing through the free layer will align with $M_{free}$ due to exchange interaction. By the conservation of angular momentum, the change of the carrier spin momentum will transfer to $M_{free}$, which is the spin transfer torque. The spin polarized current carries angular momentum can manipulate the magnetic moment by the means of STT. LLG equation can describe the change of the magnetization due to STT by adding additional terms corresponding to STT

$$\frac{d\vec{M}}{dt} = -\gamma\vec{M}\times\vec{H} + \frac{\alpha}{M_s}\vec{M}\times\frac{d\vec{M}}{dt} + a\vec{M}\times\vec{\sigma} + b\vec{M}\times(\vec{\sigma}\times\vec{M}) \tag{2.21}$$

where $\vec{\sigma}$ is a unit vector in the direction of injected spin, $a$ and $b$ are the coefficients corresponding to the effective field-like torque (the third term on the right side of the

equation) and damping-like torque (the last term the right side of the equation), respectively. The STT was first proposed by Slonczewski [13] in 1996. Therefore, Eq.(2.21) is also known as Landau-Lifshitz-Gilbert-Slonczewski (LLGS) equation. The injected spin will cause two effects on the local magnetization. First, it will generate an effective field in the direction of the injected spin $\vec{\sigma}$. The third term of Eq. (2.21) $a\vec{M}\times\vec{\sigma}$ shows the similar form as the first term $-\gamma\vec{M}\times\vec{H}$. Secondly, the injected spin will cause a torque, as $b\vec{M}\times(\vec{\sigma}\times\vec{M})$. Because the direction of the effective torque is parallel or antiparallel to the torque due to damping, it is usually named as anti-damping or damping-like torque. When the anti-damping torque is large enough to overcome the Gilbert damping, the original steady state becomes unstable. The magnetization will either eventually switch its direction or maintain a constant precession. The first scenario usually occurs when the uniaxial anisotropy is higher than the external magnetic field. This effect is called spin-torque-driven magnetic switching, which is a very promising writing mechanism for MRAM. The benefits of such switching mechanism are high switching speed, low energy consumption, and robustness. The second scenario usually occurs when the external magnetic field is large enough to prevent the magnetic switching. Since the precession is at gigahertz frequency, the device converts the DC current into microwave emission, leading to a potential application as microwave nano-oscillators [14].

More recently, a new mechanism to induce STT was observed in a bilayer structure composed of an FM layer and a material with a large spin-orbital coupling (SOC) such as heavy metals (HM) like Pt or topological insulators. Due to the large SOC, the spin-up and spin-down electrons flowing in the HM is reflected into the opposite directions and generates a pure spin in the direction transverse to the charge current, which is called spin Hall effect (SHE) [15]. The transverse spin current diffuses into the adjacent FM layer and manipulates its magnetic configuration as illustrated in Figure 2.4. This new scheme Of SOC driven STT has attacked intensive attention from both industry and academy as a promising candidate for the next generation of MRAM.

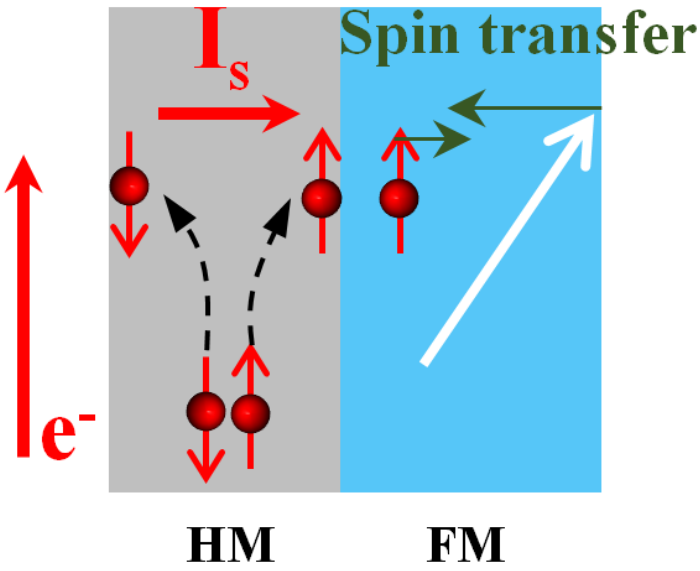

Figure 2.4 Generation of spin current with SHE in an HM layer and induced STT in the adjacent FM layer.

## 2.5 Spin-dependent Transport in Spin Valve and Magnetic Tunnel Junction

The coexistence of spin and electric charge properties in electron lead to the spin-dependent phenomenon and new functions of electronic devices, germinating a new area of spin electronics known as Spintronics. The discovery of giant magnetoresistance (GMR) effect [16, 17] in 1988 independently by Albert Fert and Peter Grünberg revolutionized the information storage in hard disk drives. The recording density of hard drives increase by 100 times due to the high sensitivity and miniature size of GMR spintronics devices, called spin valve. Subsequently, the tunnel magnetoresistance (TMR) discovered in magnetic tunnel junctions (MTJs) continuously boosts the increase of the recording density in hard drives. Besides working as field sensor in hard drives, MTJs are also used in applications such as nonvolatile magnetic random access memories and microwave detectors.

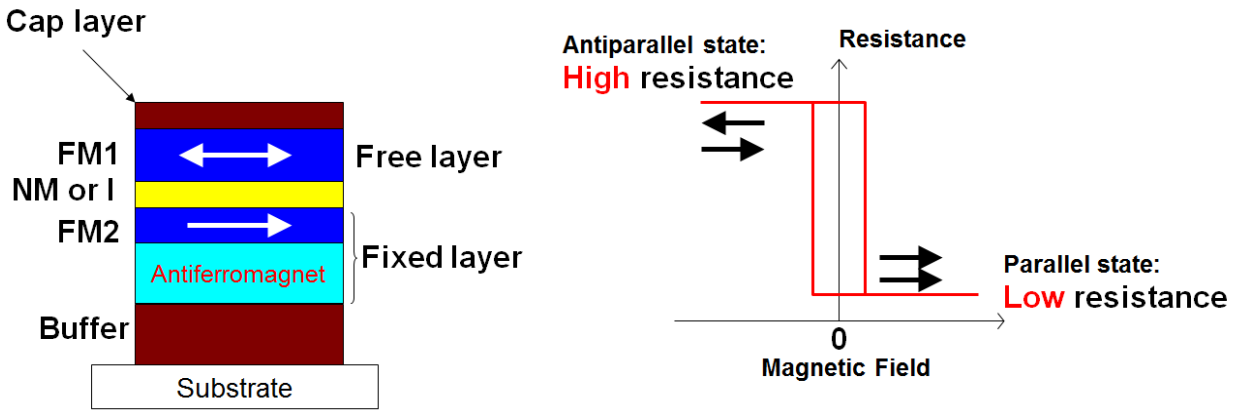


Figure 2.5 The structure of a spin valve (with NM spacer) or an MTJ (with I spacer), and a schematic resistance hysteresis loop of the device.

Figure 2.5 shows a typical structure of spin valve / MTJ. The spin valve consists of a non-magnetic layer (NM) sandwiched between two ferromagnetic electrodes (FM). One of the FM layers is called fixed layer, whose magnetization is aligned by exchange coupling to an adjacent antiferromagnetic layer. Another FM layer is the free layer, whose magnetization can be rotated by external magnetic field. Replacing the NM layer by an insulation layer (I), then the device becomes MTJ. The resistance of the device depends on the relative orientations of the magnetizations of the two FM layers: having a high resistance at antiparallel magnetization configuration and low resistance at parallel magnetization configuration.

### 2.5.1 Mott Two-current Model

The first model to describe the GMR in spin valve is proposed by Levy and Zhang [18] using the Mott two-current model. An important assumption of the model is two independent conducting channels are corresponding to the spin-up and spin-down electrons. The total resistance can be considered in a parallel circuit composed of spin-up and spin-down channels. Figure 2.6 shows the equivalent circuit for the parallel and antiparallel states. The two resistors at one channel represent the

resistance due to spin-dependent scattering at the two interfaces between ferromagnetic electrodes and the non-magnetic spacer layer. If the injected spin is antiparallel to the magnetization in FM layer, the resistor is large, due to a large amount of scattering. If the injected spin is parallel to the magnetization in FM layer, the resistor is small. The large resistor is defined as $R_1$ and the small resistor is defined as $R_2$, where $R_1 > R_2$. In the parallel state, the spin-up electrons are not scattered, resulting in two small resistors in the spin-up channel, while the spin-down electrons are scattered at each interface, resulting in two large resistors in the spin down channel. Therefore, the total resistance in the parallel state is $R_P = \frac{2R_1R_2}{R_1 + R_2}$. In the antiparallel state, following the same procedure, the total resistance is derived as $R_{AP} = \frac{R_1 + R_2}{2}$.

The GMR ratio is defined as

$$\frac{R_{AP} - R_P}{R_P} = \frac{(1-\alpha)^2}{2\alpha} \tag{2.22}$$

where $\alpha = \frac{R_1}{R_2}$ depends on the spin polarization of FM layers.

When the relative angle between the two magnetizations in FM layers is $\theta$, the resistance of the spin valve is

$$R(\theta) = \frac{1}{2}(R_{AP} + R_P) + \frac{1}{2}(R_{AP} - R_P)\cos(\theta) \tag{2.23}$$

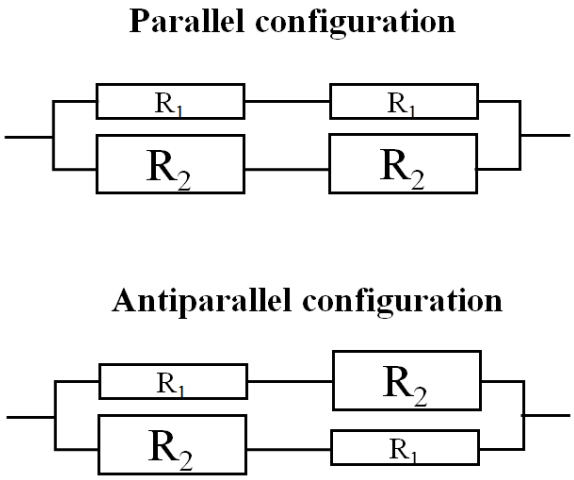

Figure 2.6 The Mott's equivalent circuit model for the parallel and antiparallel configurations.

### 2.5.2 Julliere Model

To describe the tunnel magnetoresistance (TMR) in MTJs, Julliere has proposed a model [19] in 1975 based on two assumptions. First, similar to the Mott two-current model, there are two independent conducting channels for spin-up and spin-down electrons. The spin-up electrons in one FM electrode will only transport to the empty spin-up states in the second electrode as illustrated in Figure 2.7, due to the Fermi's golden rule. In FM layers, the density of states (DOS) of the majority and minority electrons at the Fermi level are different. In the parallel state, the spin-up electrons are the majority electrons at the Fermi level for both electrodes. There are many empty spin-up states in the right FM electrode. So the conductance is large. In the antiparallel state, the spin-up electrons are the majority electrons in the left electrode, while the spin-down electrons are the majority electrons in the right electrode. There are few empty spin-up states in the right electrode, leading to low conductance. The second assumption is the conductance is proportional to the product

of the DOS in the two FM electrodes. The conductance for the parallel and antiparallel configurations can be expressed as [20]

$$G_p \propto n_{1\uparrow} n_{2\uparrow} + n_{1\downarrow} n_{2\downarrow} \tag{2.24}$$

$$G_{Ap} \propto n_{1\uparrow} n_{2\downarrow} + n_{1\downarrow} n_{2\uparrow} \tag{2.25}$$

where $n_{1\uparrow}$ and $n_{2\uparrow}$ are the density of states (DOS) of spin-up electrons in the left and right electrodes, and $n_{1\downarrow}$ and $n_{2\downarrow}$ are the DOS of spin-down electrons.

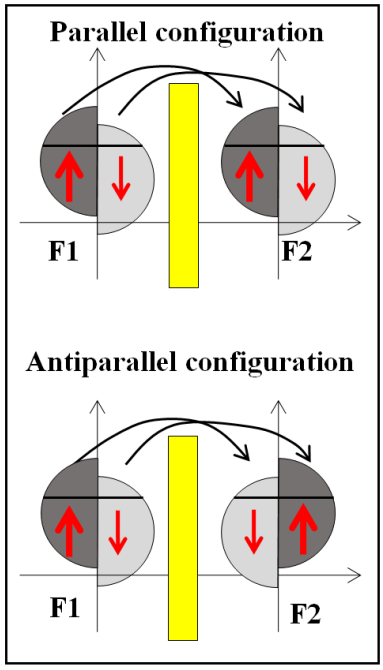


Figure 2.7 The electronic structures of the MTJ in the parallel and antiparallel configurations

The conductance of the parallel state is always larger than that in an antiparallel state. One obtains Julliere's formula for the TMR as [20]

$$TMR = \frac{G_{AP} - G_P}{G_P} = \frac{2P_L P_R}{1 - P_L P_R} \tag{2.26}$$

where $P_L$ and $P_R$ are the spin polarization in the left and right electrodes, defined as $P = \frac{n_\uparrow - n_\downarrow}{n_\uparrow + n_\downarrow}$.

### 2.5.3 Tunneling in MTJs with Crystalline MgO Barriers

The Julliere model has successfully explained the tunneling in MTJs with amorphous insulating barriers such as $Al_2O_3$. However, the highest TMR ratio in the MTJs with $Al_2O_3$ is less than 100% [21], because the spin polarization is always less than 1 in ferromagnetic transition metals [22]. S. Yuasa et al. [23] reported a TMR up to 180% at room temperature in an epitaxial-grown single-crystal Fe/MgO/Fe MTJs. Due to the band matching, MgO works as a spin filter only allowing majority electrons to pass, effectively making FM electrodes having 100% spin polarization. Figure 2.8 shows a schematic of electron tunneling through an amorphous $Al_2O_3$ and crystalline MgO (001) barrier. The top and bottom layers are Fe (001) as a typical 3d ferromagnetic material. Three majority electron Bloch states $\Delta_1$, $\Delta_2$ and $\Delta_3$ exists in single crystal Fe electrodes. They have different symmetries of wave functions. The Block states couple with evanescent states in the insulating barrier, so that the tunneling with finite probability occur. Among the three Bloch states, $\Delta_1$ state usually has a positive spin polarization and higher tunneling possibility. In the amorphous $Al_2O_3$ barrier, the other Bloch states can also tunnel through the barrier, resulting in a reduced net spin polarization, because the spin polarization of $\Delta_2$ state is negative. The crystalline MgO barrier acts as a spin filter that the $\Delta_2$ and $\Delta_3$ are not able to tunnel through. Only the highly spin-polarized $\Delta_1$ state tunnels through MgO. The theoretical expectation of the TMR ratio in this type of MTJs can be high as 1000% [24].

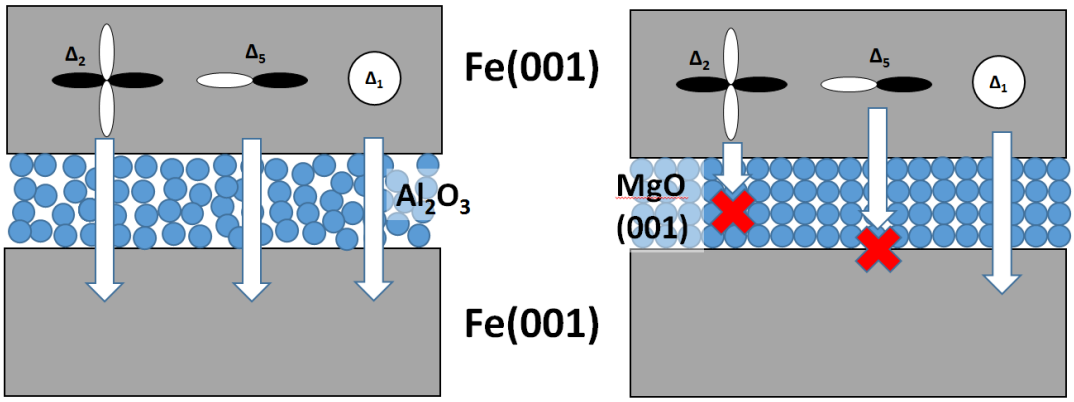

Figure 2.8 Schematics of electron tunneling trough an amorphous Al2O3 barrier and a MgO(001) barrier

## REFERENCES


[1] W. Platow, A. N. Anisimov, G. L. Dunifer, M. Farle, and K. Baberschke, "Correlations between ferromagnetic-resonance linewidths and sample quality in the study of metallic ultrathin films," *Physical Review B,* vol. 58, pp. 5611-5621, 09/01/ 1998.

[2] T. Oguchi, "Theory of spin-wave interactions in ferro-and antiferromagnetism," *Physical Review,* vol. 117, p. 117, 1960.

[3] M. Polianski and P. Brouwer, "Current-induced transverse spin-wave instability in a thin nanomagnet," *Physical review letters,* vol. 92, p. 026602, 2004.

[4] B. Hillebrands, "Spin-wave calculations for multilayered structures," *Physical Review B,* vol. 41, p. 530, 1990.

[5] M. G. Cottam, *Linear and nonlinear spin waves in magnetic films and superlattices*: World Scientific, 1994.

[6] B. Kalinikos and A. Slavin, "Theory of dipole-exchange spin wave spectrum for ferromagnetic films with mixed exchange boundary conditions," *Journal of Physics C: Solid State Physics,* vol. 19, p. 7013, 1986.

[7] M. Stiles and A. Zangwill, "Anatomy of spin-transfer torque," *Physical Review B,* vol. 66, p. 014407, 2002.

[8] Z. Li and S. Zhang, "Magnetization dynamics with a spin-transfer torque," *arXiv preprint cond-mat/0302337,* 2003.

[9] K.-J. Lee, A. Deac, O. Redon, J.-P. Nozières, and B. Dieny, "Excitations of incoherent spin-waves due to spin-transfer torque," *Nature Materials,* vol. 3, pp. 877-881, 2004.

[10] Z. Diao, Z. Li, S. Wang, Y. Ding, A. Panchula, E. Chen*, et al.*, "Spin-transfer torque switching in magnetic tunnel junctions and spin-transfer torque random access memory," *Journal of Physics: Condensed Matter,* vol. 19, p. 165209, 2007.

[11] Y. Huai, "Spin-transfer torque MRAM (STT-MRAM): Challenges and prospects," *AAPPS Bulletin,* vol. 18, pp. 33-40, 2008.

[12] D. Houssameddine, U. Ebels, B. Delaët, B. Rodmacq, I. Firastrau, F. Ponthenier*, et al.*, "Spin-torque oscillator using a perpendicular polarizer and a planar free layer," *Nature Materials,* vol. 6, pp. 447-453, 2007.

[13] J. C. Slonczewski, "Current-driven excitation of magnetic multilayers," *Journal of Magnetism and Magnetic Materials,* vol. 159, pp. L1-L7, 1996.

[14] V. E. Demidov, S. Urazhdin, H. Ulrichs, V. Tiberkevich, A. Slavin, D. Baither*, et al.*, "Magnetic nano-oscillator driven by pure spin current," *Nature Materials,* vol. 11, pp. 1028-1031, 2012.

[15] J. Hirsch, "Spin Hall effect," *Physical Review Letters,* vol. 83, p. 1834, 1999.

[16] M. N. Baibich, J. M. Broto, A. Fert, F. N. Van Dau, F. Petroff, P. Etienne*, et al.*, "Giant Magnetoresistance of (001)Fe/(001)Cr Magnetic Superlattices," *Physical Review Letters,* vol. 61, pp. 2472-2475, 11/21/ 1988.

[17] G. Binasch, P. Grünberg, F. Saurenbach, and W. Zinn, "Enhanced magnetoresistance in layered magnetic structures with antiferromagnetic interlayer exchange," *Physical Review B,* vol. 39, pp. 4828-4830, 03/01/ 1989.

[18] P. M. Levy and S. Zhang, "Our current understanding of giant magnetoresistance in transition-metal multilayers," *Journal of magnetism and magnetic materials,* vol. 151, pp. 315-323, 1995.

[19] M. Julliere, "Tunneling between ferromagnetic films," *Physics Letters A,* vol. 54, pp. 225-226, 1975.

[20] E. Y. Tsymbal, O. N. Mryasov, and P. R. LeClair, "Spin-dependent tunneling in magnetic tunnel junctions," *Journal of Physics: Condensed Matter,* vol. 15, p. R109, 2003.

[21] J. J. Yang, C. Ji, Y. A. Chang, X. Ke, and M. Rzchowski, "Over 70% tunneling magnetoresistance at room temperature for a CoFe and AlOx based magnetic tunnel junction," *Applied Physics letters,* vol. 89, p. 2502, 2006.

[22] M. Getzlaff, J. Bansmann, and G. Schönhense, "Spin-polarization effects for electrons passing through thin iron and cobalt films," *Solid State Communications,* vol. 87, pp. 467-469, 8// 1993.

[23] S. Yuasa, T. Nagahama, A. Fukushima, Y. Suzuki, and K. Ando, "Giant room-temperature magnetoresistance in single-crystal Fe/MgO/Fe magnetic tunnel junctions," *Nature Materials,* vol. 3, pp. 868-871, 2004.

[24] J. Mathon and A. Umerski, "Theory of tunneling magnetoresistance of an epitaxial Fe/MgO/Fe (001) junction," *Physical Review B,* vol. 63, p. 220403, 2001.

# Chapter 3

# FABRICATION AND CHARACTERIZATION TECHNIQUES

## 3.1 Magnetron Sputtering

Magnetron Sputtering is a vacuum physical vapor deposition (PVD) technique to fabricate thin films with various materials like metals, alloys, oxides and so on. The sputtering process is schematically depicted in Figure 3.1. An electric field accelerates the spontaneously ionized positive gas ions and bombards the atoms of the target with the guide of the magnetic field. The target is made of the material that one desires to use. Subsequently, the secondary electrons generated in this process will be accelerated and ionize the gas atoms to sustain the sputtering process. Due to the conservation of the momentum, some of the atoms on the target are knocked out with a momentum and move to the substrate on top of the target. These atoms form a thin film on the substrate. The permanent magnet underneath the target provides a magnetic field *B*. There is a perpendicular electric field *E* to accelerate the ions. The electrons and ions feel the Lorentz force in the direction of $\vec{E} \times \vec{B}$ that traps the electrons and ions into toroidal orbits near the target surface. Consequently, ionization efficiency is significantly enhanced. The magnetron sputtering operates in the pressure range from 1 to 20 mTorr. The low gas pressure makes less chance of collision between sputtered atoms and gas atoms. The sputtered atoms have a long mean-free-path and high momentum. The sputtering rate is thus high, and the deposited thin film is with small roughness.

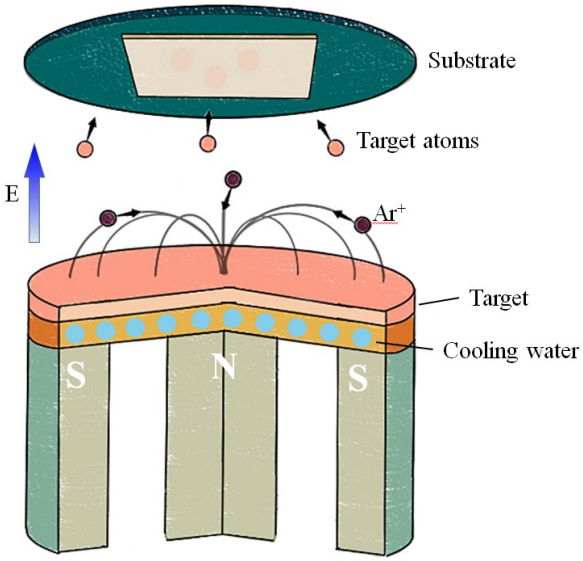


Figure 3.1 Illustration of the sputtering process and Structure of the magnetron sputtering.

During the collision between the gas ion and target, the electric charge of the ions transfers to the target. If the target is made of insulating material, the charge will accumulate on the surface. Subsequently, the surface charge on the target will repel other gas ions from bombardment because of the opposite accumulated charge. An alternating electric field is applied to the target to sustain the bombardment. This method is referred to RF sputtering. There is also an alternative method to fabricated insulating thin film. A metal film is first deposited through DC sputtering a metal target. Then the metal film is oxidized in oxygen plasma generated by an oxidation gun shown in Figure 3.2. The AC electric field discharges the oxygen gas on the electrode. 120W RF power is applied to the electrode, and the oxygen gas pressure is 60 mTorr. The sample is directly placed right above the electrode to be oxidized.

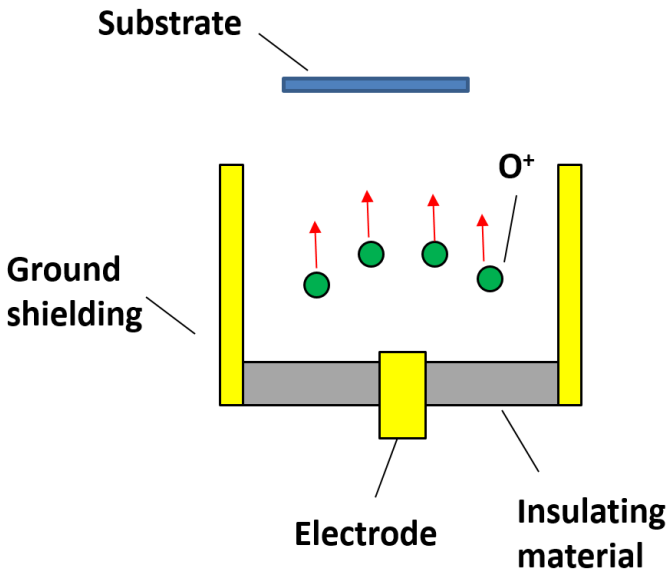


Figure 3.2 Schematics of oxidation process

## 3.2 Microfabrication and Magnetoelectric Transport Measurement

Microfabrication techniques are used to fabricate micron or nanometer structures and devices in industry and laboratory. In this research, we used two fabrication methods: photolithography and ion-beam milling.

### 3.2.1 Photolithography

Photolithography is a process to apply a layer of photoresist (PR) with the designed shape on the substrate. We developed two types of photolithography processes: positive and negative photolithography. Figure 3.3 shows their procedures. For the positive photolithography, a thin layer of PR (AZ 1512) is uniformly applied to a substrate via spin coating at 4000 RPM for one minute and followed by one minute baking at 110 °C. The second step is to align the substrate with a photomask. On the photomask, there are pre-fabricated patterns with the dark material that is not transparent to the UV light. The substrate is placed on a mask aligner (OAI HYBRALIGN SERIES 200) to align with the mask. After the alignment, the area that

not covered by the dark patterns on the mask is exposed to UV light for 6 seconds. In the last step, the sample is immersed in the developer (Rohm Haas MF319) for about 20 seconds to remove the exposed area. As a result, the PR with the same patterns as the shapes on the photomask will stay on the substrate. For the negative photolithography, a thin layer of negative photoresist AZ 5214 is applied to the substrate via spin coating and then baked at 90 °C for one minute. The substrate is aligned with the mask, followed by a 0.7 second UV light exposure. Then the sample is baked at 110 °C for one minute and exposed to UV light for 45 seconds without a mask. In the last step, the film is developed by immersing in developer AZ 300 MIF for 20 seconds. Finally, the transparent area on the mask will be imprinted onto the substrate.

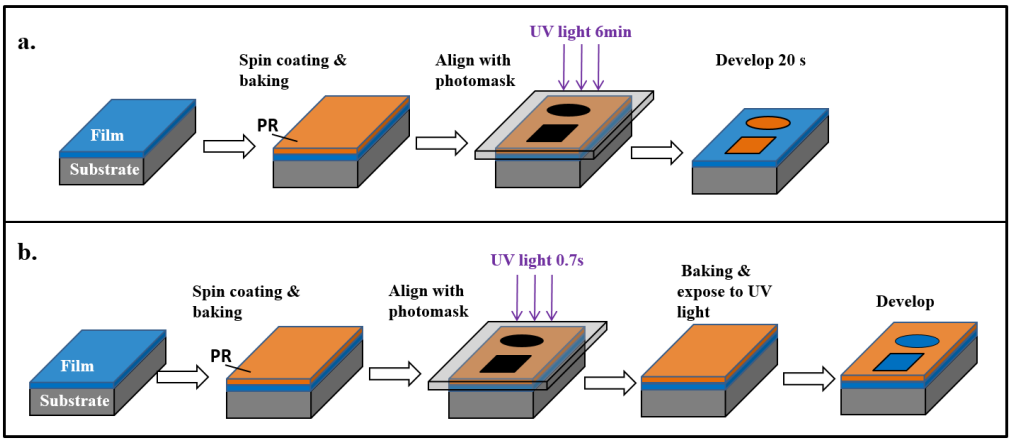


Figure 3.3 Schematics of photolithography procedures (a) Positive photolithography (b) Negative photolithography

### 3.2.2 Ion Beam Milling

Ion beam milling is a dry etching process to remove the films in the area that is not covered by PR. The ion-beam milling process is depicted in Figure 3.4. An

accelerating grid accelerates the argon ions generated by a cathode filament. The ions strike the film attached to a sample stage to remove the materials. During the milling operation, the sample stage is cooled by cooling water and rotates to ensure uniformity of ion-beam bombardment. And the sample stage is usually tilted at 5° to 10° to keep the etching edge clean. A neutralization filament prevents the accumulation of positive charge on the sample stage. After the ion beam etching, the film was placed in the acetone to remove the PR, resulting in the designed structures.

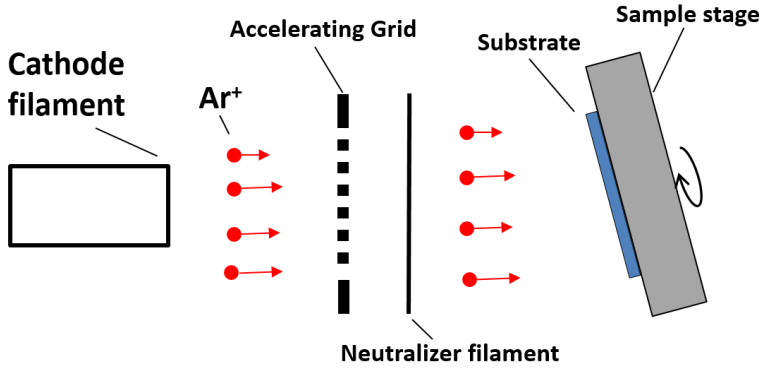


Figure 3.4 Schematics of the ion beam etching process.

### 3.2.3 The Fabrication Process and Electrical Characterization of Hall Bar and MTJs

The spin-dependent electrical transport is a crucial phenomenon in spintronics. The transport measurements are categorized into two types: current-in-plane (CIP) measurement and current-perpendicular-to-plane (CPP) measurement.

A Hall bar is usually used to perform CIP measurement. As shown in Figure 3.5, a typical geometry of Hall bar has six contact pads. The electrical current is applied between contacts 1 and 2. The electrical resistivity is calculated by dividing the voltage between contacts 3 and 4 or 5 and 6 with the current applied. The Hall

resistivity is calculated by dividing the Hall voltage between contacts 3 and 5 or 4 and 6 with the current. Two pairs of Helmholtz coils are used to generate a magnetic field in y and z directions.

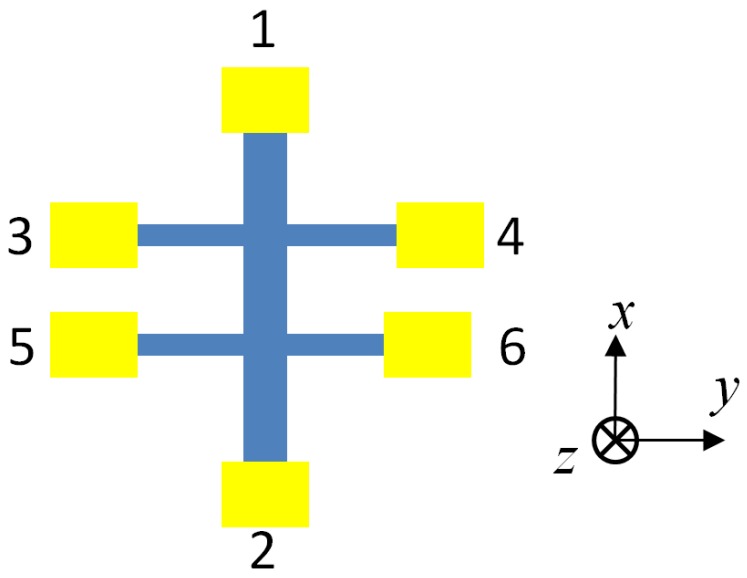


Figure 3.5 The schematics of a typical Hall bar structure

The CPP measurements are usually used to test MTJs because the tunneling occurs with the current passing through the film stacks. Two testing geometries have been developed. The first geometry is illustrated in Figure 3.6. The film stack is fabricated into pillar structures through positive lithography and ion beam milling. The etching is precisely controlled to stop at the bottom electrode. The size of the pillar ranges from 10 μm to 100 μm. The pin holes exist in the barrier due to the imperfection of the fabrication process. The pillars of large size are usually shorted by the pin holes; while the small pillars are generally pin-hole free. We contact the top electrodes of a small and a large MTJ pillar with probes and measure the resistance

with scanning the magnetic field in the film plane. In this case, the measured resistance and TMR are due to the small pillars because of the shortage of the large MTJ pillars.

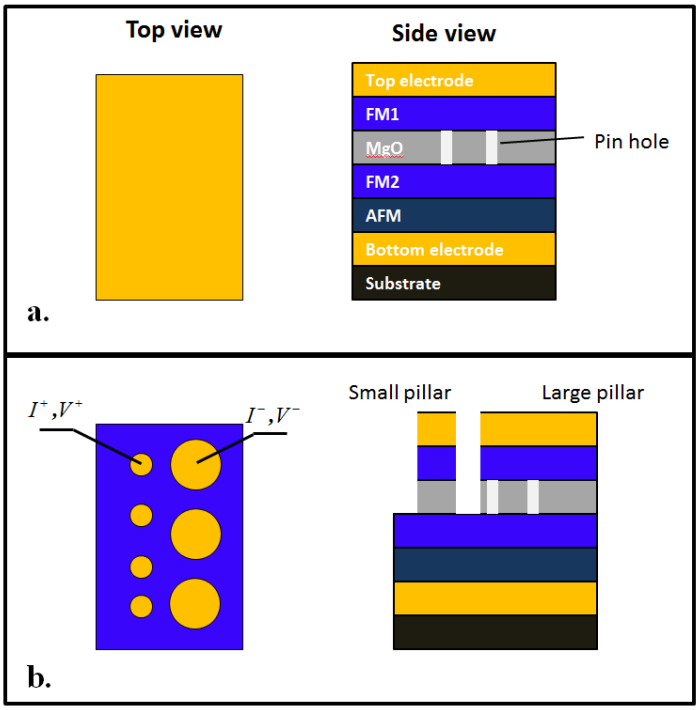


Figure 3.6 The fabrication process and measurement schematics of quick TMR test. (a) The top view shows the whole film before micro-fabrication. The side view shows some pin holes in MgO layer which connect top and bottom electrodes. (b) After positive photolithography, ion beam etching and cleaning in acetone, the MTJ stacks were defined into small and large pillars. The top view illustrates the measurement setup.

The resistance measurement is usually properly performed in 4-probe configuration. The process for fabricating the MTJs with four contact pads is illustrated in Figure 3.7. The MTJ film is defined into strips with "I" shape through positive photolithography and etching down process, as shown in Figure 3.7 (b). Then the MTJs pillars with size from 10 μm to 100 μm are defined on the strip through positive photolithography and controlled ion beam etching. The etching stopped at the

bottom electrode. Next, a thick layer (150nm) of SiO2 is deposited to insulate the side of the MTJ pillar to prevent the shortage between top and bottom electrodes. After the deposition, the sample is immersed in the acetone overnight to peel off the PR. The final step is to fabricate the top contact strip on the top electrode of MTJs by negative photolithography and sputtering of Au. The resistance measurements were performed by the 4-probe configuration shown in Figure 3.7 (d).

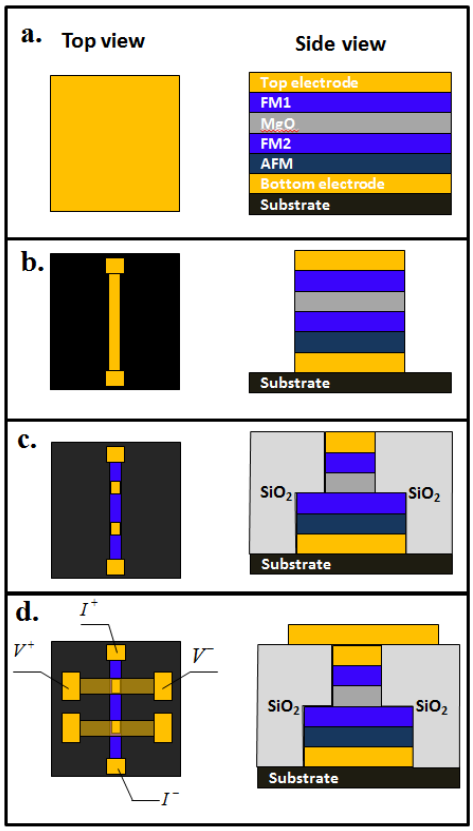


Figure 3.7 The fabrication process of the MTJ testing structure for four-probe measurements.

## 3.3 Structure and Magnetic Characterization

### 3.3.1 X-ray Diffraction

X-ray diffraction is a non-destructive technique to identify the crystalline information of materials. The principle of the X-ray diffraction is the elastic scattering of X-ray with periodic lattice of crystal and constructive interference of the reflected wave, governed by Bragg's Law [1]:

$$n\lambda = 2d_{hkl}\sin\theta_{hkl} \tag{3.1}$$

where $n$ is an integer number, $\lambda$ is the wavelength of the X-ray, $hkl$ is the Miller indices representing certain crystal planes, $d$ is the distance between these adjacent planes, and $\theta$ is the incident angle of the X-ray. The X-ray beam incidents at an angle $\theta$ on crystal planes with separation $d$. By comparing the measured XRD pattern with the standard XRD spectrum, one can identify the materials and their crystal structures.

The intensity of diffraction peak $I$ is expressed by [2]

$$I = |F|^2 p\left(\frac{1+\cos^2 2\theta}{\sin^2\theta\cos\theta}\right)e^{-2M} \tag{3.2}$$

where $p$ is the multiplicity factor, $e^{-2M}$ is the temperature factor, and $F$ is the structure factor that describes how a material scatters incident radiation and is defined as [3]

$$F_{hkl} = \sum_{1}^{N} f_n \exp\left[2\pi i\left(ha_n + kb_n + lc_n\right)\right] \tag{3.3}$$

where $a_n$, $b_n$, and $c_n$ are the lattice constants and $f_n$ is the scattering factor from a single atom in the unit cell. Certain diffraction peaks may vanish in the diffraction pattern determined by the crystalline structure of the sample. For instance, in a body-centered cubic (bcc) crystal, the three lattice constants are equal to $a$, and the

scattering factors of the atoms in a unit cell are equal to *f*. Therefore, the structure factor is given by

$$F_{hkl} = f\left[1 + (-1)^{h+k+l}\right] \tag{3.4}$$

The structure factor depends on the sum of the Miller indices as

$$F_{hkl} = \begin{cases} 2f, & h+k+l \quad even \\ 0, & h+k+l \quad odd \end{cases} \tag{3.5}$$

If the sum of the Miller indices is odd, the diffraction peaks will vanish.

The X-ray diffraction can be used to determine the film thickness when the incident angle is small (0.5°~10°). In this case, the X-ray beam reflected from the top and bottom surface of the film, so that the parameter *d* in Eq. (3.1) is equal to the film thickness.

### 3.3.2 Vibrating Sample Magnetometer

Vibrating Sample Magnetometer (VSM) is a standard technique to characterize the DC magnetic properties of magnetic materials. A typical schematic diagram of a VSM instrument is shown in Figure 3.8 [4]. The magnetic sample is attached to a vibrating rod that oscillates in the vertical direction at a frequency $\omega$. The rod is placed in an external magnetic field generated via an electromagnet. An AC voltage is induced in the pick-up coil, due to the Faraday's law of induction. A lock-in amplifier measures the induced voltage at the reference frequency $\omega$. The detected voltage is proportional to the magnetic moment of the sample. The calibration of the instrument is done by measuring a nickel sphere standard sample with a known magnetic moment as 6.9 emu at 5000 Oe.

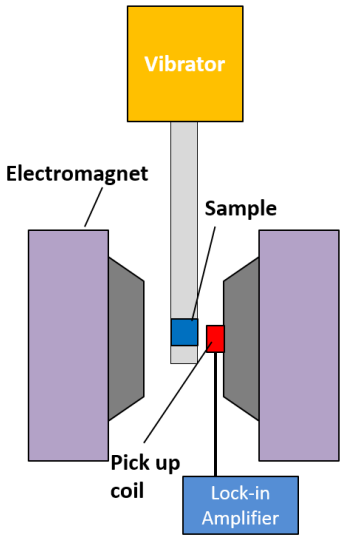

Figure 3.8 Schematic of a vibrating sample magnetometer instrument

## 3.4 Microwave Measurement

### 3.4.1 Microwave Measurement with Vector Network Analyzer

Vector Network Analyzer (VNA) is a powerful microwave measurement tool which generates microwave and detects both of the amplitude and phases. A VNA has two ports, both emitting and detecting microwave. The signal VNA measured is the transmitted and reflected voltage at the two ports from which the S-parameters can be calculated [5]. The measurement process is shown in Figure 3.9. First, the input microwave ($V_1^+$) is generated from port 1. At this moment, the output of port *2* $V_2^- = 0$. Some of the power pass through the cables and device under test (DUT) and then is detected at port 2 as $V_2^+$. Some parts of the microwave are reflected due to impedance mismatch measured at port 1 as $V_1^-$. Inversely, the microwave is input at port 2. In this case, $V_2^-$, $V_1^-$ and $V_2^+$ are measured. The S-parameters can be calculated as

$$S_{11} = \left.\frac{V_1^-}{V_1^+}\right|_{V_2^-=0}, S_{21} = \left.\frac{V_2^+}{V_1^+}\right|_{V_2^-=0} \tag{3.6}$$

$$S_{12}=\left.\frac{V_1^-}{V_2^-}\right|_{V_1^+=0},S_{22}=\left.\frac{V_2^+}{V_2^-}\right|_{V_1^+=0} \tag{3.7}$$

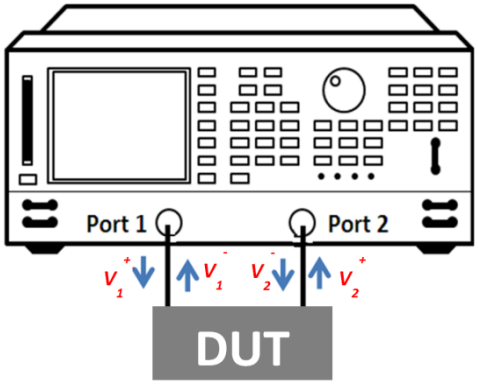


Figure 3.9 Illustration of S parameters measurement with VNA

### 3.4.2 Transmission Line Theory

The electromagnetic wave propagation in a waveguide can be described by transmission line model [6]. As shown in Figure 3.9 (a), an electromagnetic wave is propagating along the z axis. The system can be modeled as an equivalent circuit as illustrated in Figure 3.9 (b). According to Kirchhoff's circuit laws, one can write the equations for voltage and current as

$$\begin{cases} v(z,t)-R\Delta z i(z,t)-L\Delta z\dfrac{\partial i(z,t)}{\partial t}-v(z+\Delta z,t)=0 \\ i(z,t)-G\Delta z v(z+\Delta z,t)-C\Delta z\dfrac{\partial v(z+\Delta z,t)}{\partial t}-i(z+\Delta z,t)=0 \end{cases} \tag{3.8}$$

where $R$, $L$, $G$ and $C$ are the distributed lumps elements of resistance, inductance, dielectric conductance, and capacitance, respectively.

By considering the $e^{i\omega t}$ form of voltage and current, as $v(z,t)=v(z)e^{i\omega t}$ and $i(z,t)=i(z)e^{i\omega t}$, and taking the limit $\Delta z\to 0$, one can derive two differential equations for voltage and current,

$$\begin{cases} \dfrac{dv(z)}{dz} = -i(z)(R + j\omega L) \\ \dfrac{di(z)}{dz} = -v(z)(G + j\omega C) \end{cases} \tag{3.9}$$

The above equations can be solved as

$$\begin{cases} v(z) = v_0^+ e^{-\gamma z} + v_0^- e^{\gamma z} \\ i(z) = i_0^+ e^{-\gamma z} + i_0^- e^{\gamma z} \end{cases} \tag{3.10}$$

where the propagation constant $\gamma = \sqrt{(R + j\omega L)(G + j\omega C)}$ and the impedance $Z = \dfrac{v_0^+}{i_0^+} = \dfrac{-v_0^-}{i_0^-} = \sqrt{\dfrac{R + j\omega L}{G + j\omega C}}$.

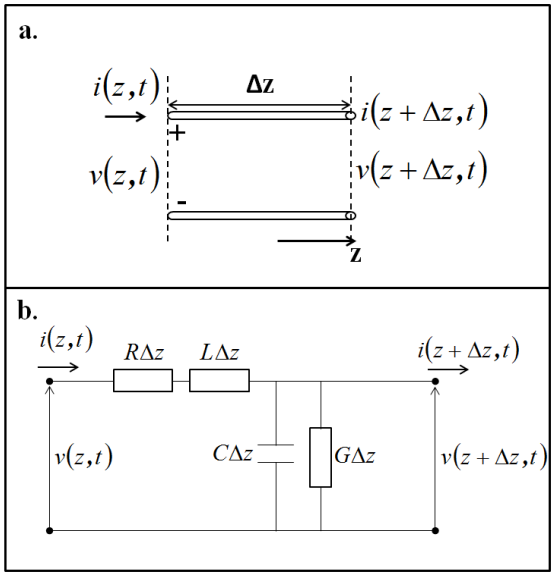


Figure 3.10 (a) The configuration of voltage and current in a transmission line. (b) Lumped-element equivalent circuit.

When two transmission lines are connected in series, as illustrated in Figure 3.11, based on the continuity of the electric field, the boundary condition can be written as

$$\begin{cases} v_2^+ + v_2^- = v_3^+ + v_3^- \\ \dfrac{v_2^+ - v_2^-}{Z_{01}} = \dfrac{v_3^+ - v_3^-}{Z_{02}} \end{cases} \tag{3.11}$$

where $Z_{01}$ and $Z_{02}$ are characteristic impedance of the first and second transmission line respectively. In each transmission line, the propagation of the voltage can be calculated from Eq. (3.10)

$$\begin{aligned} v_2^+ &= v_1^+ e^{-\gamma_1 l_1} \quad v_4^+ = v_3^+ e^{-\gamma_2 l_2} \\ v_2^- &= v_1^- e^{\gamma_1 l_1} \quad , \quad v_4^- = v_3^- e^{\gamma_2 l_2} \end{aligned} \tag{3.12}$$

where $\gamma_1$ and $\gamma_2$ are the propagation constant of the first and second transmission line respectively, and $l_1$ and $l_2$ are the length of the first and second transmission line respectively. Based on Eqs. (3.11) and (3.12), one can calculate the voltage at any location in a series of transmission lines

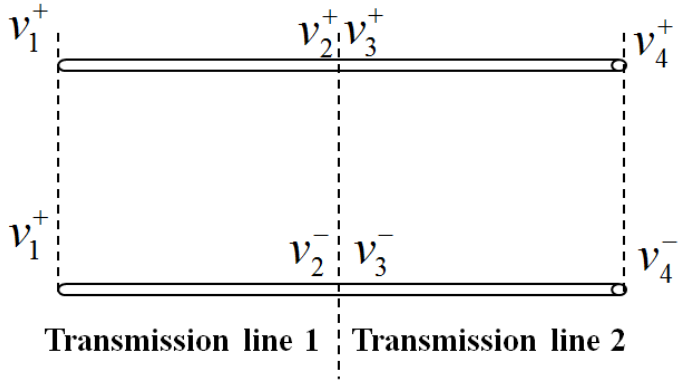


Figure 3.11 Illustration of two transmission line in series.

### 3.4.3 Formulism for Measurement of the Permeability and Permittivity by Rectangular Waveguide and Coaxial Line

The magnetic and dielectric properties of solid materials are under detection throughout the interaction between materials and microwave. Transmission

line methods are the simplest of the relatively accurate methods to determine the complex permeability and permittivity of materials. Usually, rectangular waveguide and coaxial lines are used in transmission line measurements.

Considering the relative simplicity, the off-resonance waveguide, and coaxial line transmission/reflection (TR) method [7, 8] is utilized in the measurement. In this technique, a precisely machined sample is placed in a section of the waveguide or VNA measures coaxial line and the S-parameters. One can extract the permeability and permittivity from the relevant scattering equations with S parameters. The precision of this method is mainly determined by the air gap between sample and waveguide.

Assuming there are no sources of electric and magnetic fields in the waveguide and there is no free charge building up, the EM field satisfies homogeneous Helmholtz equations

$$\nabla^2 \mathbf{E} + k^2 \mathbf{E} = 0 \tag{3.13}$$

$$\nabla^2 \mathbf{H} + k^2 \mathbf{H} = 0 \tag{3.14}$$

The field can be separated into transverse (T) and longitudinal (z) components as

$$\mathbf{E} = \mathbf{E}_T + E_z \mathbf{z} \tag{3.15}$$

$$\mathbf{H} = \mathbf{H}_T + H_z \mathbf{z} \tag{3.16}$$

The $E_z$ component is generated from TM mode, $H_z$ is from TE mode.

The transverse components satisfy

$$\nabla_T^2 \mathbf{E} = -\left(k^2 + \gamma^2\right)\mathbf{E} \equiv -k_c^2 \mathbf{E} \tag{3.17}$$

where the propagation constant is $\gamma = j\sqrt{\frac{\omega^2 \mu\varepsilon}{c^2} - k_c^2}$ , $k_c$ is the cutoff wavenumber.

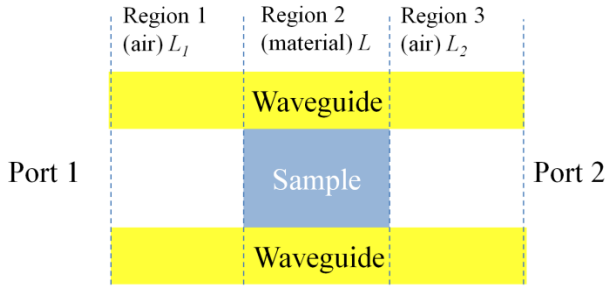


Figure 3.12 Illustration of permeability and permittivity measurement with the waveguide.

If we consider a perfect sample in an ideal waveguide as shown in Figure 3.12, in region 1 and 3, the permeability and permeability are $\mu_0$ and $\varepsilon_0$. The propagation constant for region 1 and 3 is $\gamma_0 = j\sqrt{\frac{\omega^2 \mu_0\varepsilon_0}{c^2} - k_c^2}$ . In region 2 where the sample is located, the permeability and permeability are $\mu = \mu' + j\mu''$ and $\varepsilon = \varepsilon' + j\varepsilon''$. And the propagation constant for region 2 is $\gamma = j\sqrt{\frac{\omega^2 \mu\varepsilon}{c^2} - k_c^2}$ . The solutions of $E$ field are as follow

$$E_1 = \frac{1}{\gamma}\left[e^{-\gamma_0 z} + S_{11}e^{\gamma_0 z}\right] \tag{3.18}$$

$$E_2 = \frac{1}{\gamma}C_2\left[e^{-\gamma z} + C_3 e^{-\gamma z}\right] \tag{3.19}$$

$$E_3 = \frac{1}{\gamma}\left[S_{21}e^{-\gamma_0 (z-L)}\right] \tag{3.20}$$

The constants $C_1$, $C_2$, and $C_3$, in the above equations can be determined by the boundary conditions, which is the tangential components of $E$ field and $B$ field are continuous under the assumption that no surface currents exist. For a 2-port device, the

measured S-parameters are related to the solution of Eq. (3.18)-(3.20) through subject to the boundary conditions. The S-parameters measured by the device reference planes (S) are related to the S-parameters at the sample surface (*S'*) by

$$S' = \varphi S \varphi \tag{3.21}$$

where $\varphi = \begin{pmatrix} e^{j\varphi_1} & 0 \\ 0 & e^{j\varphi_2} \end{pmatrix}$, $\varphi_1 = j\gamma_0 L_1$, and $\varphi_2 = j\gamma_0 L_2$.

The S-parameters are defined regarding the reflection coefficient $\Gamma$ and transmission coefficient *z* as

$$S_{11} = R_1^2 \left[ \frac{\Gamma(1-z^2)}{1-\Gamma^2 z^2} \right] \tag{3.22}$$

$$S_{22} = R_2^2 \left[ \frac{\Gamma(1-z^2)}{1-\Gamma^2 z^2} \right] \tag{3.23}$$

$$S_{12} = S_{21} = R_1 R_2 \left[ \frac{z(1-\Gamma^2)}{1-\Gamma^2 z^2} \right] \tag{3.24}$$

where $R_1 = e^{-\gamma_0 L_1}$, $R_2 = e^{-\gamma_0 L_2}$, the reflection coefficient is $\Gamma = \dfrac{\mu/\gamma - \mu_0/\gamma_0}{\mu/\gamma + \mu_0/\gamma_0}$, and the transmission coefficient is $z = e^{-\gamma L}$. Additionally, S21 for the empty waveguide is

$$S_{21}^0 = R_1 R_2 e^{-\gamma_0 L_a} \tag{3.25}$$

where $L_a = L_1 + L + L_2$

Finally, we get Eqs. (3.22), (3.23), (3.24), and (3.25), which are nine equations in total, to solve eight unknowns, $\varepsilon', \varepsilon'', \mu', \mu'', L_1, L_2, R_1$ and $R_2$.

### 3.4.4 Flip-chip FMR Measurement

The profile of the ferromagnetic resonance spectrum of a magnetic thin film, e.g. resonance peak position and linewidth, can be measured via a flip-chip FMR measurement. As shown in Figure 3.13 (a), a coplanar waveguide (CPW) is placed on aluminum housing with coaxial connectors on both sides to connect to the ports of VNA. The center pin of the connector is mechanically contacted to the CPW signal line, and the ground lines are connected to the aluminum housing. The structure of the CPW is schematically illustrated in Figure 3.13 (b). The fabrication of the CPW is done by sputtering of conducting films Ta(10nm)/Cu(800nm)/Au(100nm) and lift-off process. Alumina or GaAs wafer are adopted as the substrate. The impedance of a CPW depends on the thickness of the substrate, width of the signal line $W$ and the gap distance $S$ [9]. The impedance of the CPW was designed to be 50 Ω to match the impedance of the VNA. The thin films under test are placed face down on the CPW. The external magnetic field is applied parallel to the CPW by an electromagnet and is swept while VNA detects the S-parameters.

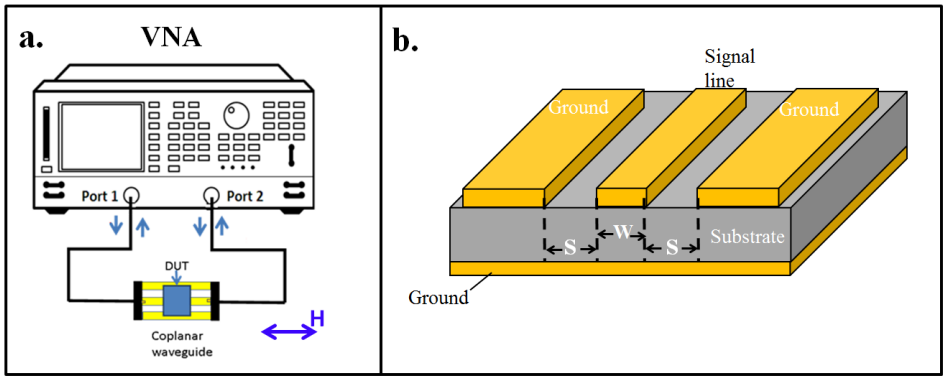


Figure 3.13 Schematics of (a) flip-chip FMR measurement (b) structure of a coplanar waveguide

A time domain FMR spectrum can be obtained by measuring the standard microwave S parameters as sweeping the external field. Under the assumption that the dominant CPW mode was the TEM mode and neglecting any reflection signal, the transmission S21 can be written as

$$S_{21}(H,\omega) \propto e^{in(H)\omega d/c} \tag{3.26}$$

where *n(H)* is the refractive index of CPW line as a function of external field *H*, $\omega$ is the angular frequency of microwave, *d* is the length of CPW line, *c* is the speed of the electromagnetic wave in vacuum.

The refractive index of CPW line can be written as

$$n(H) = n_0 + \delta\chi(H) \tag{3.27}$$

where $n_0$ is a constant which reflects the refractive index of CPW line without a magnetic sample, $\chi$(H) is susceptibility of the magnetic sample, $\delta$ is a constant

So by dividing a reference S21 to get rid of $n_0$, we can get relative susceptibility as [10]

$$\Delta\chi_{eff}(H) = \chi(H) - \chi(H_{ref}) = \frac{-ic}{\omega d\delta}\,\boldsymbol{log}\frac{S_{21}(H)}{S_{21}(H_{ref})} \tag{3.28}$$

where $S_{21}(H_{ref})$ is the S21 at saturation field $H_{ref}$.

## REFERENCES


[1] B. D. Cullity, "Elements of X-ray Diffraction, 2nd edition," Addison Wesley Publishing Company, Inc., 1978.

[2] A. Guinier, X-ray diffraction in crystals, imperfect crystals, and amorphous bodies: Courier Corporation, 1994.

[3] Y. Waseda, E. Matsubara, and K. Shinoda, X-ray diffraction crystallography: introduction, examples and solved problems: Springer Science & Business Media, 2011.

[4] "Lakeshore Vibrating Sample Magnetometer 7400 operational manual."

[5] "Reproduced from Agilent 8722ES S-parameter Vector Network Analyzer User's Guide, "http://cp.literature.agilent.com/litweb/pdf/08720-90392.pdf"."

[6] G. Miano and A. Maffucci, Transmission lines and lumped circuits: fundamentals and applications: Academic Press, 2001.

[7] J. Baker-Jarvis, E. J. Vanzura, and W. Kissick, "Improved technique for determining complex permittivity with the transmission/reflection method," Microwave Theory and Techniques, IEEE Transactions on, vol. 38, pp. 1096-1103, 1990.

[8] D. Smith, S. Schultz, P. Markoš, and C. Soukoulis, "Determination of effective permittivity and permeability of metamaterials from reflection and transmission coefficients," Physical Review B, vol. 65, p. 195104, 2002.

[9] C. P. Wen, "Coplanar waveguide: A surface strip transmission line suitable for nonreciprocal gyromagnetic device applications," Microwave Theory and Techniques, IEEE Transactions on, vol. 17, pp. 1087-1090, 1969.

[10] Y. Ding, T. J. Klemmer, and T. M. Crawford, "A coplanar waveguide permeameter for studying high-frequency properties of soft magnetic materials," Journal of Applied Physics, vol. 96, pp. 2969-2972, 2004.

# Chapter 4

## DAMPING DEPENDENCE IN MICROWAVE ASSISTED MAGNETIZATION REVERSAL

In ultrahigh density magnetic recording media, the grain size of magnetic media is reduced to increase the recording density. This will reduce the energy barrier, $K_uV$, between up and down magnetization states, where $K_u$ is the magnetic anisotropy and $V$ is the grain volume. With continuous reducing the bit size, the magnetic grain becomes paramagnetic due to the thermal fluctuation, which cannot be used to store the information. This effect is known as the superparamagnetic limit to the recording density. To maintain the thermal stability, the value of $K_u$ of the recording material is increased to keep the energy barrier $K_uV$ at least 60 times larger [1] than the thermal energy $k_BT$, where $k_B$ is the Boltzmann's constant, and $T$ is the working temperature. Consequently, it becomes harder to rewrite the information stored in the recording media, by overcoming the barrier energy to switch the magnetization. The competing requirements of stability, readability, and writeability that limit the recording capacity are known as the magnetic recording Trilemma [2, 3]. Microwave assisted magnetization reversal (MAMR) is one promising technique to mitigate the writability problem. The mechanism is illustrated in Figure 4.1. To reverse the magnetization from up state to down state, one can apply a magnetic field that generates Zeeman energy $-\mathbf{M}\cdot\mathbf{B}$ to overcome the energy barrier $K_uV$. In the presence of microwaves, the microwave magnetic field excites the large-angle precession of magnetization in both states which increases the energy of the magnet. The effective barrier energy is

thus reduced. One can, therefore, use the smaller magnetic field to switch the magnetization. Recent simulations [4-7] and experiments [8-10] have demonstrated the significant switching field reduction by the present of microwave fields. When the microwave frequency is close to the natural ferromagnetic resonance (FMR) frequency, the microwave is the most efficient in reducing the switching field, since the magnetization precession angle is the maximum at resonance.

The damping constant is another critical parameter in magnetization switching, which determines the switching time, on a scale of $1/\alpha\omega$, for the magnetization precession spiraling down to the direction along the external field. Generally, the damping has two opposite effects on the magnetization reversal. First, it determines the time of magnetization precession from a less stable to a more stable magnetic state after reversal, resulting in a so-called swing noise [11, 12]. The swing noise in giant magnetoresistive sensors is inversely proportional to damping. Second, the media damping can impede energy accumulation for magnetization switching [13]. One method to enhance the damping is to place a layer of a good spin-sink material next to the ferromagnetic layer. The spin-pumping explained this effect between normal and ferromagnetic materials [14-16]. On the other hand, simulation [17] by dynamic micromagnetic modeling indicates that microwaves become less efficient in reducing the switching field of the media with a high damping constant. Therefore, it is important to determine the optimal damping situation for practical applications. We will discuss the theoretical and experimental study on the damping dependence of microwave assisted magnetic switching in this chapter.

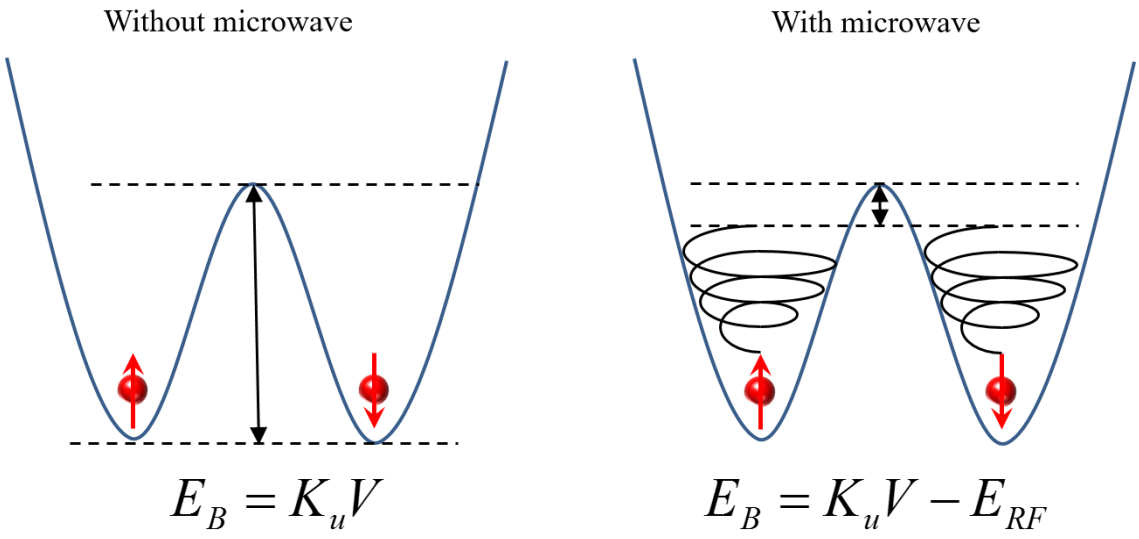


Figure 4.1 Illustration of microwave assisted magnetic reversal. The left panel shows the scenario when there is no microwave input. The right panel shows reduced energy barrier due to the microwave excited magnetization precession.

## 4.1 Numerical Simulation of Microwave Assisted Magnetization Reversal

The magnetic switching is simulated by solving LL equation numerically that ensures the unconditional preservation of the magnetization vector length. Different numerical methods can be used for the solution of the LL equation. A proper choice of the numerical methods requires a careful balance between calculation time and accuracy. To simplify the problem, one can approximately treat the magnetic sample as a single macro-spin.

The differential equation is approximately solved by the solution of initial value problem specified as

$$y' = f(t, y(t)) \tag{4.1}$$

$$y(t_0) = y_0 \tag{4.2}$$

where $y$ is an unknown function of time $t$, $y_0$ is the known initial value and $f(t,y(t))$ is the change rate of $y$ which is a function of $t$ and $y$ itself. We can rewrite LL Eq. (2.6) as

$$\mathbf{M}' = f(t, M(t)) \tag{4.3}$$

where $f(t, M(t)) = -\gamma\left[\mathbf{M}\times\mathbf{H} + \frac{\alpha}{M_s}\mathbf{M}\times(\mathbf{M}\times\mathbf{H})\right]$. The initial condition of magnetization is $\mathbf{M}(t_0) = \mathbf{M_0}$.

At the same time, the requirements of LL equation need to be satisfied

$$\mathbf{M}^2 = M_s^2 \tag{4.4}$$

$$\boldsymbol{M}\cdot\frac{d^2\boldsymbol{M}}{dt^2} = -\left(\frac{d\boldsymbol{M}}{dt}\right)^2 \tag{4.5}$$

Leonhard Euler developed the simplest first-order approximate method to solve the differential equation, named as Euler method. The value of the function in the next step $M_{n+1}$ is calculated for its present value $M_n$ as

$$M_{n+1} = M_n + hf(t_n, M_n) \tag{4.6}$$

$$t_{n+1} = t_n + h \tag{4.7}$$

where $h$ is the step size.

The drawback of this method is it does not satisfy Eq. (4.4) for the hold integration step $h$ in nature, resulting in an error $O(h)$. The error will accumulate as the calculation going forward, leading to significant distortion of the results.

To improve the calculation accuracy, one can use higher order methods, among which the 4th order Runge-Kutta method (RK4) is the most popular one. The value of the function in the next point $M_{n+1}$ is calculated for its present value $M_n$ as:

$$M_{n+1} = M_n + \frac{h}{6}(k_1 + 2k_2 + 2k_3 + k_4) \tag{4.8}$$

where

$k_1 = f(t_n, M_n)$

$$k_2 = f(t_n + h/2, M_n + hk_1/2)$$

$$k_3 = f(t_n + h/2, M_n + hk_2/2)$$

$$k_4 = f(t_n + h, M_n + hk_3)$$

The total accumulated error of RK4 is $O(h^4)$ which is much smaller than the Euler method. However, the calculation time is five-time longer.

To simulate the microwave assisted magnetic reversal, we model an ultrathin ferromagnetic film with saturation magnetization 1.5T and the effective uniaxial anisotropy field as 15 Oe along the *z*-axis. As depicted in Figure 4.2, the uniaxial anisotropy and a RF magnetic field $h_{rf}\,\boldsymbol{sin}\,\omega t$ is along the *x*-axis, and an external magnetic field $H_{ext}$ is applied along $-z$ direction to switch the magnetization. The code to simulate the magnetic reversal is shown in Appendix A1.

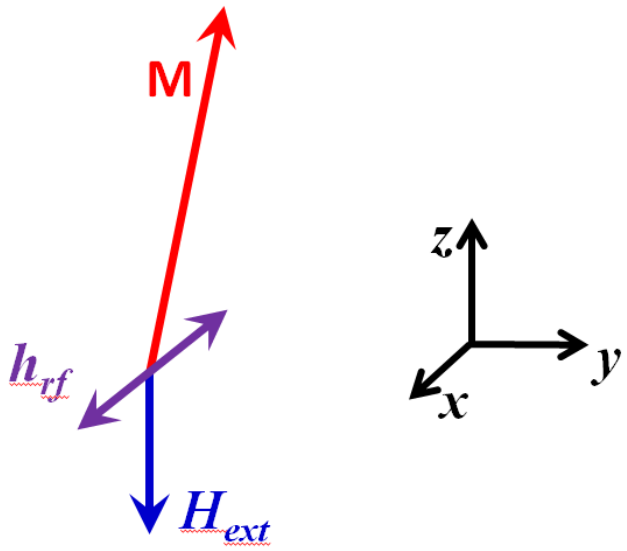


Figure 4.2 The configuration of magnetization and fields

The initial magnetization vector $\boldsymbol{M_0}$ = [5000, 0, 14142]. The demagnetization field is in the y direction as $h_d = \left[0,-M_y,0\right]$. The total effective field can be expressed as

$$H = H_{ext} + h_a + h_{rf} + h_d = \left[0,0,H_{ext}\right] + \left[0,0,15\times\frac{M_z}{M_s}\right] + \left[h_{rf}\,\boldsymbol{sin}\,\omega t,0,0\right] + \left[0,-M_y,0\right] \tag{4.9}$$

In the first scenario, a 15.5 Oe magnetic field $H_{ext}$ is applied along $-z$ direction which switches the magnetization direction. The magnetization vector rotates and finally stops along $-z$ direction as shown in Figure 4.3 (a). When the magnetic field is reduced to 10 Oe, the magnetization reversal does not occur as illustrated in figure 4.3(b), because the external field is less than the anisotropy field. In the third case, a RF magnetic field $h_{rf}$=10 Oe at 2GHz frequency is applied. The damping constant $\alpha = 0.02$. As shown in Figure 4.3 (c), the magnetization starts to precessing and the precession angle is keeping increasing. The precession angle becomes large enough that the precession overcomes the energy barrier and the $z$ component of magnetization reverse the sign. At the same time, the RF magnetic field is turned off. Finally, the precession energy is dissipated, and the magnetization settles down at $-z$-axis after some oscillations. The required switching field is significantly reduced from 15 Oe to 10 Oe due to the help of RF magnetic field. However, if the damping constant increased to 0.05 (Figure 4.3 (d)), the magnetization is only precessing around $+z$-axis without switching. Comparing Figure 4.3 (c) and (d), one can find the microwave assisted magnetic reversal is more efficient when the damping is small. By increasing the external magnetic field to be -13 Oe, the magnetic switching occurs, as shown in Figure 4.3 (e).

The swing noise is also investigated in the simulation. The swing noise is indicated by the time for the magnetization vector settling to its equilibrium direction. Comparing Figure 4.3 (c) and 4.3 (e), the magnetization vector needs more time to settle down when the damping is smaller. In conclusion, the materials with low damping will be accessible for microwave assisted magnetic reversal, but with large swing noise. For the real application, one should choose a ferromagnetic material with proper damping to balance the swing noise and switching efficiency.

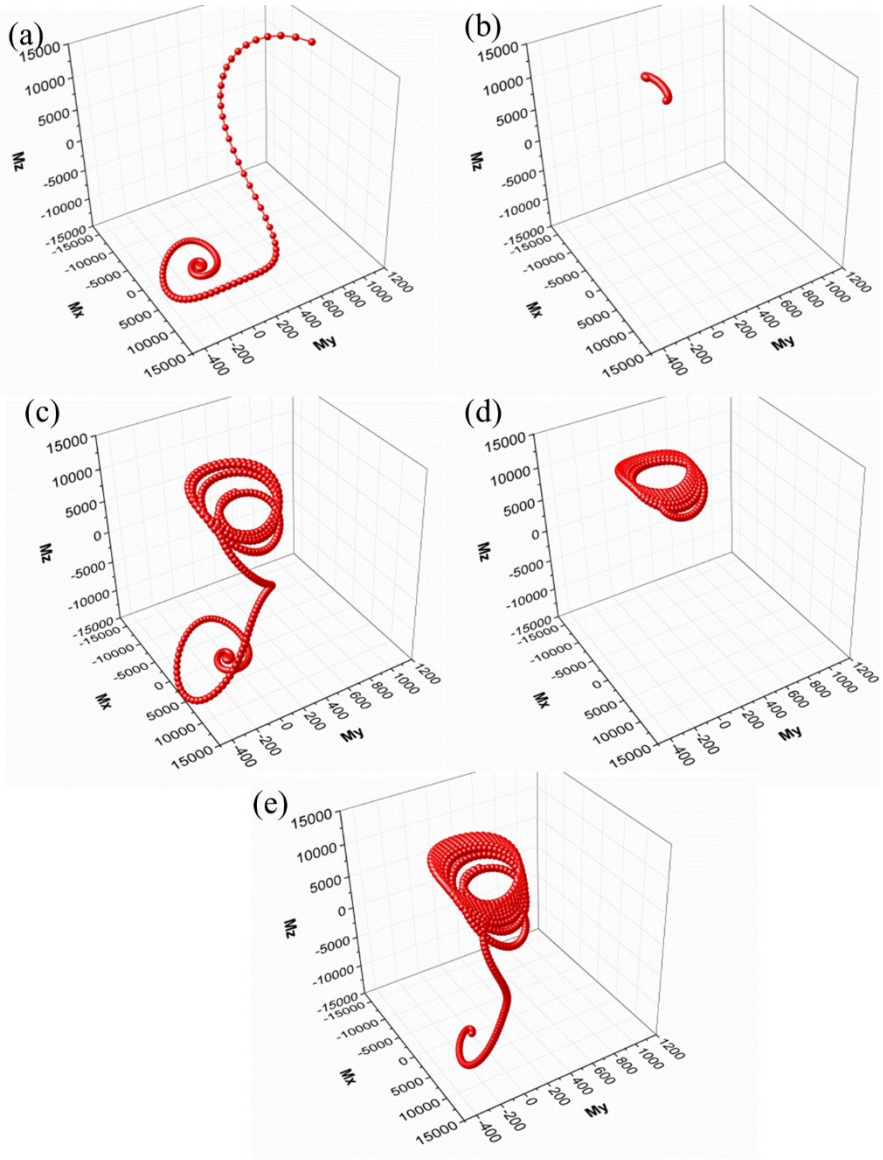


Figure 4.3 The evolution of magnetization under conditions (a) External magnetic field 15.5 Oe applied along –*z* direction and damping constant $\alpha = 0.02$ (b) External magnetic field 10 Oe applied along –*z* direction and damping constant $\alpha = 0.02$ (c) External magnetic field 10 Oe applied along –*z* direction, damping constant $\alpha = 0.02$, and microwave magnetic field $h_{rf}$=10 Oe (d) External magnetic field 10 Oe applied along –*z* direction, damping constant $\alpha = 0.05$, and microwave magnetic field $h_{rf}$=10 Oe (e) External magnetic field 13 Oe applied along –*z* direction, damping constant $\alpha = 0.05$, and microwave magnetic field $h_{rf}$=10 Oe

## 4.2 Microwave Techniques to Investigate Magnetic Dynamics of Micron-size Dots

To detect the magnetic dynamics of a small magnet, several techniques have been developed. Based on the particular detection scheme, these techniques are categorized into four types: mechanical methods, optical methods, electrical methods, and microwave methods. The mechanical methods are based on the magnetic force microscopy (MFM), which detects the magnetic dipolar force between the probe tip and the magnetic materials under test. The MFM is detected by measuring the average magnetic force change induced by magnetic precession. The method has the highest spatial resolution among all the detection techniques. However, the detection is limited to the surface of the magnetic material. The optical methods utilize magneto-optic effect: an electromagnetic wave is altered by the interaction with the magnetic field in a material. The magneto-optic Kerr magnetometer (MOKE) measures the polarization changes to light reflected from a magnetic surface to determine the magnetization. By measuring the time-averaged signal, MOKE observes the spatially resolved FMR of magnetic surfaces. The Brillouin light scattering (BLS) can measure spin wave dispersion by detecting the inelastically scattered light. The optical methods have advantages of high sensitivity, non-intrusive and good spatial resolution determined by the laser spot size which can be in sub-micron range. However, they require complicated optical circuits and instruments. The electrical methods investigate magnetic dynamics by spin-dependent electrical transport effects, such as anisotropic magnetoresistance (AMR), giant magnetoresistance (GMR) and tunneling magnetoresistance (TMR). The sensitivity of this method is determined by the MR value of the device. The principle of this method has been described in Chapter 2. The experiment details will be discussed in the next chapter.

The microwave methods have been widely used to study magnetic dynamics by detecting the change to microwave propagation due to magnetic susceptibility. Because they are sensitive and simple to carry out, the microwave methods are adopted in this study. In this thesis, I will discuss the algorithm and experiment setup of our newly designed microwave technique.

Coplanar waveguide (CPW) is adopted in our experiment microwave as a transmission line, which was fabricated by magnetron sputtering and lift-off process. As shown in Figure 4.4 (a), two CPWs with common short line were fabricated on silicon substrate. The whole structure was designed to be 50 Ohm to match the impedance of the Vector Network Analyzer (VNA). An Agilent 8753ES VNA generates microwaves, which are then amplified and applied to the CPWs by a pair of Cascade microwave air probes GSG-100. One 7 nm $\times$ 40 $\mu$m $\times$ 60 $\mu$m CoFeB dot covered by 20 nm Cu and 10 nm $SiO_2$ is patterned on the common short line through conventional photolithography and ion beam milling process. The easy axis of CoFeB is along the *x*-axis and is parallel to the CPW short line. An electromagnet produces external magnetic field $H_{ext}$ from 1000 Oe to 1000 Oe parallel to the easy axis.

As illustrated in Figure 4.4 (b), the RF magnetic field generated by microwave is confined to the common short line with a height comparable to the lateral size of the CPW. On the magnetic dot, the direction of the RF magnetic field is parallel to the *z*-axis. The small transmission S21 through the short line is via magnetic induction, which can be modeled as two inductive coupled loops as shown in Figure 4.4 (c), where two inductive loops formed by the two CPWs and magnetic dot. In this equivalent circuit, the CPWs can be treated as lumped impedance $Z_c$. The microwave transmission from left to right is through the mutual inductive coupling *M*.

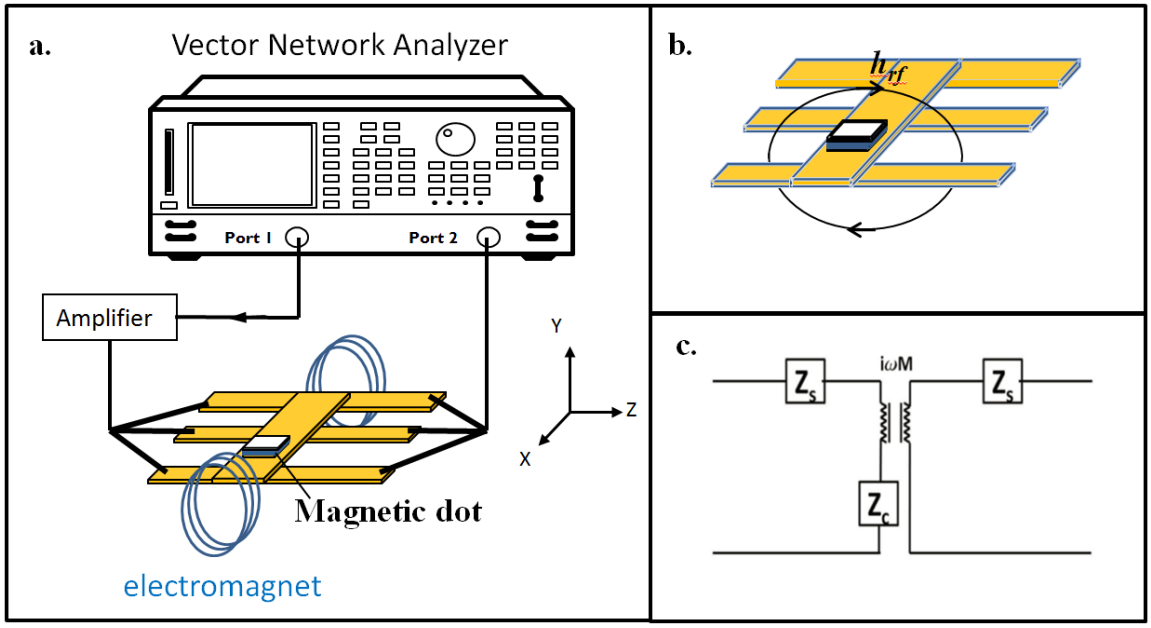


Figure 4.4 (a) The configuration of FMR measurement setup for testing magnetic dot. (b) Schematic of CPWs and magnetic dot on the common short line. (c) The equivalent circuit model.

The impedances of both source and load are $Z_s$ = 50 Ohm. Using microwave transmission line theory, one can relate the transmission S21 to the mutual inductance as

$$S_{21} = \frac{2}{1+\frac{Z_s}{Z_c}} \times \frac{ZZ_s}{Z^2 - Z_c Z_s} \tag{4.10}$$

where the first term one the right side is caused by the impedance mismatch between the feed-in circuit and the CPW, which is close to zero in the measurements, the second term is due to the inductive coupling, and the impedance of the inductive coupling $Z = j\omega M$ . Since $\omega M$ is much smaller than both $Z_c$ and $Z_s$, Eq. (4.10) can be simplified as $S_{21} = \frac{2j\omega M}{Z_c + Z_s}$.

The mutual inductance $M$ at the common short has two components as $M = A + B\mu$, where the first term is the magnetic induction of the common short in

the absence of magnetic film, and the second term is the induction through the magnetic thin film, which is proportional to its permeability. Here both $A$ and $B$ are geometric factors and are independent of external magnetic field. Therefore, the transmission S21 can be written as

$$S_{21}[\omega, H] = Te^{j\phi[\omega]}\left(\frac{2j\omega B\mu}{Z_s + Z_c} + S_{mbg} + S_{ebg}\right) \tag{4.11}$$

where $T$ is the transmission coefficient of microwave cables and probes, $\phi$ is the phase change due to the wave propagation in the CPW, $S_{mbg}$ and $S_{ebg}$ are respectively the background signals due to inductive coupling through the air and electric coupling. Because $S_{mbg}$ and $S_{ebg}$ are independent of the magnetic dot and external magnetic field, the relative magnetic susceptibility (or permeability) can then be extracted by subtracting the transmission signal measured at different external magnetic fields as

$$\chi[\omega, H] - \chi[\omega, H_{ref}] \propto \frac{S21[\omega, H] - S21[\omega, H_{ref}]}{j\omega} \tag{4.12}$$

where $H_{ref}$ is the reference magnetic field that is equal to 1000 Oe field in the measurements, which saturates the magnetization of the magnetic dot. The VNA measures the S21 at several frequencies with sweeping the external magnetic field. Then the relative magnetic permeability is calculated from Eq. (4.12). After measuring the relative permeability at all of the field points in between 1000 Oe to 0 Oe, one can get the FMR spectrum by plotting the relative susceptibility as a function of the external magnetic field, shown in Figure 4.5. An empirical phase term $e^{j\phi}$ is added during the fitting process to compensate the prefactor in Eq (4.11). The FMR linewidth and resonance field can be obtained accurately by fitting the FMR spectrum with the Lorentzian function. From Figure 4.5, the resonance field is fitted to be

$408.6 \pm 0.006$ Oe and the linewidth is $44.4 \pm 0.02$ Oe. The error of the fitting is very tiny.

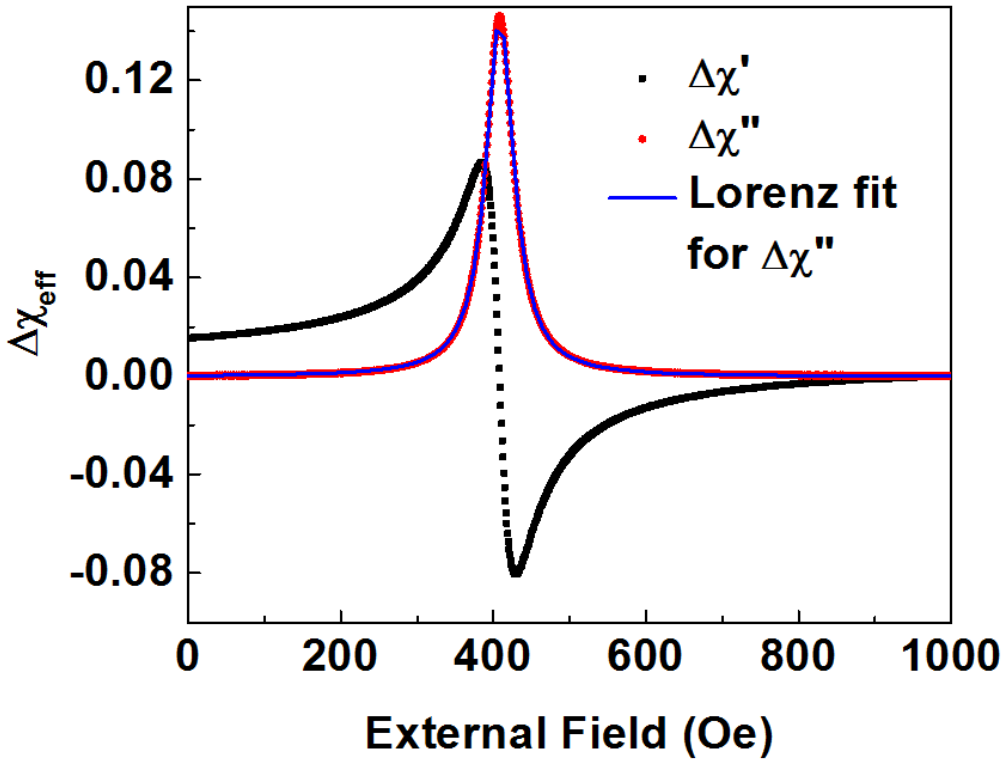


Figure 4.5 An exemplary FMR spectrum extracted from Eq. (4.12). The real part of susceptibility is plotted in black, the imaginary part of susceptibility is plotted in red, and the Lorentzian fit is plotted in blue. The sample was 80 nm $Fe_{30}Co_{70}$.

The effective saturation magnetization $M_{eff}$ and anisotropy field $H_a$ can be extracted from the Kittle equation

$$f_r = \frac{\gamma}{2\pi}\sqrt{(H_r + H_a + 4\pi M_{eff})(H_r + H_a)} \tag{4.13}$$

where $H_r$ is the magnetic field at the FMR peak. The interface perpendicular uniaxial anisotropy the effective saturation magnetization $4\pi M_{eff} = 4\pi M_s - 2K_u^s / M_s$, where

$K_u^s$ is the energy of the interface anisotropy. Since the effective saturation magnetization is much larger than $H_r$ and $H_a$, Eq. (4.13) can be simplified as

$$f_r^2 = (\frac{\gamma}{2\pi})^2 4\pi M_{eff}(H_r + H_a) \tag{4.14}$$

The square of FMR frequency is thus linear with the FMR field.

By plotting FMR field verse square of FMR frequency, the $M_{eff}$ and $H_a$ are extracted from linear fitting.

The precession damping is related to FMR linewidth by

$$\alpha = \frac{1}{2}\frac{\gamma}{2\pi}\frac{d(\Delta H)}{df} \tag{4.15}$$

where $\Delta H$ is the FMR linewidth. According to Eq. (4.15), the slope of the linear fitting corresponds to the dimensionless damping constant α.

## 4.3 Engineer the Damping by Spin Pumping

Damping constant describes the dissipation of magnetization precession energy and consequent reduction of the precession angle. Several mechanisms contribute to the magnetic damping. These mechanisms typically fall into two categories: extrinsic damping and intrinsic damping. The extrinsic damping is mainly due to the structure defects and complex geometrical features which are sample dependent. The intrinsic damping arises from the intrinsic relaxation mechanisms involving interaction between the electrons, phonons and thermally excited magnons.

To investigate the dependence of magnetic reversal on the damping, the damping should be controlled without altering other magnetic properties such as the saturation magnetization and magnetic anisotropy. The spin pumping in multilayers can fulfill the requirements and is adopted in the study.

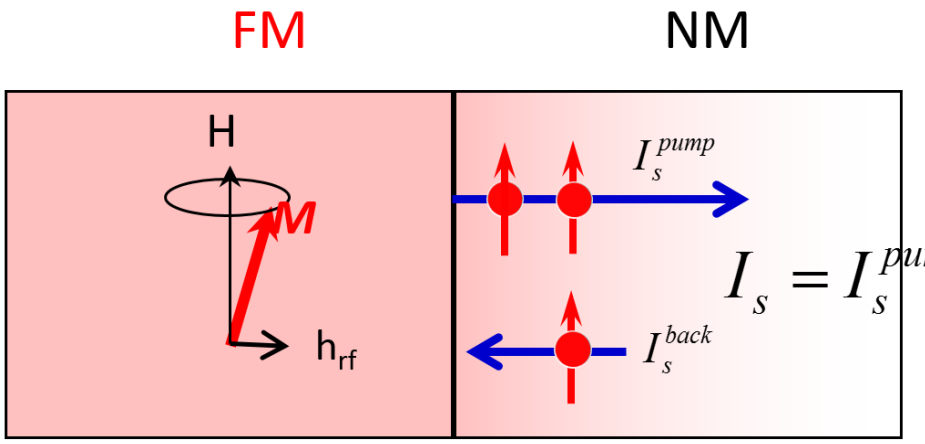

Figure 4.6 The schematic illustration of spin pumping

As depicted in Figure 4.6, spin pumping occurs at a system composed of a ferromagnet (FM) and a normal-metal (NM). The magnetization precession in FM generates spin-polarized current into the adjacent NM. If the NM has strong spin-orbital interaction, it absorbs the injected spins, leading to additional spin relaxation to FM. For ultrathin (<10nm) ferromagnetic films, the spin pumping may lead to a significant enhancement of the damping constant. This phenomenon can be understood by the reflection and transmission of spin current in the system. In a FM-NM bilayer, the magnetization $M$ precesses around the external magnetic field. A spin current $I_s^{pump}$ is pumped into NM causing spin accumulations in NM layer. This spin accumulation will diffuse to both directions and introduces a backflow spin current $I_s^{back}$. The net spin current out of the FM is $I_s = I_s^{pump} - I_s^{back}$. By conservation of angular momentum, the spin ejected by $I_s$ corresponds to torque on FM. Hence, a term due to spin pumping current is added into a modified LLG equation as

$$\frac{d\,\boldsymbol{m}}{dt} = -\gamma\,\boldsymbol{m}\times\boldsymbol{H}_{eff} + \alpha_0\,\boldsymbol{m}\times\frac{d\,\boldsymbol{m}}{dt} + \frac{\gamma}{M_s V}\boldsymbol{I}_s \tag{4.16}$$

where $\alpha_0$ is the intrinsic dimensionless Gilbert damping only due to the ferromagnet itself. The third term in Eq. (4.16) causes an additional contribution $\alpha'$ to the total Gilbert damping $\alpha = \alpha_0 + \alpha'$.

There are two extreme scenarios. If no spin-scattering occurs in NM, the pumped spin current is completely reflected back. Consequently, the enhanced damping $\alpha'$ is zero. If the NM is a good spin sink, the pumped spins are entirely absorbed by the NM. One can employ spin diffusion model to derive an expression for the additional damping as

$$\alpha' = \frac{g_L g^{\uparrow\downarrow}}{4\pi\mu} \tag{4.17}$$

where $g_L$ is the $g$ factor, $g^{\uparrow\downarrow}$ is spin mixing conductance, and $\mu$ is the magnetic moment of the FM in a unit of $\mu_B$.

Two typical NM materials, copper and platinum, are deployed here to adjust the damping constant. Copper (Cu) is considered as a spin transparent material, which is manifested by its long spin diffusion distance (>200nm); While heavy-metal platinum (Pt) has strong spin-orbital interaction and is capable of relaxing all nonequilibrium spins. For poor spin-sink materials, such as Cu and Al, there will be backflow spin currents which lead to a consistent damping. If the normal metal is a good spin-sink material, such as Pt, the injected spins will be relaxed rapidly, resulting in an increase in the damping constant. Therefore, the damping can be tuned by varying the combination of Cu and Pt layers. To demonstrate this scheme, we measured the damping constant with FMR of three types of magnetic dots composed of Cu(20 nm)/CoFeB(7 nm)/Cu(20 nm), Cu(20 nm)/CoFeB(7 nm)/Cu(5 nm)/Pt(20 nm), and Cu(20 nm)/CoFeB(7 nm)/Pt(20 nm). We characterize the damping and

saturation magnetization of these magnetic dots through CPW measurements. The nominal microwave power is fixed at -10 dBm. The 20 nm Cu layer under the CoFeB provides the same bottom interface. The easy axis of CoFeB is along the *x*-axis and is parallel to the CPW common short line. Figure 4.7 shows the typical FMR spectrum of the three samples. One can see the linewidth of the FMR peak is broadened due to the present of Pt capping layer. The direct growth of Pt on top of CoFeB gives rise to the widest FMR peak due to the strong spin-orbital coupling in Pt and the inserted Cu between CoFeB and Pt weakens the enhancement of the damping. Figure 4.8 (a) shows a linear dependence of the FMR linewidth on the frequency. According to Eq. (4.15), the slope of the linear fitting corresponds to the dimensionless damping constant, which is determined to be 0.011, 0.0079 and 0.0061 for CoFeB/Pt, CoFeB/Cu/Pt, and CoFeB/Cu, respectively. At FMR, the resonance field is proportional to the square of the microwave frequency as shown in Figure 4.8 (b). The slope of the three curves is the same, indicating the same saturation magnetization $M_s$=1.5 T for all three samples. The intercept of the line is determined by the anisotropy field of the film, which is slightly different due to the various interfaces in CoFeB/Cu and CoFeB/Pt. We also used VSM to measure the magnetic properties of the three samples. After the film deposition, the samples were cut into small squares with 5 mm × 5 mm size. Figure 4.9 shows the hysteresis loops of the three samples measured by VSM. There is a small diamagnetic background single arising from the silicon substrate and sample holder. The saturation magnetization is the same, and the coercivity fields are very close to each other, which confirm the results of FMR measurements.

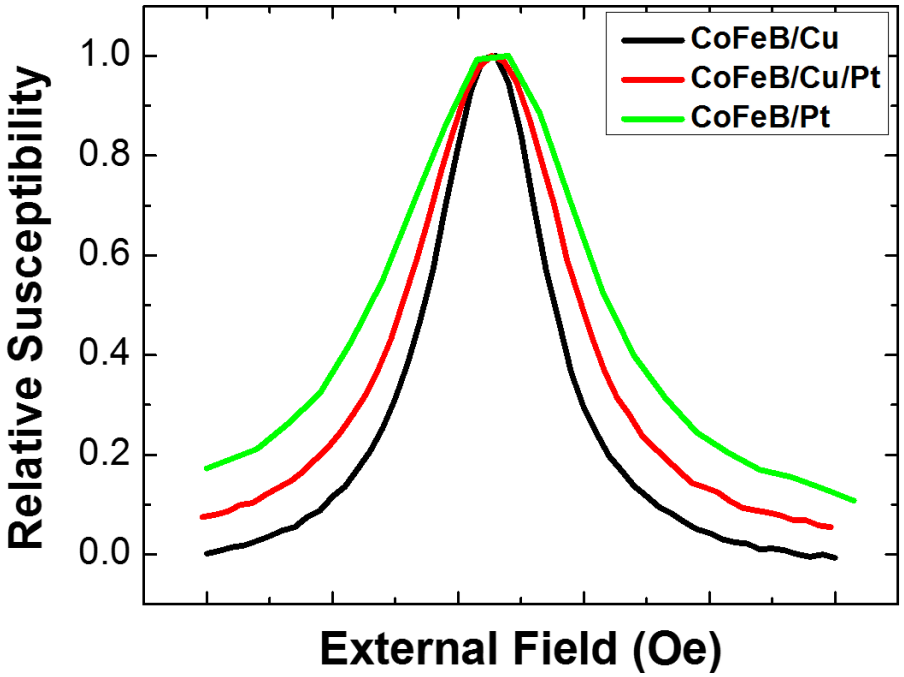


Figure 4.7 Exemplary FMR spectrum of CoFeB(7nm)/Cu(20nm), CoFeB(7nm)/ Cu(5nm)/ Pt(20nm), CoFeB(7nm)/ Pt(20nm) magnetic dots

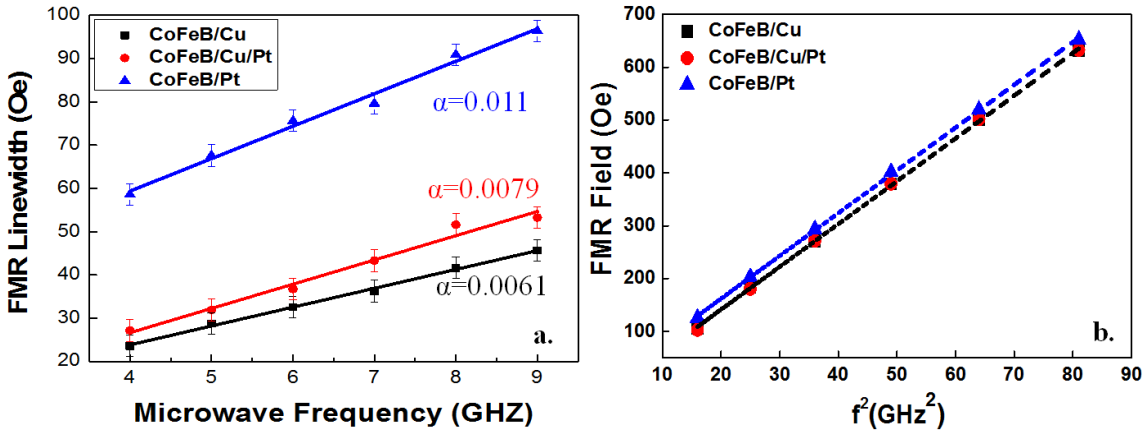


Figure 4.8 (a) The FMR linewidth vs. the microwave frequency for three samples. Extracted damping are 0.011, 0.0079, 0.0061 as labeled next to the curves. (b) The FMR resonance field vs. the square of microwave frequency for three samples.

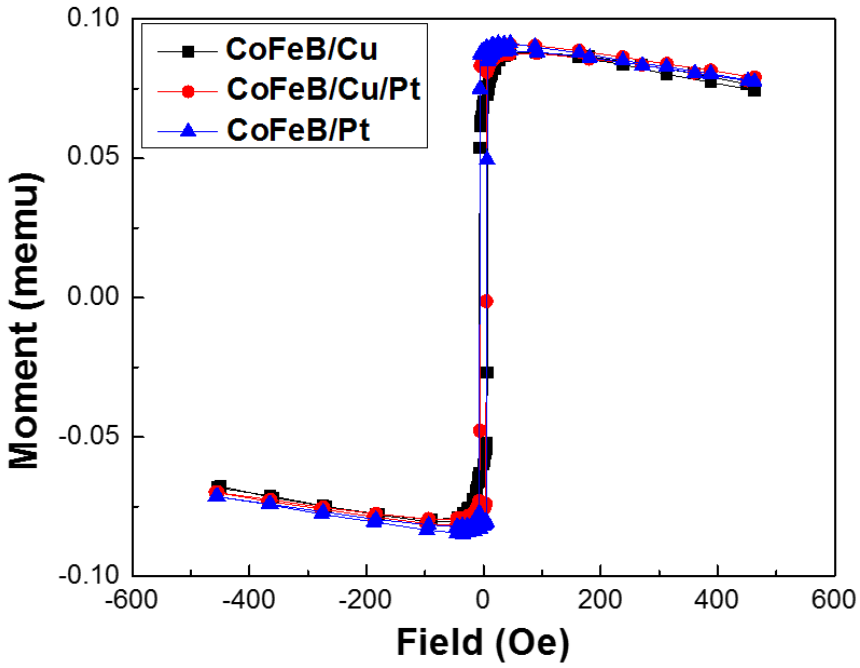

Figure 4.9 The magnetic hysteresis loop of three samples measured by VSM

## 4.4 Determine Magnetic Reversal by Susceptibility Spectrum

In the previous two sections, we've developed a new scheme to extract FMR susceptibility spectrum and demonstrated the engineering of magnetic damping by spin pumping. Conventionally, the FMR was detected at magnetization saturation state, where the magnetization precesses coherently throughout the whole sample. The saturation magnetization, magnetic anisotropy, and damping are extracted from FMR at saturation state. To study the magnetic reversal, we measured susceptibility spectrum near the magnetic switching region.

The Stoner-Wohlfarth model is a simple model to describe the magnetization behavior of a single-domain ferromagnetic particle. For an ultrathin ferromagnetic film with uniaxial anisotropy, the total magnetic energy is

$$E = -H_{ext} M_s \cos(\theta - \phi) - \frac{K_u}{2} \cos^2 \phi \qquad (4.18)$$

where $K_u$ is the uniaxial anisotropy energy, $\theta$ and $\varphi$ are the polar angle of magnetization and external magnetic field respectively. The first term is Zeeman energy and the second term is the magnetic anisotropy energy.

When the field is applied along the easy axis, the effective field of the ferromagnetic film can be calculated from the first derivative of the total magnetic energy as

$$H_{eff} = -\frac{\partial E}{\partial M} = H_{ex} + \frac{2K_u}{M_s} = H_{ex} + H_a \tag{4.19}$$

The effective anisotropy field $H_a = \frac{2K_u}{M_s}$. The magnetic susceptibility is field dependent as $\chi[H_{eff}, \omega]$. The magnetization changes from $+M_z$ to $-M_z$ at magnetization reversal. As a result, the susceptibility will have a change of $\chi[H + H_a, \omega] - \chi[H - H_a, \omega]$ near the switching region.

We performed an experiment with a sputtered 80nm $Fe_{30}Co_{70}$ thin film. Both magnetic hysteresis loop and the susceptibility spectrum near the switching region are measured and plotted in Figure 4.10. The switching in the susceptibility spectrum happens at the same field as magnetization switching. This abrupt change in the susceptibility is a useful indication of the magnetization switching in the study of a microwave-assisted magnetization reversal.

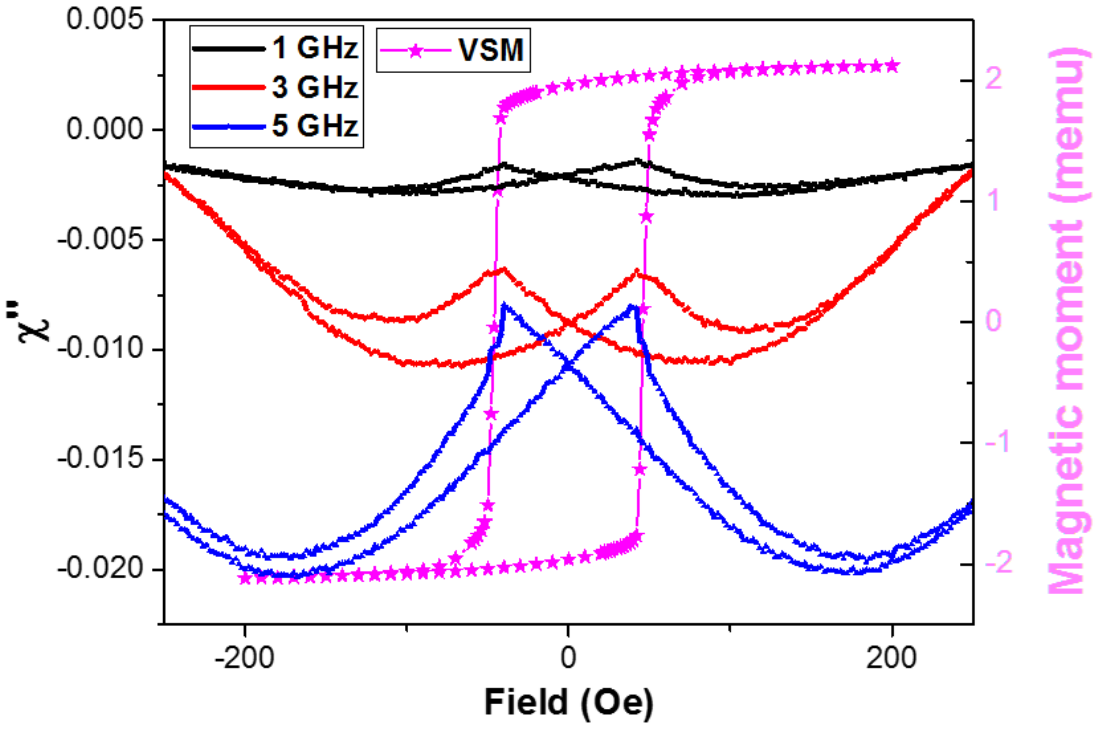


Figure 4.10 Magnetic susceptibility spectrum at different frequencies and the magnetic hysteresis loop measured with VSM. The switching in susceptibility and hysteresis loop occur at the same field.

## 4.5 Investigate the Damping Dependence of MAMR

We first measure the evolution of switching behaviors of CoFeB/Cu sample under various microwave power. The microwave frequency is 2 GHz, and the nominal microwave power is in the range of 0 dBm to 20 dBm. Figure 4.11 (a) shows the phase of S21 near the switching. Comparing with the susceptibility spectrum illustrated in Figure 4.10, one can see the spectrum of the phase of S21 is much clearer to indicate the magnetic switching. The abrupt change of S21 is due to the magnetic switching. The switching field shifts with the microwave power. We plot the magnetic switching as a function of the microwave power in Figure 4.11 (b). The switching field decreases with the increase of the microwave power because the magnetic dot can

absorb more energy from microwave to overcome the energy barrier. When the microwave power is larger than 10 dBm, the switching field drops significantly. As the microwave power is increased to 20 dBm, the switching field is decreased by as much as 60%. Moreover, microwaves at 2 GHz are more efficient in reducing the switching field than using microwaves at 2.5 GHz.

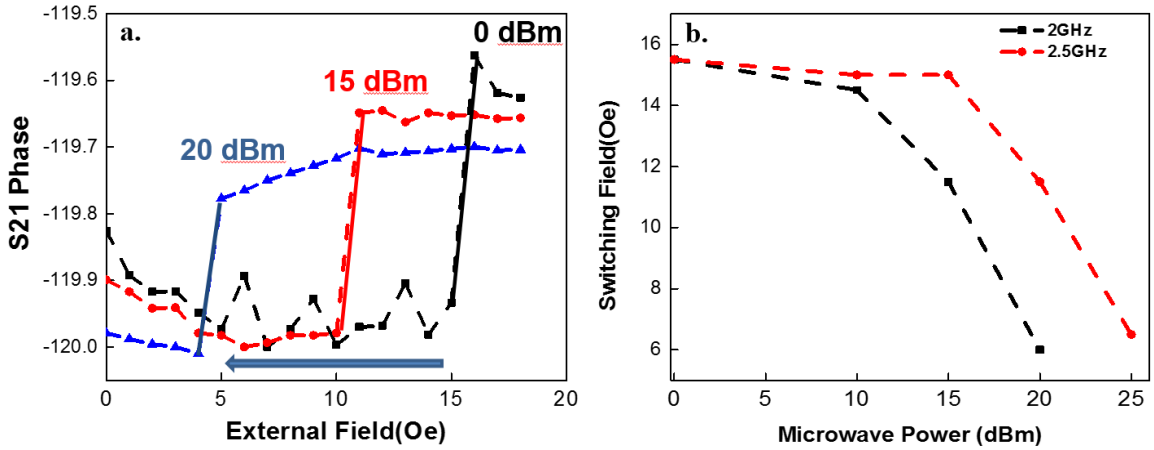


Figure 4.11 (a) The phase of S21 as a function of the external magnetic field at microwave power of 0 dBm, 15 dBm, and 20 dBm. (b) The switching field as a function of the microwave power at 2 GHz and 2.5 GHz.

To study the influence of damping on the reduction of the switching field, we measured the switching field vs. the microwave power curves of three samples with different damping constants. The damping constant shows a significant effect on MAMR. The material with lower damping requires smaller switching field with the same microwave. As shown in Figure 4.12 (a), at 20 dBm microwave power, the switching field CoFeB/Cu ($\alpha = 0.0061$) is reduced by 60% as compared with the 20% reduction in CoFeB/Pt ($\alpha = 0.011$) sample. As shown in Figure 4.12 (b), a numerical simulation of the power and damping dependence of the switching field was done by solving the LLG equation under a single domain assumption, the magnetic dot is

treated as a single macro-spin, and the thermal effect is neglected. The extracted damping constants and saturation magnetization of the three samples extracted from Figure 4.8 are used in the calculation. The trend of the switching behavior is qualitatively reproduced, even though there is a quantitative difference between the experimental and numerical results, especially in the low power region. Then we consider the thermal effect. For magnetic materials with a smaller damping, the precession angle is larger under the same microwave excitation. Therefore, it might convert more energy into heat. With the increase of temperature, the magnetic dot becomes easy to be switched. It is important to estimate the maximum temperature increase at the highest microwave power to evaluate the heating effect. The heating sources in the CPW can be considered as two contributions, magnetic loss, and electrical loss. The power absorbed at FMR can be estimated by $P_{FMR} = \frac{h_{rf}^2}{\mu_0} \chi'' \omega A t_{FM}$, where numerical simulation revealed $h_{rf}$~14 Oe at 2 GHz with 25 dBm, $\chi''$ ~50 is the imaginary part of the susceptibility at FMR and $At_{FM}$ is the volume of the ferromagnetic dot. The upper limit for the temperature increase due to FMR can be estimated from steady-state heating on the Si substrate, where $t$=250 μm is the thickness of Si substrate and $\kappa$=92.7 W/(m·K) is the effective thermal conductivity of the substrate calculated by $\kappa = \frac{d_1 + d_2}{d_1/\kappa_1 + d_2/\kappa_2}$ because there is a $SiO_2$ surface layer of about 1 μm. The estimated maximum temperature rise is as small as 0.01 K at FMR. For the electric loss in the 50 μm wide CPW with the length of 1mm, no more than 20% microwave energy is dissipated, since the sum of reflection and transmission are more than 80%. If the losses were uniformly distributed along the CPW, at $P$=25 dBm, the electric loss would increase temperature $\Delta T = \frac{t(0.2P)}{\kappa A}$ ~3.4 K. These estimations

are consistent with results reported in Ref [10]. The heating effect can be neglected in the reduction of switching field.

The efficiency of microwaves on switching also depends on the frequency of microwave. The phenomenon is predicted by the numerical simulation and easy to understand because the precession angle is maximum at the resonance frequency. We plot the normalized switching field as a function of microwave frequency in Figure 4.12 (c). The switching field is normalized to the maximum value in the frequency range from 0.75 GHz to 3.25 GHz. The nominal microwave power is kept as 15 dBm. There is a deep around 1.5 GHz for all three samples with different damping constants. The most efficient frequency is close to the FMR frequency of CoFeB, which is not damping related.

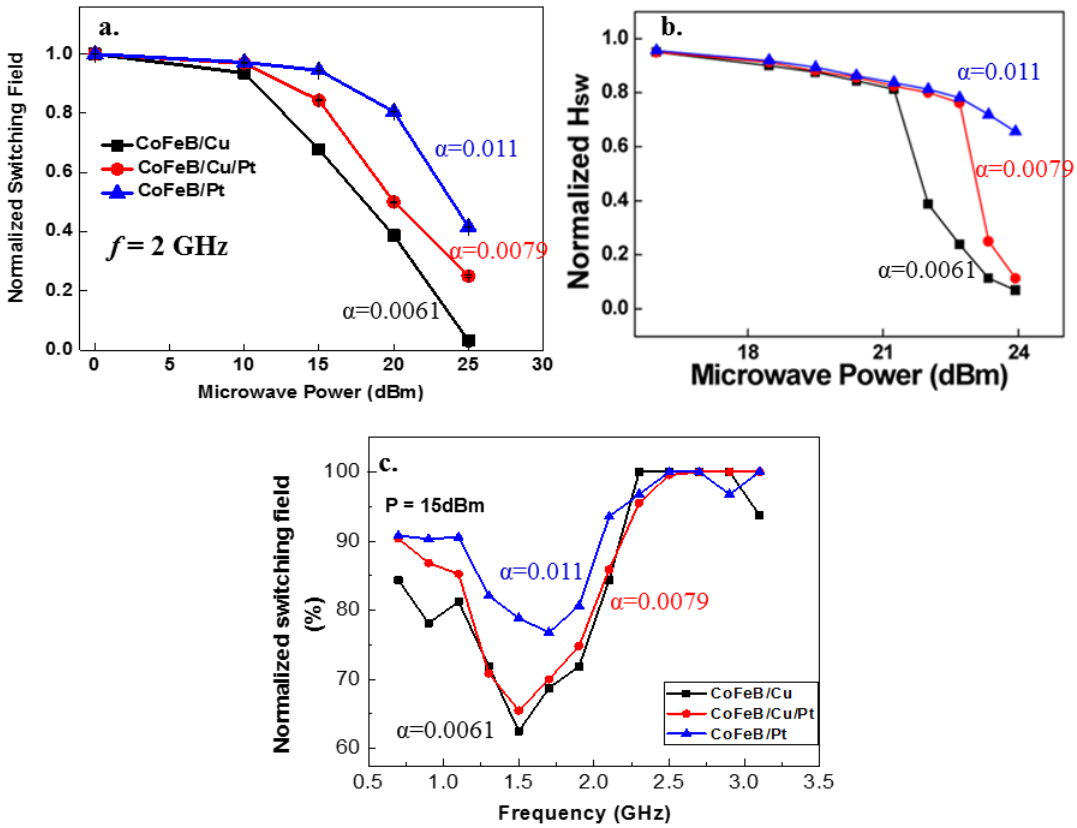


Figure 4.12 (a) The normalized switching field as a function of the microwave power. (b) The simulation results of normalized switching field for three films with different damping constants. (b) The frequency dependence of MAMR. The normalized switching field as a function of the microwave frequency at a fixed power of P=15dBm. In the frequency range from 0.7 to 3.1 GHz, three samples show similar frequency dependence, having a minimum value at an optimal frequency $f_{opt}$. This occurs when the FMR peak field is close to the switching field, and the magnetization is processing at maximum angles. When the frequency is far away from $f_{opt}$, the effect is attenuated.

## REFERENCES


[1] S. N. Piramanayagam, "Perpendicular recording media for hard disk drives," *Journal of Applied Physics,* vol. 102, p. 011301, 2007.

[2] C. Thirion, W. Wernsdorfer, and D. Mailly, "Switching of magnetization by nonlinear resonance studied in single nanoparticles," *Nature Materials,* vol. 2, pp. 524-527, Aug 2003.

[3] G. W. Qin, Y. P. Ren, N. Xiao, B. Yang, L. Zuo, and K. Oikawa, "Development of high density magnetic recording media for hard disk drives: materials science issues and challenges," *International Materials Reviews,* vol. 54, pp. 157-179, May 2009.

[4] M. Igarashi, Y. Suzuki, H. Miyamoto, Y. Maruyama, and Y. Shiroishi, "Mechanism of microwave assisted magnetic switching," *Journal of Applied Physics,* vol. 105, Apr 2009.

[5] S. Okamoto, M. Igarashi, N. Kikuchi, and O. Kitakami, "Microwave assisted switching mechanism and its stable switching limit," *Journal of Applied Physics,* vol. 107, Jun 2010.

[6] S. Okamoto, N. Kikuchi, and O. Kitakami, "Frequency modulation effect on microwave assisted magnetization switching," *Applied Physics Letters,* vol. 93, pp. 142501, Oct 6 2008.

[7] K. Rivkin, N. Tabat, and S. Foss-Schroeder, "Time-dependent fields and anisotropy dominated magnetic media," *Applied Physics Letters,* vol. 92, pp. 153104 , Apr 14 2008.

[8] T. Moriyama, R. Cao, J. Q. Xiao, J. Lu, X. R. Wang, Q. Wen*, et al.*, "Microwave-assisted magnetization switching of Ni80Fe20 in magnetic tunnel junctions," *Applied Physics Letters,* vol. 90, Apr 2007.

[9] C. Nistor, K. Sun, Z. H. Wang, M. Z. Wu, C. Mathieu, and M. Hadley, "Observation of microwave-assisted magnetization reversal in Fe65Co35 thin films through ferromagnetic resonance measurements," *Applied Physics Letters,* vol. 95, pp. 012504 , Jul 6 2009.

[10] G. Woltersdorf and C. H. Back, "Microwave assisted switching of single domain Ni80Fe20 elements," *Physical Review Letters,* vol. 99, pp. 227207, Nov 30 2007.

[11] C. Y. Mao, J. G. Zhu, R. M. White, and T. Min, "Effect of damping constant on the switching limit of a thin-film recording head," *Journal of Applied Physics,* vol. 85, pp. 5870-5872, Apr 15 1999.

[12] H. N. Bertram, Z. Jin, and V. L. Safonov, "Experimental and theoretical studies of thermal magnetization noise in GMR heads," *Ieee Transactions on Magnetics,* vol. 38, pp. 38-44, Jan 2002.

[13] Z. H. Wang and M. Z. Wu, "Chirped-microwave assisted magnetization reversal," *Journal of Applied Physics,* vol. 105, pp. 093903, May 1 2009.

[14] S. Mizukami, Y. Ando, and T. Miyazaki, "Effect of spin diffusion on Gilbert damping for a very thin permalloy layer in Cu/permalloy/Cu/Pt films," *Physical Review B,* vol. 66, pp. 104413, Sep 1 2002.

[15] Y. Tserkovnyak, A. Brataas, and G. E. W. Bauer, "Enhanced Gilber damping in thin ferromagnetic films," *Physical Review Letters,* vol. 88, pp. 117601, Mar 18 2002.

[16] M. V. Costache, M. Sladkov, S. M. Watts, C. H. van der Wal, and B. J. van Wees, "Electrical detection of spin pumping due to the precessing magnetization of a single ferromagnet," *Physical Review Letters,* vol. 97, pp. 216603, Nov 24 2006.

[17] Y. M. Wang, Y. H. Tang, and J. G. Zhu, "Media damping constant and performance characteristics in microwave assisted magnetic recording with circular ac field," *Journal of Applied Physics,* vol. 105, pp. 07B902, Apr 1 2009.

# Chapter 5

## MAGNETIC TUNNEL JUNCTION WITH PERPENDICULAR MAGNETIC ANISOTROPY

In 1956, the first hard disk drive (HDD) was first invented by IBM with an areal density of 2 Kbit/in$^2$ [1]. The recording media used in the first HDD was aluminum coated with $\gamma$-iron oxide in an epoxy base. With the development of new magnetic recording physics, new magnetic materials, and advanced signal process methods, the areal recording density of HDD dramatically increased to be above 1.3 Tbit/in$^2$ as of 2015 [2], which is $10^8$ times more density than the first device. For decades, the HDD industry has focused on the so-called longitudinal magnetic recording [3] in which the magnetization of the recording media lies in the plane of the disk. As illustrated in Figure 5.1, the information, i.e. the binary digit 0 or 1, is indicated by the magnetization orientation of the magnetic grains (bits) pointing to the left or right. The read/write head is composed of a magnetic sensor and electromagnet that generates magnetic field to switch the magnetization of the data bits. With the increase of areal density, the bits become smaller and closer to each other. The demagnetizing field rising from dipole-dipole interaction is enhanced, similar to two magnetic dipoles placed in a line repelling each other. Moreover, the magnetic anisotropy energy of the bits is reduced with the grain volume. Coercivity is increased via increasing of the magnetic anisotropy energy to counteract the demagnetizing field and maintain the stability of the bits under thermal fluctuations. As a result, there is a theoretical limit of the longitudinal recording as 200 Gbits/in$^2$ [4]. In perpendicular

recording, the magnetization of each data bit is aligned perpendicular to the disk plane [5-8]. In this geometry, the dipolar energy between adjacent magnetic grains is small so that the demagnetizing field is not significant enhanced with grain size reduction. In addition, a magnetic soft undrelayer below the recording layer conducts and concentrates magnetic flux to enhance the write field, which allows magnetic materials with high coercivity to be used. The soft underlayer also increases the total thickness of the recording layer, leading to an enhanced magnetic signal for the read heads. All of these benefits ensure the steady increase of recording density in HDD.

In a hard drive device, the stored information is rewritten by reversing the magnetic moment of the bits via a magnetic field. The writing process is energy consuming because it requires a large electric current to generate the write field. The reading speed is also limited by the mechanical movement of the read head flying with nm distance above the disk surface.

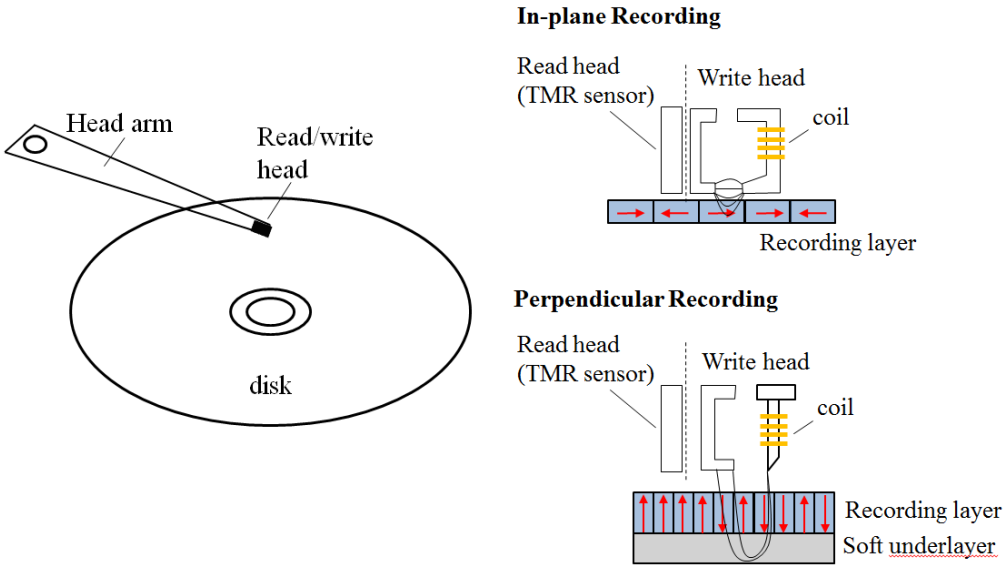


Figure 5.1 The schematics of a hard disk drive, in-plane recording, and perpendicular recording [3].

Different mechanisms have been proposed and used in the new generation of magnetic recording devices. One promising candidate is spin-transfer-torque magnetic random access memory (STT-MRAM) [9-12]. The primary devices are magnetic tunnel junctions where the electric resistance, as the sensing signal of stored information, is determined by the orientation of magnetization. The spin polarized current interacts with local spin angular momentum to flip the magnetization, as referred to spin-transfer switching. To generate the spin-polarized current, an electric current is needed to flow through an FM polarizer [13] or materials with strong spin-orbital interaction [14-16]. The process still costs energy due to the finite resistance of the device. To further reduce the energy consumption, a nonvolatile magnetoelectric (ME) device was proposed, which is composed of an antiferromagnetic insulator, such as chromia α-Cr2O3 (0001), and an MTJ with perpendicular magnetic anisotropy grown on top of chromia. The schematic structure is depicted in Figure 5.2. The antiferromagnetic chromia is a typical ME material [17] that its surface magnetic momentum $M^i$ is induced by an electric field with a component $E^j$ with an ME coefficient $\alpha_{me}^{ij}$ according to $\mu_0 M^i = \alpha_{me}^{ij} E^j$. The surface magnetic state can be controlled by the voltage applied on the chromia. The surface momentum is normal to the surface plane and coupling to the bottom electrode of the perpendicular MTJ via exchange interaction, referred to exchange bias. The read of the information is through measuring the resistance of the MTJ. Robust room-temperature voltage-controlled magnetic switching has been achieved in heterostructures composed of chromia and FM thin films with PMA, such as Co/Pd or Co/Pt multilayers [18]. In the nonvolatile ME device, the energy consumption of writing is ultra-low because there are no resistive elements in the switching mechanism. Table 5.1 summarizes the

performance of HDD, STT-MRAM, and ME memory devices. The fabrication of MTJs with PMA and integration of MTJs with chromia are essential for making the ME device. In this chapter, I will discuss the development of magnetic thin films and MTJs with PMA.

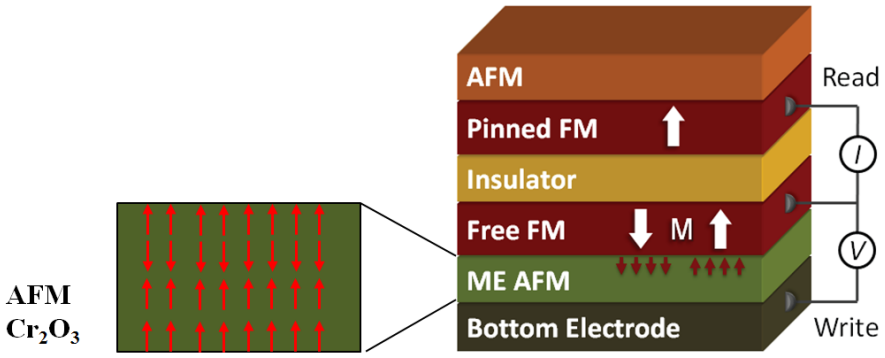


Figure 5.2 Schematics of magnetoelastic recording device.

**Table 5.1 Comparison of memory and storage technologies[19, 20].**

| | HDD | STT-MRAM | ME memory device |
|---|---|---|---|
| Energy per bit (pJ) | 1-10×109 | 0.1 | 0.01 |
| Read/Write time (ns) | 5-8×106 | 1-10 | 1-10 |

## 5.1 Magnetic Anisotropy

In ferromagnetic materials, the magnetic moment tends to align with certain directions. This phenomenon is known as magnetic anisotropy. The preferred axis (direction) is called easy axis, and the axis normal to the easy axis is called hard axis. In a soft magnetic material with uniaxial magnetic anisotropy (the material only has one easy axis), the shape of magnetic hysteresis loop depends on the direction of the external magnetic field. When sweeping the magnetic field along the easy axis, a

square hysteresis loop will be observed, as shown in Figure 5.3 (a). The coercivity field $h_c$ is the magnitude of the magnetic field as the magnetic moment equals to zero. For a magnetic single domain, the coercivity field relates to the magnetic anisotropy energy $K_u$ as $h_c=K_u/(2Ms)$. When applying the magnetic field along the hard axis as shown in Figure 5.3 (b), the magnetization is hard to be saturated by the field. The hysteresis curve goes across the origin of the coordinate. The effective magnetic anisotropy field $h_a$ is the field to deflect the magnetic moment from the easy to the hard axis.

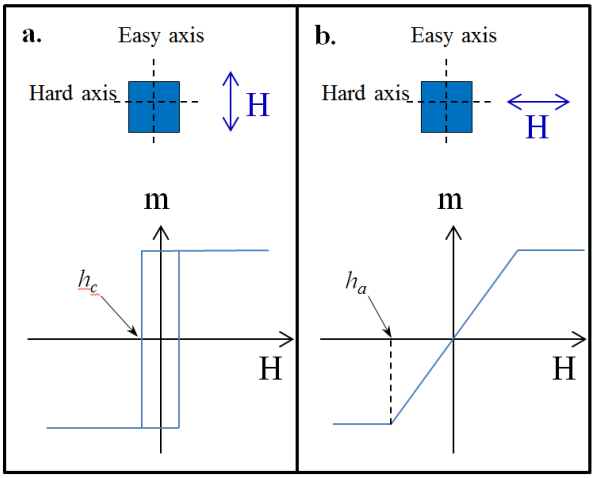


Figure 5.3 The schematics of hysteresis loops as sweeping magnetic field along (a) easy axis (b) hard axis

There are several origins of magnetic anisotropy: magnetocrystalline anisotropy, shape anisotropy, magnetoelastic anisotropy, and interface magnetic anisotropy. In a single-crystal magnetic material, magnetocrystalline anisotropy is due to the spin-orbit coupling. The magnetocrystalline anisotropy is small in transition metals Co, Fe and Ni, due to the quenching of the orbital moment [21]. The magnitude of magnetocrystalline anisotropy depends on the crystallinity of the materials. The

magnetic transition metal films deposited by sputtering are usually polycrystalline. Consequently, there are no well-defined easy axes. The shape anisotropy arises from the demagnetizing field that depends on the geometry of the magnet. The magnetization causes net magnetic charges at the edge of the magnet that generates the magnetic field in the direction opposite to the magnetization. In a magnetic thin film, the demagnetizing field is equal to $-4\pi M_s$ in the perpendicular direction to the film plane, and it equals to zero in the film plane. Therefore, without perpendicular anisotropy, the magnetization prefers to lie in the film plane. A perpendicular magnetic field larger than the saturation magnetization can rotate the magnetization to the normal direction. The magnetoelastic effect is the change in the magnetic anisotropy due to the strain [22].

Interface magnetic anisotropy usually causes the perpendicular magnetic anisotropy (PMA). In ultra-thin magnetic films, the interface significantly influences the magnetic properties. Due to the broken symmetry, the atoms at the interface have a different environment compared to those in the bulk. For a monolayer of Co [23], because of the broken of symmetry at the surface, the energy of the out-of-plane 3d orbitals $d_{xz}$, $d_{z^2}$ and $d_{yz}$ are lower than the energy of the in-plane orbitals $d_{xy}$ and $d_{x^2-y^2}$. As a result, the electron first fills the 3d bands with out-of-plane anisotropy. The perpendicular surface anisotropy is of the order of 1 erg/cm$^2$ [23].

The picture becomes more complicated with different kinds of interface atoms. Two scenarios have been demonstrated with enhanced surface anisotropy. The first one is heavy metals (HM), such as Pt and Pd, at the surface of ferromagnetic transition metal (FM) such as Co or Fe. The second example is oxygen atoms at the surface of Co or Fe. The presence of heavy atoms at the Co surface will give rise to a

strong hybridization of Co 3d orbitals with Pt 5d orbitals. The interface hybridization can be viewed as an effective field acting on the Co/Pt interfacial atoms and modifying their band structures. Owing to the strong spin-orbital interaction in Pt, the splitting of Co 3d out-of-plane and in-plane orbitals is increased, resulting in strong perpendicular anisotropy of the interfacial Co atoms. The effective field also acts on the interfacial Pt atoms, inducing a magnetic moment at the Pt interface parallel to the Co magnetic moment. The strong spin-orbital interaction in heavy metal is essential for the PMA in HM/FM systems.

Recently, PMA was observed in FM/oxides heterostructures such as Fe/MgO [24] and CoFeB/MgO [25]. This effect quickly captured tremendous attention, because Fe/MgO and CoFeB/MgO are the essential structures in MTJs. Different from HM/FM interface, the spin-orbital interaction is weak in oxides. The hybridization between Fe 3d and O 2p orbitals gives rise to a strong crystal field at the interface, which splits the Fe 3d out-of-plane and in-plane bands. The Fe-O bond here is critical to the PMA [26]. For example, the over/under-oxidation of the FM/oxide interface will reduce the interface anisotropy. Specifically, the stoichiometric MgO in Fe/MgO gives rise to the highest PMA. PMA in the under-oxidized Fe/MgO interface is greater than PMA in the over-oxidized interface.

To make MTJ with perpendicular magnetic anisotropy (p-MTJ), thin films with PMA are demanded. Three types of materials with PMA have been explored in this thesis.

## 5.2 Multilayer Thin Films with Perpendicular magnetic anisotropy

PMA can be developed in multilayers (MLs) formed by the alternative of ferromagnetic metal (FM), such as Co and Fe, and heavy metal (HM), such as Pt and

Pd. We investigated the PMA in Co/Pd ML's. The coercivity of the films can be tailored by changing the thickness of the individual Co and Pd players. A series of Co/Pd (Pt) MLs were deposited on (100) silicon substrates with 1000 nm wet thermal SiO2. All the metallic layers were deposited using dc sputtering, and the $SiO_2$ capping layer was deposited using radio-frequency (RF) sputtering. The base pressure is lower than $5 \times 10^{-7}$ Torr. The Ar atmosphere pressure during sputtering was 4.5 mTorr. The first set of samples has constant Co film thickness of 0.3 nm and various Pd film thicknesses ranging from 0.3 nm to 1.2nm. The second set of samples has constant Pd film thickness of 0.6 nm and different Co film thicknesses ranging from 0.3 nm to 0.9 nm. After the deposition of the MLs, the samples were transferred into a glove box with high purity Argon atmosphere. The level of oxygen and moisture is less than 5 ppm and 0.5 ppm, respectively. The samples were annealed at 250°C on top of a hot plate for 20 min and fast cooled down to room temperature by directly placed on a metal block. The PMA of the MLs was investigated by VSM. The magnetic hysteresis loops are shown in Figure 5.4. With the increase of Pd layer thickness from 0.3 nm to 1.2 nm, the coercivity is enhanced from 150 Oe to 700 Oe. The coercivity is reduced by increasing the Co layer thickness.

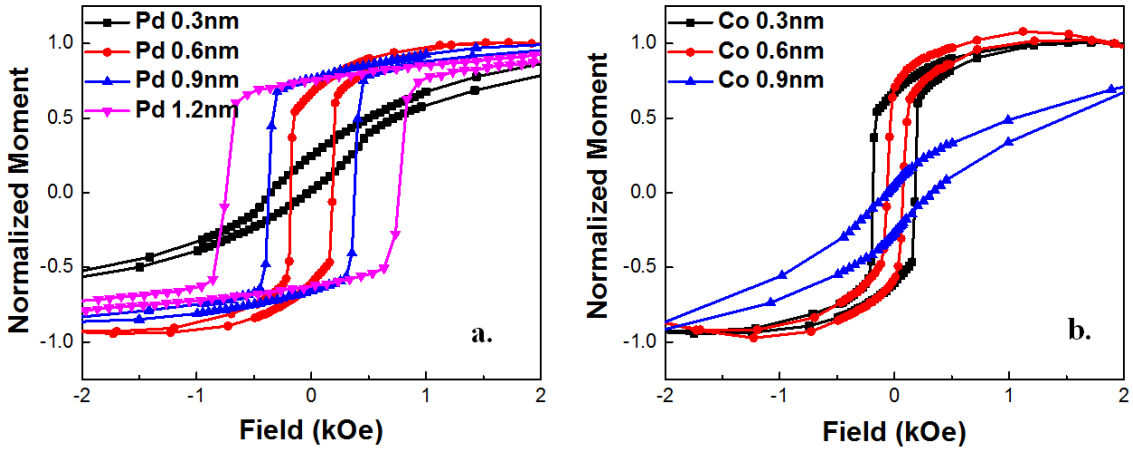


Figure 5.4 (a) The magnetic hysteresis loops of multilayer [Co (0.3 nm)/Pd(t nm)]$_{10}$ (b) The magnetic hysteresis loops of multilayer [Co (t nm)/Pd(0.6 nm)]$_{10}$

The crystalline (001) MgO is crucial for MTJs with high TMR. However, the Co/Pd MLs are not the solid underlayer to grow (001) MgO. The best choice of the underlayer is CoFeB that promotes the growth of MgO with (001) texture. Therefore, a $Co_{40}Fe_{40}B_{20}$ layer was inserted in between Co/Pd MLs and MgO layer. We fabricated Ta(7nm)/ Ru(20nm)/ Ta(7nm)/ [Co(0.3nm)/Pd(0.6nm)]$_{10}$/ Ta(0.4nm)/ CoFeB(1.1nm)/ MgO(3nm)/ CoFeB(1.1nm)/ Ta(0.4nm))/ [Co(0.3nm)/Pd(1.2nm)]$_{10}$/Au(100nm) structure. The films were annealed at 250°C on top of a hot plate for 20 min in a glove box and fast cooled down to room temperature. The bottom Co/Pd MLs contain thinner Pd layer than the top Co/Pd multilayers. So their coercivities are different. We observed two magnetic switching in the hysteresis loop as shown in Figure 5.5. Both of the parallel and antiparallel configurations exist in the field sweeping which is required for the tunneling magnetoresistance measurement. For example, when the external field is 1000 Oe, the top and bottom magnetizations are parallel. When the external field decreases to -500 Oe, the top, and bottom magnetizations are antiparallel.

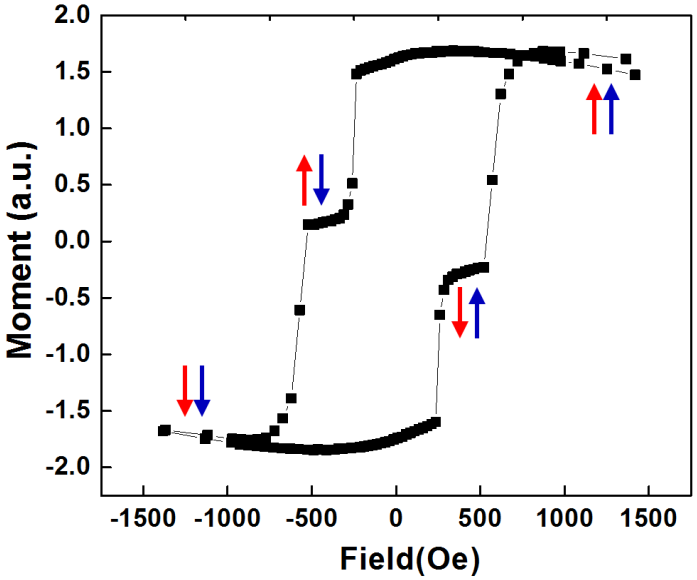


Figure 5.5 The magnetic hysteresis loop of a MTJ stack with structure of Ta(7nm)/ Ru(20nm)/ Ta(7nm)/ [Co(0.3nm)/Pd(0.6nm)]10/ Ta(0.4nm)/ CoFeB(1.1nm)/ MgO(3nm)/ CoFeB(1.1nm)/ Ta(0.4nm))/ [Co(0.3nm)/Pd(1.2nm)]10/Au(100nm). The blue and red arrows indicate the magnetization of the top and bottom magnetic layers, respectively.

The PMA of the multilayers was also investigated via anomalous Hall effect (AHE). The Hall effect is the generation of a voltage in the direction transverse to an electric current in a conductor due to the Lorentz force caused by a magnetic field. The ferromagnetic materials show much larger Hall effect than non-magnetic conductor, because of the broken time-reversal symmetry in a ferromagnetic phase due to the spin-orbital coupling. Besides the contribution of ordinary Hall effect, the Hall voltage of FM is mainly determined by the magnetization in the direction normal to the film surface. The stronger Hall effect discovered in ferromagnetic conductors is known as AHE. The Hall resistance is defined as $\rho_{xy} = \frac{V_{xy}}{I}$, where $I$ is the applied current and $V_{xy}$ is the transverse voltage. It has a general expression as

$$\rho_{xy} = R_0 H_z + R_s M_z \tag{5.1}$$

where $R_0$ is the ordinary Hall constant, $H_z$ is the external magnetic along the $z$-axis, $R_s$ is the AHE constant, and $M_z$ is the $z$ component of the magnetization.

A typical AHE measurement setup is sketched in Figure 5.6. The film was patterned into a 0.5 mm × 5 mm Hall bar through conventional photolithography followed by ion beam milling. A constant current is injected in the film plane along the $y$ direction, the Hall voltage is measured across the current in the $x$ direction by a nanovoltmeter (Keithley 2182A), and an external magnetic field generated by a pair of Helmholtz coil is applied perpendicular to the film plane. The PMA properties of a perpendicular FM film are studied by $V_{xy}$–$H$ hysteresis loop with sweeping the perpendicular magnetic field. Figure 5.6 (b) shows a typical Hall hysteresis loop. The 100% perpendicular remanence and sharp square hysteresis loop indicate the PMA in the Co/Pd ML's. The coercivity of the film is indicated by the value of the magnetic field where the Hall resistance equals to zero. The advantage of using AHE to characterize the PMA is the low noise and no background signal.

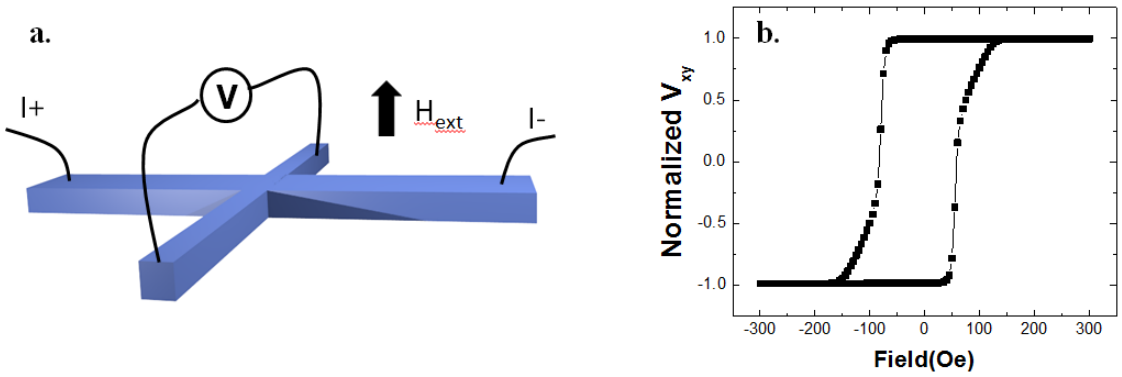


Figure 5.6 (a) The schematics of AHE measurement (b) Hall voltage as a function of magnetic field.

## 5.3 Exchange Coupling Between Co/ Pt MLs and Antiferromagnet IrMn

The perpendicular exchange coupling (bias) between ferromagnetic and antiferromagnetic layers is very crucial for developing nonvolatile magnetoelectric devices. Voltage controls the interface magnetization of antiferromagnet (AFM) Cr2O3. The switching of the interface magnetization reverses the magnetization of the ferromagnetic (FM) layer through the exchange coupling between FM and $Cr_2O_3$. The exchange bias is manifested in the shift in the hysteresis loop of FM layer along the magnetic field axis. An exchange-bias field $H_{EB}$ quantifies the shift of the magnetization hysteresis loop. Here, we investigated the dependence of exchange bias on the thickness of the spacer layer (Pt) between FM and AFM IrMn layer. We have investigated the exchange bias properties of Pt(0.5 nm)/[Co(0.4 nm)/Pt1.5 nm]$_2$/Co(0.4 nm)/**Pt(0.2~0.8 nm)**/IrMn(15 nm). IrMn is one of the typical AFM materials used in information-storage devices to pin the magnetization of the reference magnetic layer in a magnetic tunnel junction or to stabilize magnetization of nanomagnets against thermal excitations. The Pt spacer layer between Co and IrMn varies from 0.2 to 0.8 nm. Figure 5.7 (a) shows the hysteresis loop of samples with 0.2 nm, 0.4 nm, and 0.8 nm Pt spacer layer. We observed the change of coercivity and exchange bias. The coercivity is reduced as the increase in the Pt layer thickness. The exchange bias is calculated by

$$H_{EB} = \left(H_{c,-M} - H_{c,+M}\right)/2 \tag{5.2}$$

where $H_{c,-M}$ and $H_{c,+M}$ are the coercivity field at negative and positive field respectively.

As shown in Figure 5.7 (b), the exchange bias is inversely proportional to the spacer layer thickness. To switch the magnetization of an FM layer through the exchange coupling to an AFM, a spacer layer with a thin thickness is desirable.

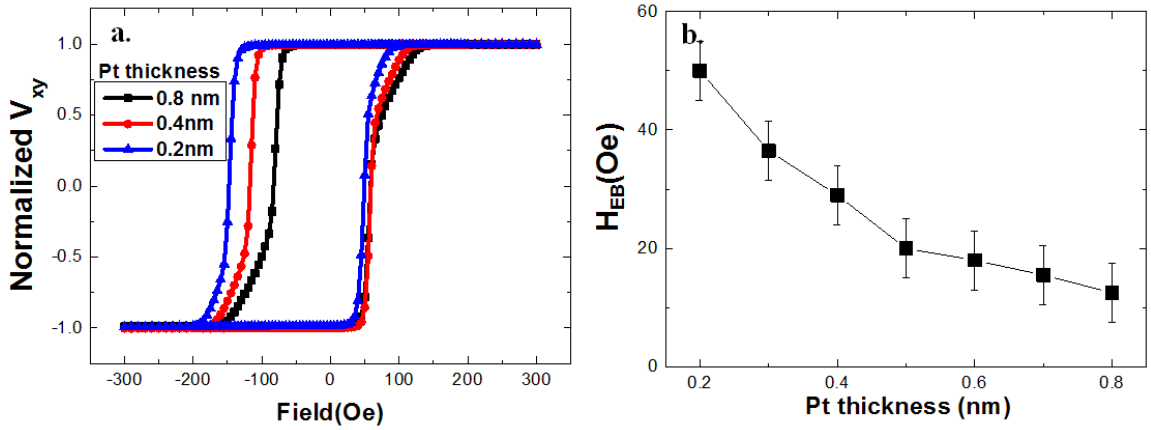


Figure 5.7 (a) the hysteresis loops of films with various Pt spacer thicknesses (b) the exchange bias field as a function of the spacer layer thickness.

## 5.4 Perpendicular Magnetic Anisotropy in Ta/CoFeB/MgO

Recently, perpendicular magnetic anisotropy was discovered in Ta/CoFeB/MgO, which is an essential structure in a magnetic tunnel junction [25]. The PMA in Ta/CoFeB/MgO originates from the hybridization of CoFeB 3d and O 2p orbitals. The thickness of each layer and annealing conditions play a significant role in fabricating thin films with PMA. After the film deposition, the PMA was developed by the rapid thermal annealing in a glove box. It was reported that the rapid thermal annealing is a promising thermal treatment process to fabricate perpendicular MTJs with TMR over 100% [27]. The annealing temperature we used was 340 °C and annealing time was 3 min. Then the sample was placed on a metal plate to cool rapidly down to room temperature. The thickness of Ta, CoFeB, and MgO affect PMA

significantly. Several films with different layer thicknesses were fabricated and patterned into Hall bar structure to investigate PMA in the films. We fabricated a layer of wedged shape with variable thickness and fixed the thicknesses of all other layers. Figure 5.8 shows the AHE loops of the samples. The structure of sample 1 from bottom to top is Ta(1-3 nm)/CoFeB(1.2 nm)/MgO(3 nm)/Ta(2 nm). The 2 nm Ta capping layer was used to protect the film during the photolithography process. The thickness of the bottom Ta varies from 1 nm to 3 nm. The thicknesses of the other layers are constant. We observed clear PMA signal in the samples with Ta thicker than 1 nm. Similarly, we studied the influence of CoFeB thickness on PMA in sample 2. The structure of sample 2 is Ta(2 nm)/CoFeB(0.8-1.5 nm)/MgO(3 nm)/Ta(2 nm). The samples with CoFeB thickness of 1 nm and 1.2 nm show perfect square hysteresis loop indicating good PMA. The PMA is weak in the samples with CoFeB thickness of 0.8 nm and 1.5 nm. The structure of sample 3 is Ta(2 nm)/CoFeB(1.2 nm)/MgO(1.1-3.5 nm)/Ta(2 nm). The samples with MgO layer thicker than 1.1 nm shows good PMA. To summarize the thickness study, we find out the proper thickness range of each layer to achieve good PMA: Ta thicker than 1 nm, CoFeB thickness in between 0.8 nm and 1.5 nm and MgO thicker than 1.1 nm. The determination of the proper thickness range is imperative to fabricate MTJs with PMA.

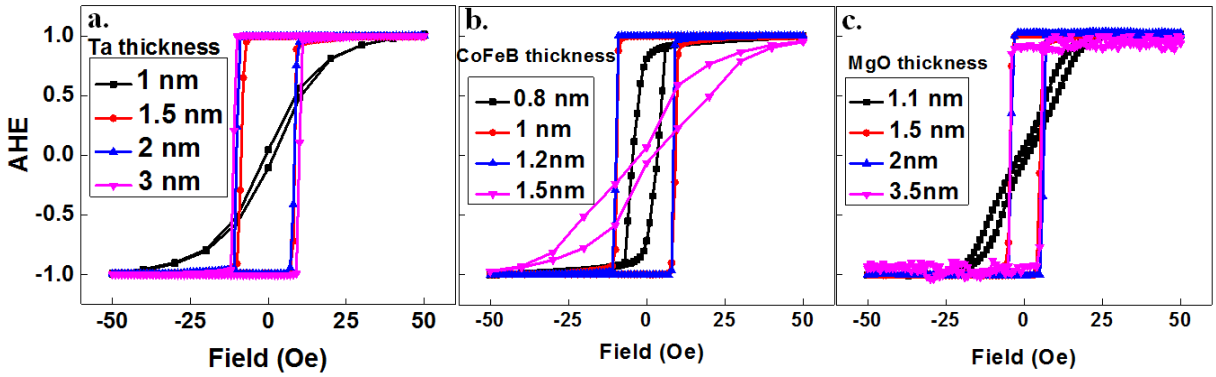


Figure 5.8 The AHE hysteresis loops of (a) Ta(t nm)/CoFeB (1.2 nm)/ MgO(3 nm)/Ta(2 nm). (b) Ta(2 nm)/CoFeB (t nm)/ MgO(3 nm)/Ta(2 nm) (c) Ta(2 nm)/CoFeB (1.2 nm)/ MgO(t nm)/Ta(2 nm)

## 5.5 Magnetic Tunnel Junctions with Amorphous Barrier

An MTJ is composed of an ultra-thin oxide insulating layer sandwiched between two ferromagnetic layers. We developed the methods to fabricate two types of barrier: amorphous $AlO_x$ barrier and crystalline MgO barrier. Although the TMR ratio of the MTJs with amorphous $AlO_x$ barrier is low (<60%), $AlO_x$-based MTJs are easier to fabricate and is thus a good choice to begin with. The high vacuum chamber was first pumped to a base pressure of $1\times10^{-7}$ Torr. All the metal layers are deposited under 4.5 mTorr argon atmosphere by dc magnetron sputtering except the IrMn layer which is deposited by RF sputtering. The $AlO_x$ barrier can be fabricated by oxidizing an ultra-thin aluminum layer in $O_2$ plasma or by RF sputtering of an $Al_2O_3$ target. The former method is superior to make high-quality AlOx barrier without pin holes. After 2 nm aluminum film was deposited, the metal film was oxidized through two steps of plasma oxidation. The $O_2$ pressure is 60 mTorr, and RF power is 120W. The first step is to expose the Al layer in $O_2$ plasma for several times with exposure duration less than 1s.Then the film was kept in $O_2$ plasma for 3 min. Figure 5.9 shows the high-resolution TEM picture of the MTJ film with NiFe/$AlO_x$/NiFe. The $Al_2O_3$ barrier is

clearly amorphous, and the NiFe electrodes show very high quality (111) crystalline orientation. No pin hole in the $Al_2O_3$ was observed.

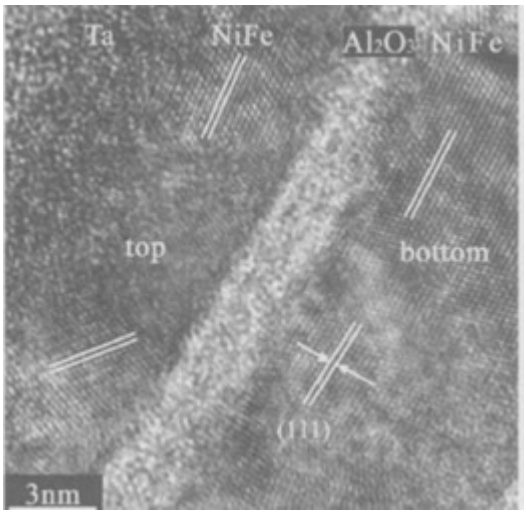


Figure 5.9 The TEM picture of an MTJ with $AlO_x$ barrier

The typical TMR curves of $[Co/Pd]_n$/ $Al_2O_3$/$[Co/Pd]_n$ MTJs are shown in Figure 5.10. Figure 5.10 (a) presents the TMR loops in a small field range that only one of the two magnetic electrodes switches its direction, resulting in a single step in the hysteresis loop. The TMR ratio decreases with the increase of the bias voltage, a common feature observed in all types of MTJs [28]. By increasing the field range to be $\pm 350$ Oe, the TMR curve shows four steps in Figure 5.10 (a). The low TMR state indicates parallel configuration and high TMR state indicate anti-parallel configuration. The TMR ratio of MTJs with $AlO_x$ barrier is typically less than 10 %, that is not high enough for the applications requires high sensitivity.

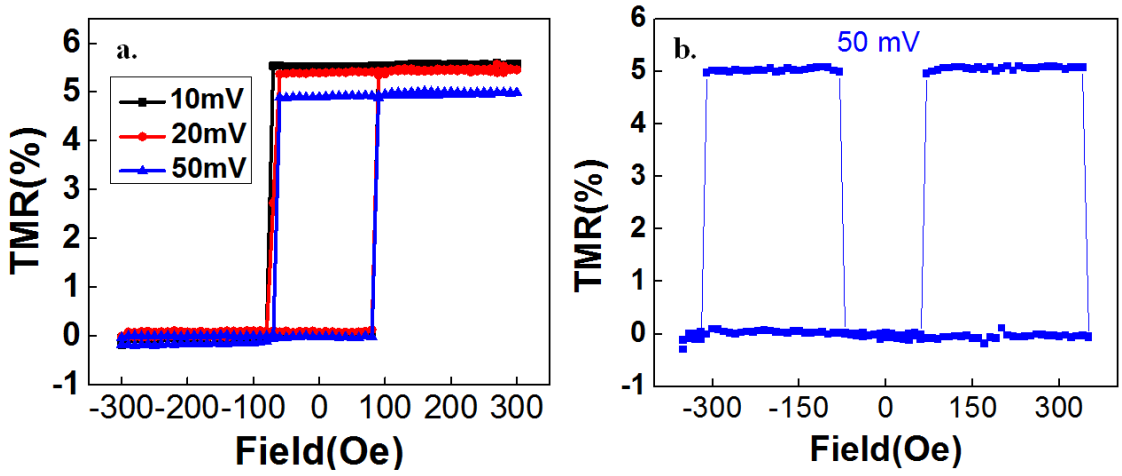


Figure 5.10 (a) TMR curves of an $AlO_x$ based MTJ at a various bias voltage. (b) A complete TMR curve at 50 mV bias voltage

## 5.6 Magnetic Tunnel Junctions with Crystalline MgO Barrier

The TMR ratio of MTJs with crystalline MgO barrier is very high due to the coherent spin tunneling in single-crystal FM/MgO/FM structure. We developed and improved the process of fabricating the MTJs with PMA.

### 5.6.1 Improve the Tunneling Magnetoresistance in MTJs with MgO Barrier

The origin of the enormously high TMR in MTJs with crystalline MgO tunnel barrier is the coherent tunneling of electrons with $\Delta_1$ symmetry at the Fermi level in ultrathin MgO with (001) texture [29] (also see Section 2.5.3). The textured growth of MgO (001) is very sensitivity to the base pressure of the vacuum chamber, especially the residual moisture. $H_2O$ is found to be the major part of the residual gas in the sputtering chamber. $H_2O$ molecules are often trapped on the inner wall of a vacuum chamber due to van der Waals force. To remove the $H_2O$ molecules, we bake the chamber up to 100 ºC for 48 hours using four resistor heating belts, while pumping the chamber with a cryopump. Then the sputtering chamber is cooled down to room

temperature. An ion gauge detects the base pressure, and the partial pressure of gasses is measured by a residual gas analyzer (RGA). At this time, the base pressure is about $6\times10^{-8}$ Torr and the partial pressure of $H_2O$ ($P_{H_2O}$) is $2\times10^{-8}$ Torr. The partial pressure of other residual gasses, such as $H_2$, $O_2$, $N_2$, and $CO_2$, are less than $5\times10^{-9}$ Torr. To further reduce the $H_2O$ partial pressure, a Ta target is sputtered by dc sputtering at 40 W power. Usually, the sputtering time is 20 min to 40 min. After the Ta sputtering, the $H_2O$ partial pressure can go down to $3\times10^{-9}$ Torr and the total base pressure is less than $3\times10^{-8}$ Torr. We investigated the influence of $H_2O$ partial pressure on the crystalline structure of MgO. Two samples with the same structure as Ta (10 nm)/ CoFeB (10 nm)/ MgO (10 nm)/ CoFeB (10 nm)/Ta (10 nm) were fabricated. The $H_2O$ partial pressures during the sputtering were $2\times10^{-8}$ Torr and $3\times10^{-9}$ Torr respectively. After deposition, the samples were annealed at 380 ºC for 3 min in the glove box followed by fast cooling. The XRD patterns of the two samples are plotted in Figure 5.11. The sample grown at $P_{H_2O}$ as $3\times10^{-9}$ Torr shows a stronger MgO (002) peak, indicating a better MgO (001) crystalline texture. The MgO growth benefits from low $H_2O$ partial pressure during the deposition.

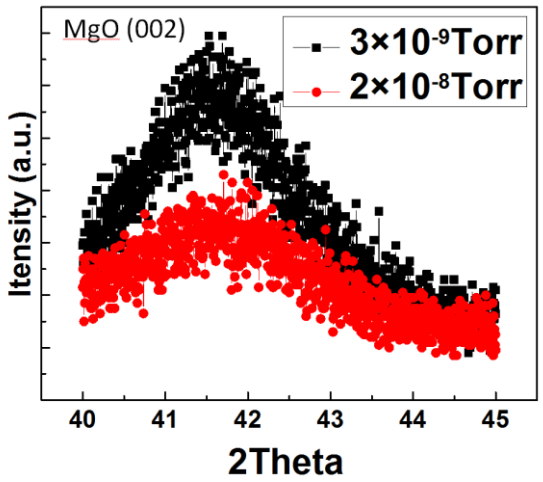


Figure 5.11 The XRD spectrum of Ta/CoFeB/MgO/CoFeB/Ta films. The $H_2O$ partial pressure at the sputtering is $3\times10^{-9}$ Torr and $2\times10^{-8}$ Torr respectively for the two samples.

To investigate the effect of $P_{H_2O}$ on TMR, we grow two identical MTJs with in-plane magnetic anisotropy at different $P_{H_2O}$. The film stack is Si/$SiO_2$/Ta (8 nm)/ Ru (20 nm) / Ta (8 nm) / CoFe (4 nm)/ IrMn (15 nm)/ CoFe (4 nm)/ Ru (0.85 nm) / CoFeB (3 nm)/ MgO (0.8-4 nm)/ CoFeB (3 nm)/ Ta (8 nm)/ Au (100 nm). Sample A was deposited in $H_2O$ partial pressure of $2\times10^{-8}$ Torr, and sample B was deposited in $H_2O$ partial pressure of $3\times10^{-9}$ Torr. Both samples were annealing at 380 ºC for 3 min in glove box through a rapid thermal annealing process. The films were then patterned into pillar structure by photolithography and ion beam milling to perform TMR test. Figure 5.12 shows the TMR curves for sample A and sample B. The TMR ratio of sample A is less than 10%, and the TMR ratio of sample B is about 20%. The TMR is improved by reducing the $H_2O$ partial pressure during sputtering.

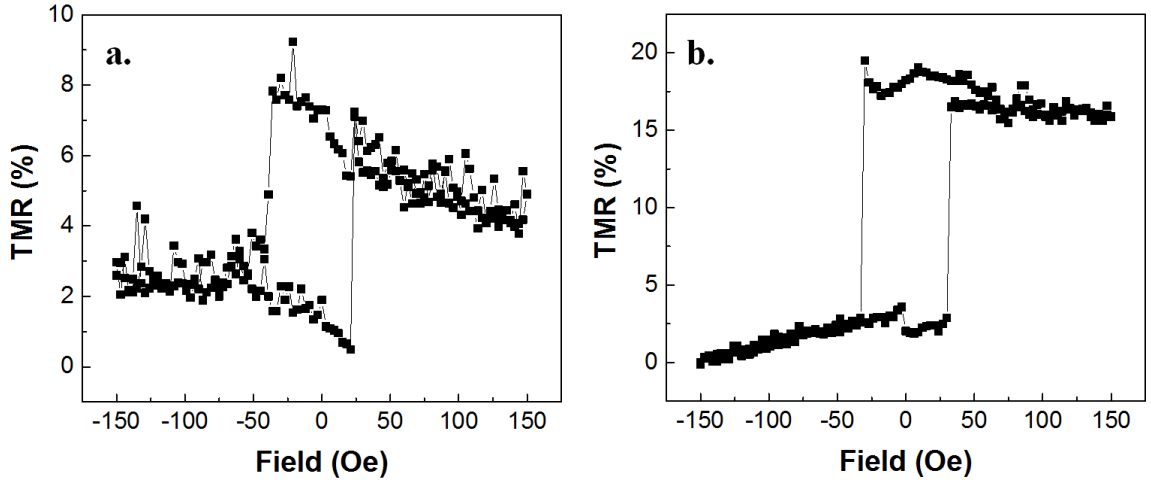

Figure 5.12 The TMR curves of the in-plane MTJs grown with MgO sputtering power as 4 W/cm$^2$ and $H_2O$ partial pressure of (a) $2\times10^{-8}$ Torr (b) $3\times10^{-9}$ Torr

We then improved the TMR by reducing the sputtering rate of MgO. The sputtering rate of MgO was decreased from 0.25nm/min (sample B) to 0.1 nm/min (sample C), by reducing the RF sputtering power from 4 W/cm$^2$ to 2.5W/cm$^2$. The TMR curve of sample C is shown in Figure 5.13. A TMR ration of 120% was achieved in this junction.

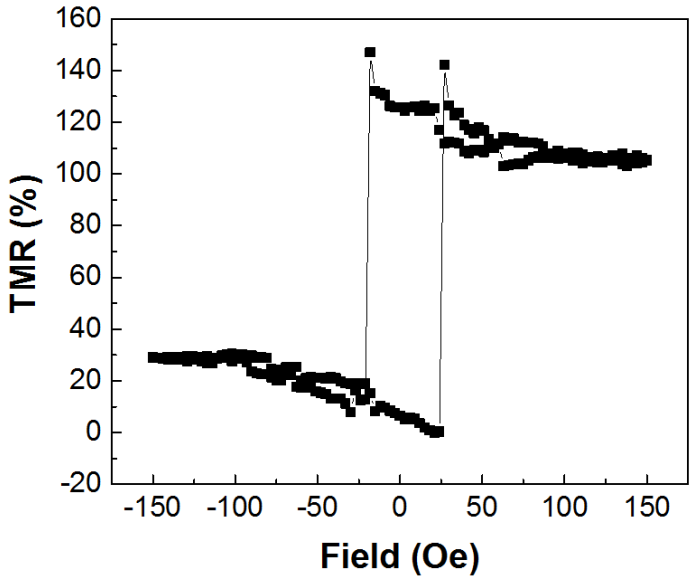


Figure 5.13 The TMR curve of an in-plane MTJ fabricated at $H_2O$ partial pressure $3\times10^{-9}$ Torr and MgO sputtering power as 2.5W/cm$^2$

We also performed current-in-plane-tunneling (CIPT) test on sample B and sample C to confirm the result. Since the thickness of MgO barrier is in the range from 0.8 to 4 nm, we can observe increased junction resistance along the wedge direction. The TMR ratios at different resistances are listed in Table 5.2. For both CIPT and pillar measurement, the TMR ratio of sample C is higher than that of sample B. However, the CIPT measurement shows a decrease of TMR with the increase of resistance, which is not consistent with the pillar measurement. The larger TMR ratio found in the MTJs with lower MgO sputtering rate may arise from the smoother tunneling barrier. Further investigation is needed to verify this argument. Finally, by reducing the $H_2O$ partial pressure and MgO sputtering rate in making sample C, the highest TMR ratio of about 120% has been achieved that is promising for magnetoelectric devices.

**Table 5.2 Summary of TMR ratio and resistance of sample B (MgO sputtering power as 4 W/cm$^2$ and $H_2O$ partial pressure as $3\times10^{-9}$ Torr) and sample C (MgO sputtering power as 2.5 W/cm$^2$ and $H_2O$ partial pressure as $3\times10^{-9}$ Torr) measured by CIPT and pillar methods.**

| Sample B(CIPT) | | Sample C(CIPT) | | Sample C(pillar) | |
|---|---|---|---|---|---|
| TMR(%) | RA(kΩ) | TMR(%) | RA(kΩ) | TMR(%) | RA(kΩ) |
| 25 | 60 | 111 | 2.4 | 123 | 2.4 |
| 3 | 147 | 56 | 12.7 | 130 | 12.7 |
| 0.4 | 155 | 11.4 | 49 | 125 | 49 |
| 0.4 | 181 | 1.9 | 113 | 109 | 113 |

### 5.6.2 MTJs with MgO Barrier and PMA

The structure of the first perpendicular MTJ is Si/$SiO_2$/Ta (8 nm)/ Ru (20 nm) / Ta (8 nm)/ CoFeB (1.1 nm)/ MgO (2 nm)/ CoFeB (1-1.2 nm)/ Ta (8 nm)/ Au (100 nm). After the deposition of the film stacks, the films were patterned into circular shape MTJ pillars with a diameter ranging from 10 μm to 50 μm and then measured by two-probe measurement with the external field in the direction perpendicular to the film plane. The coercivity of the CoFeB electrodes depends on the layer thickness and their neighboring layers. To observe TMR, the two CoFeB electrodes should have different switching fields (coercivity). The top CoFeB electrode was fabricated to be a wedged layer with a thickness ranging from 1 nm to 1.2 nm. Figure 5.14 (a) shows the coercivity of the top CoFeB electrode as a function of its thickness. The typical TMR curves of the junction are shown in Figure 5.14 (b) and (c). Initially, the fabrication is not optimized. The TMR ratio is as low as 1.5%. After reducing the $H_2O$ partial pressure and MgO deposition rate, the highest TMR ratio reached is up to 60%. In this structure, the electric field at MgO/CoFeB interface would significantly affect the magnetic anisotropy of CoFeB. This voltage controlled magnetic anisotropy (VCMA) has been utilized to switch the magnetization [27] and excite spin dynamics [30].

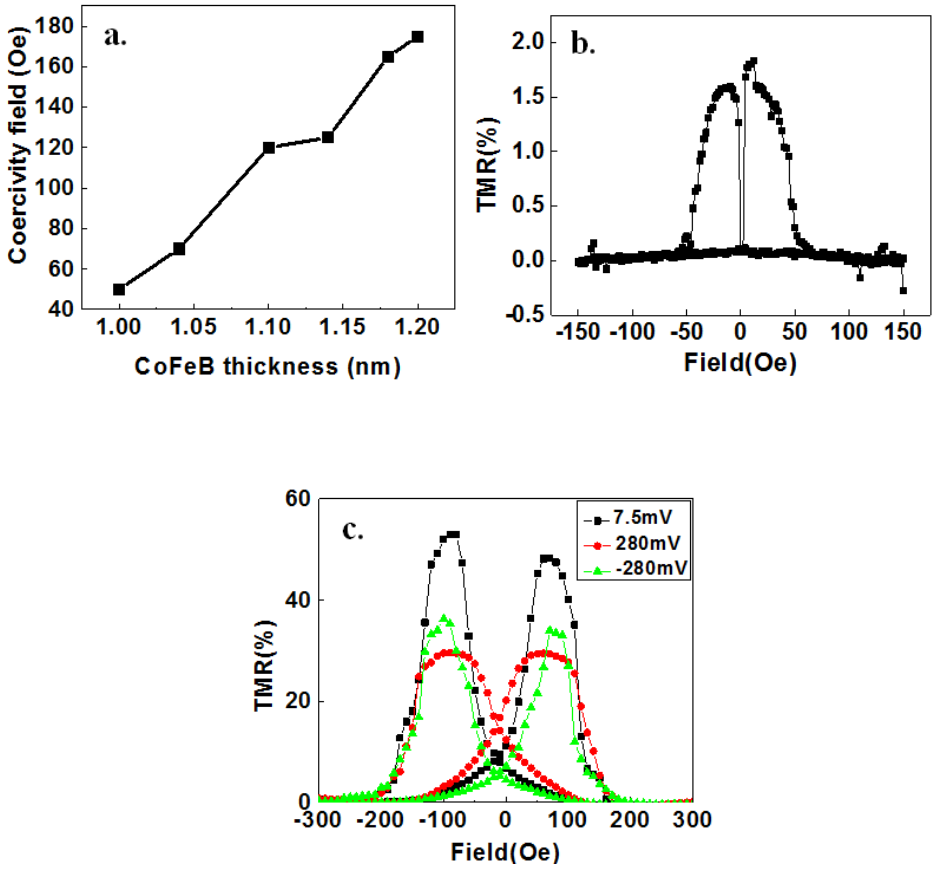


Figure 5.14 (a) the coercivity of top CoFeB layer as a function of the layer thickness (b) the TMR curve of the p-MTJs fabricated under bad conditions (c) the TMR curve of the p-MTJs fabricated under low $H_2O$ partial pressure and low MgO sputtering rate.

To investigate VCMA effect in our perpendicular junction, we applied a large positive and negative bias voltage on the junction pillar. As shown in Figure 5.14(c), the switching field changes a little bit between 280 mV and -280 mV bias. However, the switching of the two electrodes is not sharp enough to identify the coercivity field. The switching property was improved by reducing the annealing temperature from 380 ºC to 340 ºC. The improved TMR curve is shown in Figure 5.15. We also increased the bias voltage to 1 V and -1 V to enhance further the VCMA effect. By comparing the TMR curve along CoFeB wedge, we identified the high coercivity field corresponding to the top CoFeB electrode. We observed the shift of the

coercivity field due to the bias voltage. The coercivity of the top CoFeB electrode shows significant changes from 60 Oe to 105 Oe in the electric field range from -500 to 500 mV/nm.

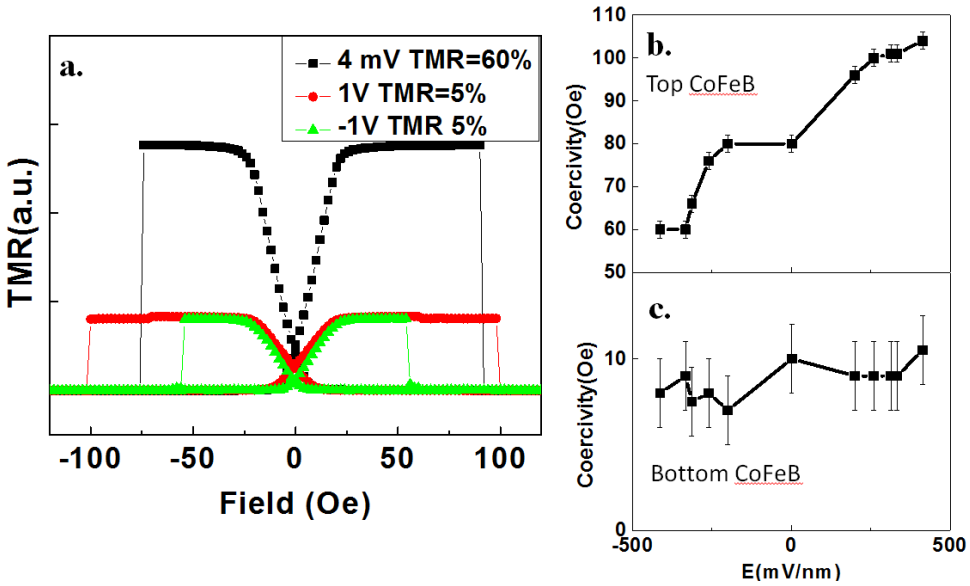


Figure 5.15 (a) the TMR curves of the p-MTJ annealed at 340 ºC (b) the coercivity of top CoFeB layer at different bias fields (c) the coercivity of bottom CoFeB layer at different bias fields

The perpendicular junctions with fixed layer are also fabricated. The structure is schematically represented in Figure 5.16. The bottom CoFeB electrode is the fixed layer with synthetic antiferromagnetic pinned layers. Its magnetization is fixed in the film plane. The top CoFeB layer has its magnetization perpendicular to the film plane due to PMA. After deposition, the films were patterned into circular shape MTJ pillars with a diameter ranging from 10 μm to 50 μm and then measured by two-probe measurement with external field sweeping in the film plane. The TMR of the junction is plotted in Figure 5.16. The in-plane magnetic field is not enough to drive the magnetization of the top CoFeB into the film plane to achieve parallel and

antiparallel configurations. The magnetization of the top CoFeB has only tilted a small angle from the normal direction. We calculate the TMR ratio to be 80% by estimating the effective magnetic anisotropy field as 2000 Oe. The device is suitable for the applications of spin wave excitation and detection.

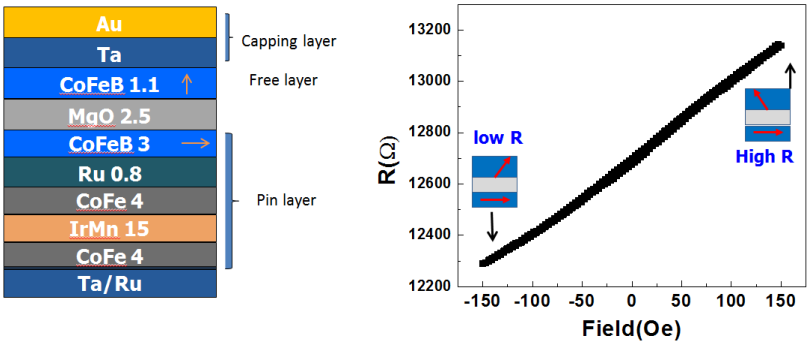


Figure 5.16 p-MTJs with an in-plane fixed layer.

## REFERENCES


[1] J. Yang and F.-B. Sun, "A comprehensive review of hard-disk drive reliability," in *Reliability and Maintainability Symposium, 1999. Proceedings. Annual*, 1999, pp. 403-409.

[2] "http://www.seagate.com/www-content/investors/_shared/docs/tech-talk-mark-re-20150825.pdf"

[3] E. Abarra, A. Inomata, H. Sato, I. Okamoto, and Y. Mizoshita, "Longitudinal magnetic recording media with thermal stabilization layers," *Applied Physics Letters,* vol. 77, pp. 2581-2583, 2000.

[4] G. Bertero, S. Malhotra, B. Bian, J. Tsoi, M. Avenell, D. Wachenschwanz*, et al.*, "Longitudinal magnetic media designs for 60-200-Gb/in 2 recording," *Magnetics, IEEE Transactions on,* vol. 39, pp. 651-656, 2003.

[5] S. Khizroev and D. Litvinov, *Perpendicular magnetic recording*: Springer Science & Business Media, 2006.

[6] R. Victora and X. Shen, "Composite media for perpendicular magnetic recording," *Magnetics, IEEE Transactions on,* vol. 41, pp. 537-542, 2005.

[7] P. Carcia, A. Meinhaldt, and A. Suna, "Perpendicular magnetic anisotropy in Pd/Co thin film layered structures," *Applied Physics Letters,* vol. 47, pp. 178-180, 1985.

[8] R. Victora and X. Shen, "Exchange coupled composite media for perpendicular magnetic recording," *Magnetics, IEEE Transactions on,* vol. 41, pp. 2828-2833, 2005.

[9] Y. Huai, "Spin-transfer torque MRAM (STT-MRAM): Challenges and prospects," *AAPPS Bulletin,* vol. 18, pp. 33-40, 2008.

[10] Z. Diao, Z. Li, S. Wang, Y. Ding, A. Panchula, E. Chen*, et al.*, "Spin-transfer torque switching in magnetic tunnel junctions and spin-transfer torque random access memory," *Journal of Physics: Condensed Matter,* vol. 19, p. 165209, 2007.

[11] E. Chen, D. Apalkov, Z. Diao, A. Driskill-Smith, D. Druist, D. Lottis*, et al.*, "Advances and future prospects of spin-transfer torque random access memory," *Magnetics, IEEE Transactions on,* vol. 46, pp. 1873-1878, 2010.

[12] C. Papusoi, B. Delaët, B. Rodmacq, D. Houssameddine, J.-P. Michel, U. Ebels*, et al.*, "100 ps precessional spin-transfer switching of a planar magnetic random access memory cell with perpendicular spin polarizer," *Applied Physics Letters,* vol. 95, p. 2506, 2009.

[13] M. Hosomi, H. Yamagishi, T. Yamamoto, K. Bessho, Y. Higo, K. Yamane*, et al.*, "A novel nonvolatile memory with spin torque transfer magnetization switching: Spin-RAM," in *Electron Devices Meeting, 2005. IEDM Technical Digest. IEEE International*, 2005, pp. 459-462.

[14] J. Hirsch, "Spin hall effect," *Physical Review Letters,* vol. 83, p. 1834, 1999.

[15] S. O. Valenzuela and M. Tinkham, "Direct electronic measurement of the spin Hall effect," *Nature,* vol. 442, pp. 176-179, 2006.

[16] L. Liu, C.-F. Pai, Y. Li, H. Tseng, D. Ralph, and R. Buhrman, "Spin-torque switching with the giant spin Hall effect of tantalum," *Science,* vol. 336, pp. 555-558, 2012.

[17] K. Dudko, V. Eremenko, and L. Semenenko, "Magnetostriction of Antiferromagnetic Cr2O3 in Strong Magnetic Fields," *physica status solidi (b),* vol. 43, pp. 471-477, 1971.

[18] X. He, Y. Wang, N. Wu, A. N. Caruso, E. Vescovo, K. D. Belashchenko*, et al.*, "Robust isothermal electric control of exchange bias at room temperature," *Nat Mater,* vol. 9, pp. 579-585, 07//print 2010.

[19] K. L. Wang, J. G. Alzate, and P. K. Amiri, "Low-power non-volatile spintronic memory: STT-RAM and beyond," *Journal of Physics D: Applied Physics,* vol. 46, p. 074003, 2013.

[20] J. J. Yang, D. B. Strukov, and D. R. Stewart, "Memristive devices for computing," *Nature nanotechnology,* vol. 8, pp. 13-24, 2013.

[21] P. W. Anderson, "Localized magnetic states in metals," *Physical Review,* vol. 124, p. 41, 1961.

[22] T. Moran and B. Lüthi, "Elastic and magnetoelastic effects in magnetite," *Physical Review,* vol. 187, p. 710, 1969.

[23] B. Carvello, C. Ducruet, B. Rodmacq, S. Auffret, E. Gautier, G. Gaudin*, et al.*, "Sizable room-temperature magnetoresistance in cobalt based magnetic tunnel junctions with out-of-plane anisotropy," *Applied Physics Letters,* vol. 92, p. 102508, 2008.

[24] A. Hallal, H. X. Yang, B. Dieny, and M. Chshiev, "Anatomy of perpendicular magnetic anisotropy in Fe/MgO magnetic tunnel junctions: First-principles insight," *Physical Review B,* vol. 88, p. 184423, 11/21/ 2013.

[25] S. Ikeda, K. Miura, H. Yamamoto, K. Mizunuma, H. D. Gan, M. Endo*, et al.*, "A perpendicular-anisotropy CoFeB–MgO magnetic tunnel junction," *Nat Mater,* vol. 9, pp. 721-724, 09//print 2010.

[26] H. X. Yang, M. Chshiev, B. Dieny, J. H. Lee, A. Manchon, and K. H. Shin, "First-principles investigation of the very large perpendicular magnetic anisotropy at Fe|MgO and Co|MgO interfaces," *Physical Review B,* vol. 84, p. 054401, 08/01/ 2011.

[27] W.-G. Wang, M. Li, S. Hageman, and C. L. Chien, "Electric-field-assisted switching in magnetic tunnel junctions," *Nat Mater,* vol. 11, pp. 64-68, 01//print 2012.

[28] A. Kalitsov, P.-J. Zermatten, F. Bonell, G. Gaudin, S. Andrieu, C. Tiusan*, et al.*, "Bias dependence of tunneling magnetoresistance in magnetic tunnel junctions with asymmetric barriers," *Journal of Physics: Condensed Matter,* vol. 25, p. 496005, 2013.

[29] E. Y. Tsymbal, O. N. Mryasov, and P. R. LeClair, "Spin-dependent tunnelling in magnetic tunnel junctions," *Journal of Physics: Condensed Matter,* vol. 15, p. R109, 2003.

[30] J. Zhu, J. A. Katine, G. E. Rowlands, Y.-J. Chen, Z. Duan, J. G. Alzate*, et al.*, "Voltage-Induced Ferromagnetic Resonance in Magnetic Tunnel Junctions," *Physical Review Letters,* vol. 108, p. 197203, 05/09/ 2012.

# Chapter 6

# CHARACTERIZATION OF SPIN-ORBITAL TORQUES AND MANIPULATION OF MAGNETIZATION IN MAGNETIC HETEROSTRUCTURES

## 6.1 Introduction

The request for nonvolatile low-power magnetic memories and logic devices has attracted intensive attention from both academy and industry on the research of the electrical control of magnetism. The magnetic manipulation based on spin orbital torques (SOTs) is one of the most promising techniques due to its high efficiency and simple structure. Two mechanisms have been proposed to generate pure spin currents or spin accumulation at NM/FM interface: spin Hall effect (SHE) [1, 2] and Rashba spin-orbit interaction [3]. In a magnetic bilayer illustrated in Figure 6.1 (a), an in-plane charge current in the non-magnetic (NM) layer generates a transverse pure spin current due to the spin Hall effect. The spin current will flow into the adjacent FM layer and alter the magnetization of the FM layer. The direction of the SOTs depends on the polarity of the charge current flow. Similar to the anomalous Hall effect, the spin Hall effect is caused by the screw scattering, side jump and intrinsic spin-orbital coupling in the NM layer.

The screw scattering was first proposed and observed by Mott in 1929 [4] and 1932 [5]. The electrons move with a high velocity and interact with the electric field of atomic nuclei. Because of the relativistic spin-orbital coupling, an asymmetric scattering of polarized electrons occurs. The electron scattering by a nuclear that

carries negative charge is schematically depicted in Figure 6.1 (b). In the rest frame of the electron, the electron spin feels a relativistic magnetic field $\vec{B} \propto \vec{v} \times \vec{E}$ perpendicular to the plane of the electron trajectory. The magnetic field has opposite signs for the electrons moving to the right and the left of the charged nuclear. The induced Zeeman energy of the electrons is defined as

$$E = -\vec{\mu}_B \cdot \vec{B} \tag{6.1}$$

where $\mu_B$ is the Bohr Magneton. The spin-up and spin-down electrons will be deflected into the opposite directions to minimize the Zeeman energy.

The side jump is due to the presence of impurities or defects in the material. The Hamiltonian of spin-orbital interaction is expressed as [6]

$$H_{so} = -\frac{\lambda_c^2}{4\hbar}\left[\mathbf{p} \times \nabla V(\mathbf{r})\right] \cdot \boldsymbol{\sigma} \tag{6.2}$$

where $\lambda_c$ is the constant of spin-orbital coupling, $\mathbf{p}$ is the momentum of the conducting electron, $V(\mathbf{r})$ is the potential of the impurity atoms acting on the electron, and $\boldsymbol{\sigma}$ is the vector of the Pauli matrices. Due to the spin-orbital coupling, the position operator of the electron is redefined as $\mathbf{r}' = \mathbf{r} + \frac{\lambda^2}{4\hbar}\mathbf{p} \times \boldsymbol{\sigma}$. One can derive the velocity as [6]

$$\mathbf{v} = \frac{i}{\hbar}\left[H, r'\right] = \frac{\hbar \mathbf{k}}{m^*} + \frac{2\lambda_c^2}{\hbar}\nabla V(\mathbf{r}) \times \boldsymbol{\sigma} \tag{6.3}$$

where $\mathbf{k}$ is the wavevector and $m^*$ is the effective mass of conducting electron. The second term on the right-hand side of Eq. (6.3) is corresponding to an anomalous velocity arising from the spin-orbital coupling. The electron is described by a wave packet. In the electron-impurity collision process as illustrated in Figure 6.1 (c), the average momentum of the wave packet has a change as $\hbar\nabla\mathbf{k}$ and the derivative of potential $\nabla V(\mathbf{r}) = -\hbar\dot{\mathbf{k}}$ is dominating the velocity of the electron as Eq. (6.3).

Therefore, one can calculate the displacement of the electron after the electron scattering off the impurity as [6]

$$\Delta r' = \int v(t)dt = -2\lambda_c^2 \Delta k \times \sigma \tag{6.4}$$

The displacement $\Delta r'$ is known as the "side-jump".

The intrinsic spin-orbital interaction is found to be significant in certain materials, such as heavy metals. A transverse spin-dependent velocity can be generated by the relativistic spin-orbital field in a crystal without any screw scattering. The relativistic spin-orbital field is caused by the band structure of an NM. The SHE was initially observed in semiconductors [1, 7, 8] and quickly detected in heavy metal [9-11].

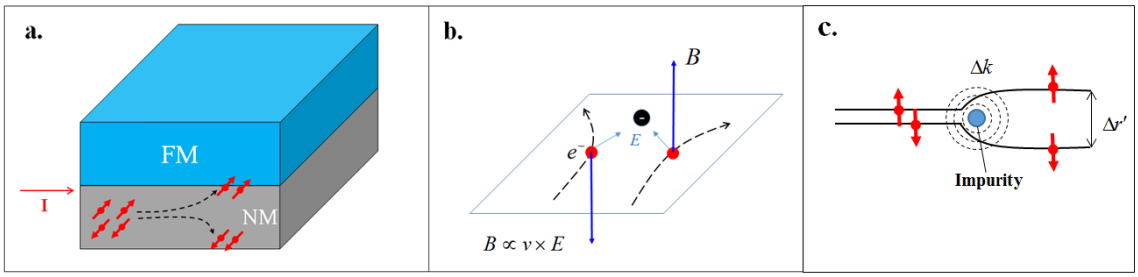


Figure 6.1 The schematics of (a) spin Hall effect and induced spin accumulation at the interface (b) screw scattering effect (c) side jump effect.

The SHE is not the only mechanism that can inject spins into FM in NM-FM bilayers. The other mechanism is the Rashba effect, which originates from the broken structure inversion symmetry. As illustrated in Figure 6.2 (a), a Rashba magnetic field is given by $\vec{B}_{Rashba} \propto \vec{v} \times \vec{E}$ [12], where $\vec{E}$ is the electric field normal to the film plane generated by the broken structure inversion symmetry. Therefore, the equilibrium spin texture in *k* space with zero current is chiral as illustrated in Figure 6.2 (b). The current driven by an electrical field applied along the *x*-axis induces a shift

in the $k$ space as $\delta k$, as shown in Figure 6.2 (c). By integrating throughout the $k$ space, a net spin along the $y$ direction at the FM/NM interface is produced.

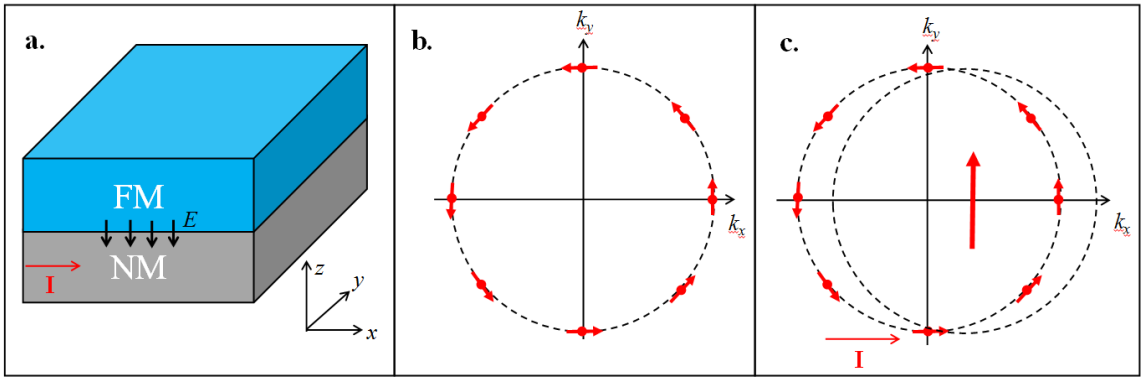


Figure 6.2 (a) the schematics of Rashba configuration. (b) Rashba spin texture in equilibrium with zero current. (c) non-equilibrium redistribution of spin texture in an applied charge current.

Even though SHE and Rashba effect are usually entangled in experiments; one can distinguish them from their dependence on the angle between the current and magnetization because Rashba effect has more significant angle dependence than SHE [13]. The quantitative characterization of the SOTs is highly demanded both fundamental scientific understanding and practical applications. In this chapter, an optical method based on magneto-optic Kerr effect (MOKE) with normally incident light is discussed. By measuring the angle dependence of SOTs, we found the Rashba effect dominates the SOTs in Ta/CoFeB/MgO.

## 6.2 MOKE Measurement of the Effective Fields due to Spin-Orbital Torque

The incident light interacts with the magnetic surface, leading to a change of polarization in the reflected light. The polarization rotation is arising from a magnetization dependent permittivity tensor, which can be written as a Taylor series relates to the magnetization vector $\boldsymbol{m}$ [14]

$$\varepsilon_{ij}(\vec{m}) = \varepsilon_{ij}(0) + \sum_{k=x,y,z} \varepsilon_{ijk} m_k + \sum_{k,l=x,y,z} \varepsilon_{ijkl} m_k m_l + ... \tag{6.5}$$

where the first term on the right side of Eq. (6.5) is the magnetic-independent permittivity, the second term gives rise to the first-order MOKE response including common polar, longitudinal and transverse MOKE signals, and the third term corresponds to the second-order MOKE response, as referred to quadratic MOKE.

In the configuration of normal incident light with linear polarization, the incident light is reflected back from a magnetic surface. The rotation of the polarization angle due to the magnetization of a magnetic thin film can be expressed as

$$\Psi \propto \alpha_{polar} m_z + \beta_{quadratic} m_x m_y \tag{6.6}$$

where $\alpha_{polar}$ and $\beta_{quadratic}$ are the coefficient for the polar and quadratic MOKE signals, respectively.

The polar and quadratic MOKE can be distinguished by the polarization of the incident light. We define the polar and azimuthal angle of the magnetization as $\theta_0$ and $\varphi_0$ respectively, and the angle of the linear polarized incident light polarization as $\phi_0$, then Eq. (6.6) can be rewritten as

$$\Psi = \alpha_{polar} \cos\theta_0 + \frac{1}{2} \beta_{quadratic} \sin^2\theta_0 \sin[2(\varphi_0 - \phi_0)] \tag{6.7}$$

One can find that the polar MOKE response does not depend on the polarization of light; while the quadratic MOKE response is proportional to $\sin[2(\varphi_0 - \phi_0)]$. Our MOKE setup for measuring current-induced magnetization reorientation is schematically illustrated in Figure 6.3. The sample under test is an HM/FM bilayer film. The film was patterned into 50 μm× 50 μm sized square through positive photolithography followed by ion-beam milling. An insulating layer is deposited on top of FM layer to prevent the oxidation. Two electrode pads composed

of Ta (10 nm)/Cu (200 nm)/Au (100 nm) are fabricated on the sides of the sample. A diode laser is used as the light source with 780nm center wavelength. The laser beam is first linearly polarized through a half wave plate (HWP-1) and a quarter wave plate (QWP-1).

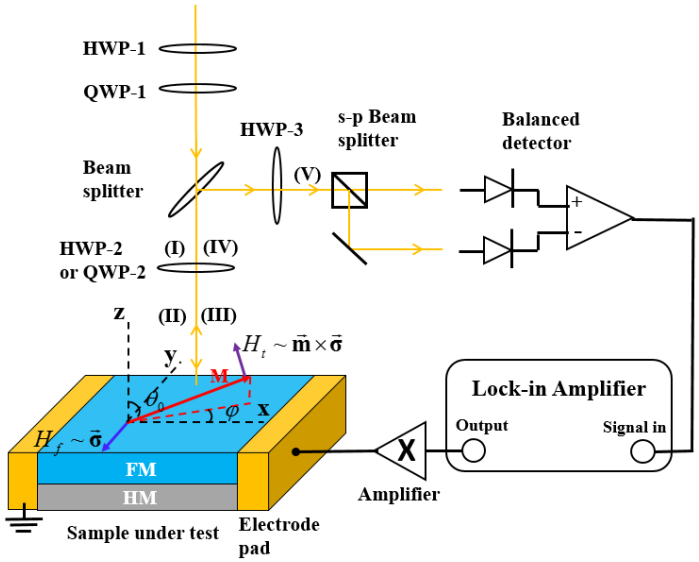


Figure 6.3 Experimental setups of MOKE detection of SOTs.

We analyze the polarization of the light in the optical path at the position indicated by the Roman numerals in Figure 6.3. The light polarization is described via the Jones calculus, where a Jones vector represents the polarized light and Jones matrices represent linear optical elements. The expression of the Jones matrices of Half wave plate, quarter wave plate and magnetic surface are derived in Ref [15,16].

At position I where the light is linearly polarized along the *x*-axis, we define the initial polarization of the light as $\Psi = 0$. The polarization is defined as $P_1 = \begin{bmatrix} 1 \\ 0 \end{bmatrix}$.

Then the light beam passes the HWP-2, whose Jones matrix is $M_{HW}=\begin{bmatrix}\cos 2\phi_{HW} & -\sin 2\phi_{HW}\\ \sin 2\phi_{HW} & \cos 2\phi_{HW}\end{bmatrix}$. $\phi_{HW}$ is the angle of the principle axis of HWP-2 with respect to the *x*-axis. At position II, the polarization can be calculated as

$$P_2 = M_{HW}\cdot P_1 = \begin{bmatrix}\boldsymbol{\cos}\, 2\phi_{HW}\\ \boldsymbol{\sin}\, 2\phi_{HW}\end{bmatrix} \tag{6.8}$$

The second HWP (HWP-2) rotates the polarization angle as $\Psi = 2\phi_{HW}$.

After the laser beam is reflected from the sample, the polarization angle is changed to be $\Psi = 2\phi_{HW} + \Psi[\mathbf{M}]$, where $\Psi[\mathbf{M}]$ is the change of the polarization angle due to the magnetic surface. The Jones Matrix of the magnetic surface is

$$M_k = \begin{bmatrix}\boldsymbol{\cos}\,\varphi_0 & -\boldsymbol{\sin}\,\varphi_0\\ \boldsymbol{\sin}\,\varphi_0 & \boldsymbol{\cos}\,\varphi_0\end{bmatrix}\xi\begin{bmatrix}1+\dfrac{\beta_{quadratic}}{2}\boldsymbol{\sin}^2\theta_0 & -\alpha_{polar}\boldsymbol{\cos}\,\theta_0\\ \alpha_{polar}\boldsymbol{\cos}\,\theta_0 & 1-\dfrac{\beta_{quadratic}}{2}\boldsymbol{\sin}^2\theta_0\end{bmatrix}\begin{bmatrix}\boldsymbol{\cos}\,\varphi_0 & \boldsymbol{\sin}\,\varphi_0\\ -\boldsymbol{\sin}\,\varphi_0 & \boldsymbol{\cos}\,\varphi_0\end{bmatrix} \tag{6.9}$$

where $\theta_0$ and $\varphi_0$ is the polar and azimuthal angle of the magnetization respectively, $\xi$ is the reflection coefficient of the magnetic surface.

The polarization vector at position III can be calculated as

$$P_3 = M_k\cdot P_2 = \xi\left\{\begin{bmatrix}\boldsymbol{\cos}\, 2\phi_{HW}\\ \boldsymbol{\sin}\, 2\phi_{HW}\end{bmatrix} + \alpha_{polar}\boldsymbol{\cos}\,\theta_0\begin{bmatrix}-\boldsymbol{\sin}\, 2\phi_{HW}\\ \boldsymbol{\cos}\, 2\phi_{HW}\end{bmatrix} + \frac{\beta_{quadratic}}{2}\boldsymbol{\sin}^2\theta_0\begin{bmatrix}\boldsymbol{\cos}\, 2(\varphi_0-\phi_{HW})\\ \boldsymbol{\sin}\, 2(\varphi_0-\phi_{HW})\end{bmatrix}\right\} \tag{6.10}$$

Then the light passes through the HWP again, at position IV, the polarization vector is

$$P_4 = M_{HW}\cdot P_3 = \xi\left\{\begin{bmatrix}1\\ 0\end{bmatrix} + \begin{bmatrix}\dfrac{\beta_{quadratic}}{2}\boldsymbol{\sin}^2\theta_0\,\boldsymbol{\cos}(4\phi_{HW}-2\varphi_0)\\ -\alpha_{polar}\boldsymbol{\cos}\,\theta_0 + \dfrac{\beta_{quadratic}}{2}\boldsymbol{\sin}^2\theta_0\,\boldsymbol{\sin}(4\phi_{HW}-2\varphi_0)\end{bmatrix}\right\} \tag{6.11}$$

Therefore, the polarization of the light is $\psi = -\alpha_{polar}\cos\theta_0 + \frac{\beta_{quadratic}}{2}\sin^2\theta_0 \sin\left(4\phi_{HW} - 2\varphi_0\right)$. Substituting $\phi_0 = 2\phi_{HW}$ into the expression, one can derive Eq. (6.7).

Then the light is reflected by the beam splitter and cross another half wave plate (HWP-3). The principle axis of the HWP-3 is set to be $\frac{\pi}{8}$. After passing through HWP-3, the light polarization becomes

$$
\begin{aligned}
P_5 &= \begin{bmatrix} \cos\frac{\pi}{4} & -\sin\frac{\pi}{4} \\ \sin\frac{\pi}{4} & \cos\frac{\pi}{4} \end{bmatrix} \xi \begin{bmatrix} 1 + \frac{\beta_{quadratic}}{2}\sin^2\theta_0 \cos\left(4\phi_{HW} - 2\varphi_0\right) \\ -\alpha_{polar}\cos\theta_0 + \frac{\beta_{quadratic}}{2}\sin^2\theta_0 \sin\left(4\phi_{HW} - 2\varphi_0\right) \end{bmatrix} \\
&= \frac{\xi}{\sqrt{2}} \begin{bmatrix} 1 + \frac{1}{2}\beta_{quadratic}\sin^2\theta_0 \cos\left(4\phi_{HW} - 2\varphi_0\right) - \alpha_{polar}\cos\theta_0 + \frac{\beta_{quadratic}}{2}\sin^2\theta_0 \sin\left(4\phi_{HW} - 2\varphi_0\right) \\ 1 + \frac{1}{2}\beta_{quadratic}\sin^2\theta_0 \cos\left(4\phi_{HW} - 2\varphi_0\right) + \alpha_{polar}\cos\theta_0 - \frac{\beta_{quadratic}}{2}\sin^2\theta_0 \sin\left(4\phi_{HW} - 2\varphi_0\right) \end{bmatrix} \\
&= \begin{bmatrix} E_x \\ E_y \end{bmatrix}
\end{aligned}
\tag{6.12}
$$

The *x* and *y* component of the light is then separated into two beams by the s-p beam splitter and detected by a balanced detector. The voltage output is

$$
\begin{aligned}
V &\propto \left(E_x\right)^2 - \left(E_y\right)^2 \\
&= \xi^2 \left[1 + \frac{1}{2}\beta_{quadratic}\sin^2\theta_0 \cos\left(4\phi_{HW} - 2\varphi_0\right)\right] \times \left[-\alpha_{polar}\cos\theta_0 + \frac{\beta_{quadratic}}{2}\sin^2\theta_0 \sin\left(4\phi_{HW} - 2\varphi_0\right)\right]
\end{aligned}
\tag{6.13}
$$

If we replace the HWP-2 with a quarter-wave plate QWP-2, the linear polarized light becomes circularly polarized light at position II with polarization vector as

$$P_2 = \frac{1-i}{2}\begin{bmatrix}1\\ i\end{bmatrix} \tag{6.14}$$

At position III, the polarization becomes

$$P_3 = \frac{1-i}{2}\zeta\left\{(1-i\alpha_{polar}m_z)\begin{bmatrix}1\\ i\end{bmatrix} + \frac{1}{2}\beta_{quadratic}(\cos\varphi_0 + i\sin\varphi_0)^2\begin{bmatrix}1\\ -i\end{bmatrix}\right\} \tag{6.15}$$

At position IV, the polarization is

$$P_4 = \zeta\left\{\begin{bmatrix}0\\ 1\end{bmatrix} + \begin{bmatrix}\frac{1}{2}\beta_{quadratic}(\sin 2\varphi_0 - i\cos 2\varphi_0)\\ i\alpha_{polar}m_z\end{bmatrix}\right\} \tag{6.16}$$

The total rotation of polarization angle in this case is

$$\Psi = \frac{\pi}{2} - \frac{1}{2}\beta_{quadratic}(\sin 2\varphi_0 - i\cos 2\varphi_0) \tag{6.17}$$

For the DC MOKE measurement, a DC current is applied to the sample. A voltmeter detects the output voltage. As $\phi_{HW} = 22.5^\circ$ and $\varphi_0 = 0^\circ$, the Eq.(6.13) becomes

$$V = -\xi^2\alpha_{polar}\cos\theta_0 \tag{6.18}$$

The form of Eq. (6.18) is the same as common polar MOKE response.

When we apply an in-plane AC current through the sample which leads to an oscillation of the magnetization $\mathbf{m}(t)$ due to SOTs, the corresponding oscillation amplitude of the polar and azimuthal angle of magnetization are $\Delta\theta$ and $\Delta\varphi$, respectively. A lock-in amplifier measures the AC voltage output of the balanced detector as

$$\Delta V = D\xi^2\Delta\psi(\mathbf{m}) \tag{6.19}$$

The pre-factor $D$ relates to the balance detector, lock-in amplifier and other variables in the experimental setup which is hard to determine.

With linear polarized incident light, after differentiation of Eq. (6.7), the magnitude of the oscillation in the Kerr rotation is

$$\left|\Delta\Psi\left[\mathbf{m}(t)\right]\right| = [\alpha_{polar} + \beta_{quadratic}\cos\theta_0 \sin 2(\varphi_0 - \phi_0)]\sin\theta_0\Delta\theta + \beta_{quadratic}\sin^2\theta_0 \cos 2(\varphi_0 - \phi_0)\Delta\varphi \tag{6.20}$$

where $\phi_0 = 2\phi_{HW}$.

When the magnetization is aligned by an external magnetic field in the x-direction, the azimuthal angle of magnetization $\varphi_0$ equals to zero and the polar angle $\theta_0$ equals to 90°. With applying a linear polarized light with polarization $\phi_0 = 45^\circ$, the second term on the right side of Eq.(6.20) equals to zero, and the MOKE signal only depends on the polar angle $\Delta\theta$ as

$$\left|\Delta\Psi\left[\mathbf{m}(t)\right]\right| = \alpha_{polar}\Delta\theta \tag{6.21}$$

Therefore, using light with linear polarization at $\phi_0 = 45^\circ$, one can determine the magnetization out-of-plane rotation.

For the incident light with circular polarization, the differentiation of Eq. (6.17) leads to the magnitude of the oscillation in the Kerr rotation as

$$\left|\Delta\Psi\left[\mathrm{m}(t)\right]\right| = \beta_{quadratic}\cos 2\varphi_0\Delta\varphi \tag{6.22}$$

Therefore, using circularly polarized light, one can measure the magnetization rotation in the film plane.

## 6.3 Analytical Model of the Magnetization Angle Change due to Spin Transfer Torques

The magnetization is rotated from its equilibrium orientation ($\theta_0, \varphi_0$) due to the presence of SOTs. To quantitatively measure the current-induced SOTs, we drive the relation between SOTs and the change of the polar angle $\Delta\theta$ and the azimuthal angle $\Delta\varphi$.

In the system shown in Figure 6.3, the current passing in the HM layer induces effective fields $\Delta H_{x,y,z}$ from SOTs and Oersted field. The effective fields cause small deviation of the magnetization orientation as $\Delta\theta$ and $\Delta\varphi$.

The magnetic energy of the system can be written as

$$E = -K_p \cos^2\theta - K_I \sin^2\varphi \sin^2\theta - \vec{M}\cdot\vec{H} \tag{6.23}$$

where $\theta$ and $\varphi$ are the polar and azimuthal angles of the magnetization, respectively, $K_p$ is the effective out-of-plane anisotropy energy including demagnetizing energy and perpendicular surface anisotropy $K_\perp$, and $K_I$ is the in-plane uniaxial anisotropy energy. In a magnetic thin film, $K_p$ can be expressed as

$$K_p = K_\perp - \frac{1}{2}M_s^2 \tag{6.24}$$

The correspond effective out-of-plane and in-plane anisotropy field can be written as $H_p = \frac{2K_p}{M_s}$ and $H_I = \frac{2K_I}{M_s}$.

To find the equilibrium magnetization directions ($\theta_0, \varphi_0$), one can solve the equations

$$\left.\frac{\partial E}{\partial \theta}\right|_{\theta=\theta_0,\varphi=\varphi_0} = 0 \tag{6.25}$$

$$\left.\frac{\partial E}{\partial \varphi}\right|_{\theta=\theta_0,\varphi=\varphi_0} = 0 \tag{6.26}$$

The small perturbations ( $\Delta\theta, \Delta\varphi$ ) to the magnetization direction are given by

$$\Delta\theta = \frac{\partial\theta}{\partial H_x}\Delta H_x + \frac{\partial\theta}{\partial H_y}\Delta H_y + \frac{\partial\theta}{\partial H_z}\Delta H_z \tag{6.27}$$

$$\Delta\varphi = \frac{\partial\varphi}{\partial H_x}\Delta H_x + \frac{\partial\varphi}{\partial H_y}\Delta H_y + \frac{\partial\varphi}{\partial H_z}\Delta H_z \tag{6.28}$$

We assume that the external magnetic field is much larger than the in-plane uniaxial anisotropy, so that $\varphi_0 = \varphi_H$. We further assume the direction of the external magnetic field is along either *x* or *y*-axis. Eqs. of (6.26) and (6.27) under small angle approximation can be expressed as

$$\Delta\theta = \frac{\cos\theta_0(\Delta H_x \cos\varphi_H + \Delta H_y \sin\varphi_H) - \sin\theta_0 \Delta H_z}{(H_P - H_I \sin^2\varphi_H)\cos 2\theta_0 + H\cos(\theta_H - \theta_0)} \tag{6.29}$$

$$\Delta\varphi = \frac{-\Delta H_x \sin\varphi_H + \Delta H_y \cos\varphi_H}{-H_I \sin\theta_0 \cos 2\varphi_H + H\sin\theta_H} \tag{6.30}$$

Eqs. (6.28) and (6.29) can be further simplified in the particular field and magnetic anisotropy configurations. Here we discussed three cases in the following sections.

### 6.3.1 In-plane Magnetic Anisotropy and X-axis External Magnetic Field

As shown in Figure 6.4, the FM layer has in-plane magnetic anisotropy and the external magnetic field is applied parallel to the current direction, which is along the *x*-axis. Because the demagnetizing field is much larger than the perpendicular surface anisotropy, the magnetization prefers to lie in the film plane. The current generates a spin current with polarization $\vec{\sigma}$ along *y*-axis. The effective

field due to the damping-like torque is $\vec{H}_t \propto \vec{M} \times \vec{\sigma}$, and is parallel to the *z*-axis. The effective field due to field-like torque is $\vec{H}_f \propto \vec{\sigma}$, and is parallel to the *y*-axis.

Therefore, the current induced effective fields can be written as

$$\Delta H_z = H_t \tag{6.31}$$

$$\Delta H_y = H_f + H_{Oe} \tag{6.32}$$

where $H_t$ and $H_f$ are the effective due to damping-like and field-like SOT respectively, $H_{Oe}$ is Oersted field that can be calculated from Ampere's Law.

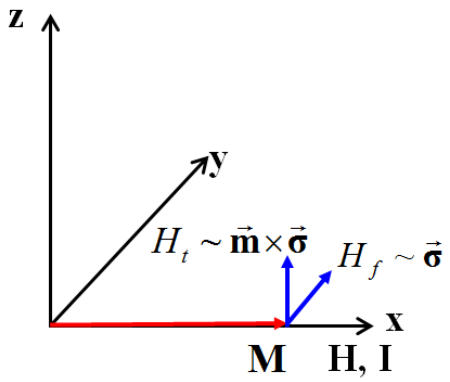


Figure 6.4 the schematic configuration of magnetization, external field, current, and SOTs in the in-plane magnetization geometry.

In this geometry, $\varphi_0 = \varphi_H = 0^\circ, \theta_H \approx 90^\circ$, we can simplify the Eqs. (6.29) and (6.30) as

$$\Delta\theta = \frac{H_t}{H_P - H} \tag{6.33}$$

$$\Delta\varphi = \frac{H_f + H_{Oe}}{H - H_I} \tag{6.34}$$

The effective perpendicular field is almost equal to the demagnetizing field $4\pi M_s$, which is much larger than the applied in-plane magnetic field. Therefore, Eq. (6.33) can be rewritten as

$$\Delta\theta = \frac{H_t}{4\pi M_s} \tag{6.35}$$

The change of polar angle $\Delta\theta$ is directly proportional to the effective field $H_t$ due to the damping-like torque and almost does not depend on the external magnetic field. The change of azimuthal angle $\Delta\varphi$ is directly proportional to the sum of $H_f$ and Oersted field $H_{Oe}$, and is inversely proportional to the external magnetic field. From Eq. (6.21) with 45° linear polarized light, one can find the polar MOKE signal only depends on $\Delta\theta$, or $H_t$. Moreover, with circular polarized incident light, the quadratic MOKE single is proportional to $\Delta\varphi$. By separately measuring polar and quadratic MOKE, one can quantitatively determine $H_t$ and $H_f$.

### 6.3.2 Perpendicular Anisotropy and External Field in *x*-*z* Plane Configuration

This configuration, as illustrated in Figure 6.5, considers the FM layer has perpendicular anisotropy (PMA) and both the external magnetic field and current are applied in the x-axis. Again, the magnetization $\vec{M}$ derivates from its equilibrium direction due to SOTs. The current-driven spin polarization $\vec{\sigma}$ along *y*-axis causes two effective fields as $\vec{H}_t \propto \vec{M} \times \vec{\sigma}$ and $\vec{H}_f \propto \vec{\sigma}$. Therefore, the current induced effective fields can be written as

$$\Delta H_x = -H_t \cos\theta_0 \tag{6.36}$$

$$\Delta H_z = H_t \sin\theta_0 \tag{6.37}$$

$$\Delta H_y = H_f + H_{Oe} \tag{6.38}$$

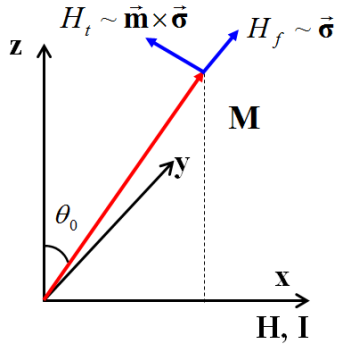


Figure 6.5 the configuration of an FM with perpendicular magnetic anisotropy in a magnetic field applied along the *x*-axis

In this geometry, the field orientation is $\varphi_0 = \varphi_H = 0^\circ, \theta_H \approx 90^\circ$. By substituting Eqs. (6.36), (6.37) and (6.38) into Eqs. (6.29) and (6.30), one can derive the modulation of the magnetization as

$$\Delta\theta = -\frac{H_t}{H_P \cos 2\theta_0 + H \sin\theta_0} \tag{6.39}$$

$$\Delta\varphi = \frac{1}{H - H_I \sin\theta_0}(H_f + H_{Oe}) \tag{6.40}$$

The change of the polar angle depends on the effective field due to the damping-like torque, and the change of the azimuthal angle is proportional to the sum of Oersted field and the effective field due to the field-like torque.

### 6.3.3 Perpendicular Anisotropy and External Field in *y*-*z* Plane Configuration

As shown in Figure 6.6, the magnetization rotates in the *y*-*z* plane with in-plane magnetic field applied along the *y*-axis. The electrical current is still applied along the *x*-axis. In this geometry, the effective field along the *x*-axis is due to the damping-like torque, and the effective field along the *z*-axis is due to the field-like torque. One can write the effective fields as

$$\Delta H_y = (H_f + H_{Oe}) \tag{6.41}$$

$$\Delta H_x = H_t \tag{6.42}$$

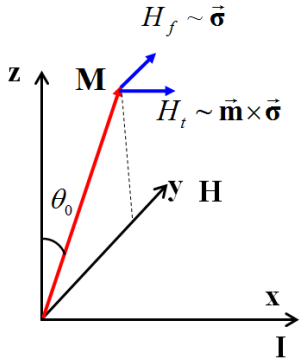


Figure 6.6 Configuration of an FM layer with perpendicular magnetic anisotropy in the external magnetic field applied in the *Y*-axis.

The azimuthal angle of the magnetization and field and the polar angle of the field are $\varphi_0 = \varphi_H = 90^\circ, \theta_H \approx 90^\circ$.

By substituting Eqs. (6.41) and (6.42) into Eqs. (6.29) and (6.30), we get the expression of the magnetization change as

$$\Delta\theta = \frac{1}{(H_P - H_I)\cos 2\theta_0 + H\sin\theta_0}(H_f + H_{Oe})\cos\theta_0 \tag{6.43}$$

$$\Delta\varphi = \frac{1}{H - H_I \sin\theta_0} H_t \tag{6.44}$$

In this scenario, the modulation of polar angle $\Delta\theta$ is proportional to the field-like torque and Oesterd field, and the modulation of the azimuthal angle $\Delta\varphi$ depends on the damping-like torque.

## 6.4 Experimental Detection of SOTs in HM/FM with In-plane Magnetization

We prepared Py (2nm)/Pt (5 nm) thin films with in-plane anisotropy and patterned the film into 50 μm ×50 μm square. A 10 mA AC current with a frequency of 1.7 kHz is applied in the film plane. The MOKE signal was detected by the measurement setup illustrated in Figure 6.3. We investigated the polar and quadratic MOKE by changing the polarization of the incident light. The extracted polarization change is shown in Figure 6.7 (a). With 45° linear polarization, we observe a step-shape curve as we scan the magnetic field. The change of the signal occurs near zero magnetic fields, corresponding to the magnetic switching. The amplitude of the polarization change is independent of the magnetic field as expected from Eq. (6.35). A circularly polarized light is formed by replacing the half wave plate (HWP-2) with a quarter wave plate (QWP-2). In this geometry, only the quadratic MOKE will contribute to the signal without polar MOKE signal as indicated by Eq. (6.22). Figure 6.7 (b) shows the extracted polarization change with 90° linearly polarized light (black curve) and circular incident light (red curve). The signal with circularly polarized light is proportional to 1/*H,* and there is no step-shape signal corresponding to polar MOKE, as expected from Eq. (6.36). There is an offset in the signal with 90° linearly polarized light (black curve) because of the polar MOKE response. To summarize, the polar MOKE signal is detected at 45° linearly polarized incident light, and the quadratic MOKE signal is detected with circularly polarized incident light.

The magnitude of $\alpha_{polar}$ is almost two orders larger than that of $\beta_{quadratic}$[16]. Therefore, the polar MOKE response should be greater than the quadratic MOKE. However, we observed the opposite results in Figure 6.7. This is because, in the in-plane geometry, the out-of-plane magnetization rotation $\Delta\theta$ is small

due to the demagnetization effect, the measured quadratic MOKE signal is, therefore, larger than the polar MOKE signal.

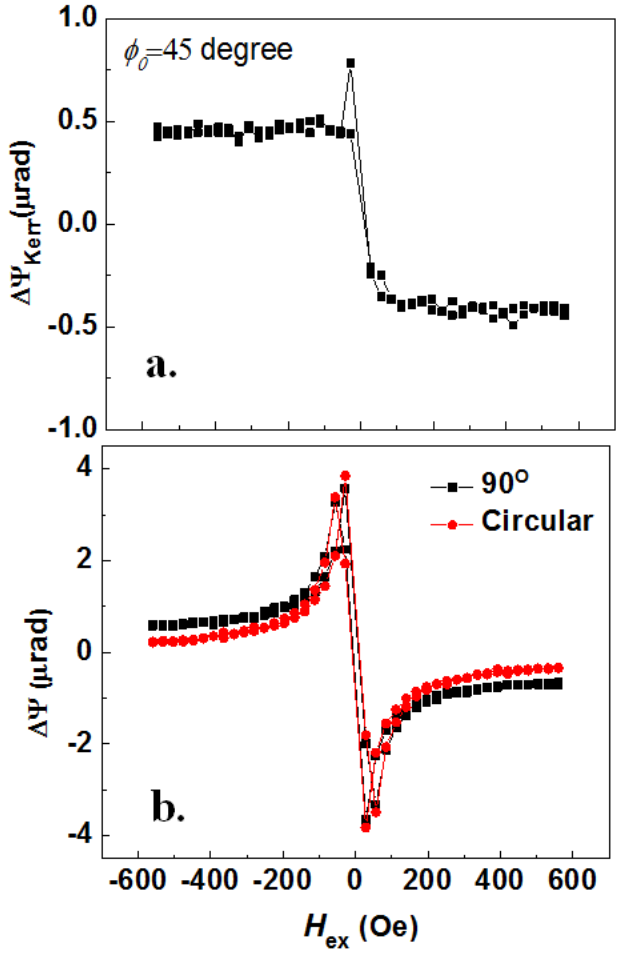


Figure 6.7 (a) the amplitude of polarization oscillation as a function of the external magnetic field with 45° linearly polarized incident light (b) the amplitude of polarization oscillation with 90° linearly polarized light (black curve) and circular incident light (red curve). The sample is Py (2nm)/Pt (5 nm).

## 6.5 Experimental Detection of SOTs in HM/FM with Perpendicular Magnetization

In magnetic thin films with PMA, such as Ta/CoFeB/MgO, the magnetization prefers to lie in the direction normal to the sample plane. In this case, the change of the polar angle due to SOTs will not be suppressed by the demagnetization effect, which occurs in the case of in-plane magnetization. One can expect that the polar MOKE signal would be much larger than the quadratic MOKE because the coefficient $\alpha_{polar} >> \beta_{quadratic}$. Here, we only use polar MOKE single to determine both of the damping-like and field-like torques in two measurement geometries.

To measure the effective field due to damping-like torque**,** the external magnetic field is applied in the *x*-*z* plane. The azimuthal angle of the external magnetic field $\varphi_H = 0$ and the polar angle of magnetic field $\theta_H = 85^\circ$. In Eq. (6.38), the change of the polar angle due to the effective field is only proportional to the effective field $H_t$ from the damping-like torque. Moreover, from Eq. (6.7), we know that the polar MOKE response only depends on the polar angle, when the normal incident light is linearly polarized at 45° with respect to the *x*-axis. We plot the DC polar MOKE signal as a function of the external magnetic field in Figure 6.8. The significant change in the signal near $\pm 100$ Oe indicates the magnetic reversal due to the *z* component of the external magnetic field. Further increasing the magnetic field reduces the MOKE signal because the magnetization gradually rotates towards the film plane. From Eq. (6.7), the equilibrium polar angle of the magnetization $\theta_0$ is obtained from the DC polar MOKE as

$$\cos\theta_0 = \frac{V_{dc}}{V_{dc}(\theta_0 = 0)} \tag{6.45}$$

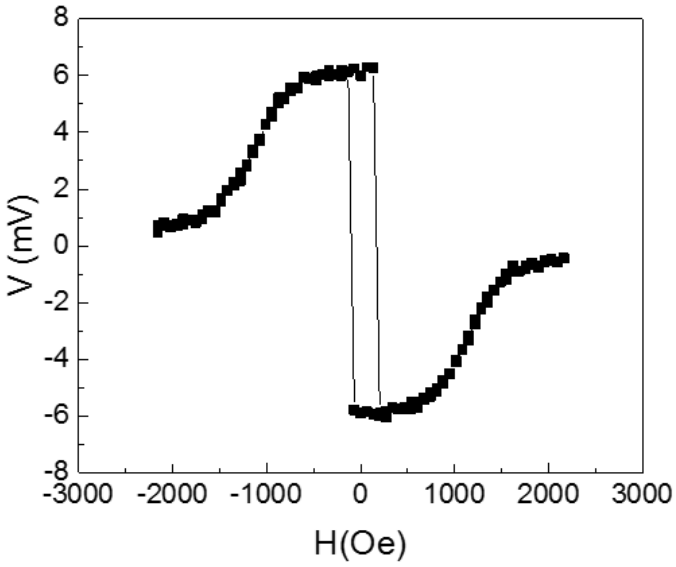


Figure 6.8 DC polar MOKE signal as a function of the external magnetic field. The sample is Ta (3nm) /CoFeB (1nm)/MgO (3nm)/ $SiO_2$(5nm).

According to Eqs. (6.19), (6.20) and (6.39), the second-order polar MOKE single measured by the lock-in amplifier is expressed as

$$\Delta V = -D\xi^2(\alpha_{polar} + \beta_{quadratic}\cos\theta_0)\sin\theta_0 \frac{1}{H_P\cos 2\theta_0 + H\sin\theta_0} H_t \tag{6.46}$$

We developed a method to calibrate the pre-factor $D$ and quantitatively determined the value of $H_t$. Figure 6.9 shows the structure of the sample with a calibration wire, which is a conducting wire made of Ta (10 nm)/Cu (300 nm)/Au (100 nm). The calibration wire is fabricated on the substrate parallel to the sample under test. The width of the wire $w_1$ is 30 μm and the width of the sample under test $w_2$ is 30 μm. The distance $d$ between the conducting wire and the sample under test is 120 μm. The current flowing in the calibration wire will generate a magnetic field $H_{cal}$ perpendicular to the film plane on the sample under test. The magnitude of $H_{cal}$ can be calculated from Ampere's Law. For example, a 100 mA AC current in the calibration wire generates $1.66 \pm 0.16$ Oe magnetic field on the sample perpendicular to the film

plane, where the error is due to the finite width of the sample and calibration wire. This calibration field will induce a perturbation of the magnetization as

$$\Delta\theta = -\frac{\sin\theta_0}{H_P\cos 2\theta_0 + H\sin\theta_0} H_{cal} \tag{6.47}$$

Hence a polar MOKE signal due to the AC calibration field

$$\Delta V_{cal} = D\xi^2(\alpha_{polar} + \beta_{quadratic}\cos\theta_0)\sin\theta_0 \frac{\sin\theta_0}{H_P\cos 2\theta_0 + H\sin\theta_0} H_{cal} \tag{6.48}$$

Comparing Eq. (6.46) and (6.48), we get the effective field due to the damping-like torque as

$$H_t = \frac{\Delta V}{\Delta V_{cal}} H_{cal}\sin\theta_0 \tag{6.49}$$

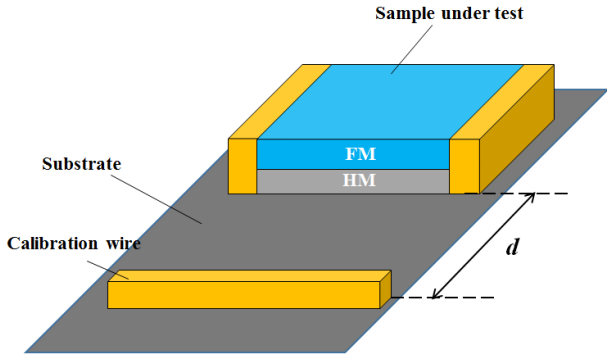


Figure 6.9 The schematics of the sample structure with a calibration wire for AC MOKE measurement.

Figure 6.10 shows the plot of the polar MOKE signal (black curve) due to the anti-damping torque and the calibration field as a function of the external magnetic field (red curve). The symmetry of the two curves is different. The single due to the anti-damping torque is antisymmetric in the field scan because the anti-damping torque $\sim\vec{\boldsymbol{\sigma}}\times\vec{\mathbf{m}}$ is reversed as the magnetization switches direction. The single due to

the calibration field is symmetric in the field scan because it does not change its direction with the DC external field.

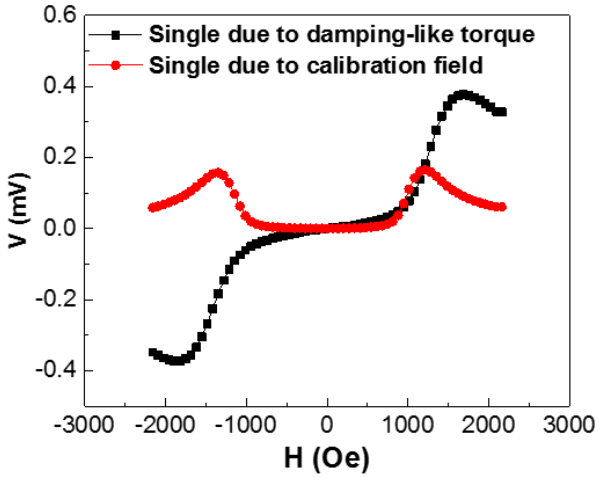


Figure 6.10 The polar MOKE signal when the external magnetic field is applied in the *x*-*z* plane. The black curve is measured when a 1mA AC current is passing through the sample of Ta (3nm) /CoFeB (1nm)/MgO (3nm)/$SiO_2$ (5nm), and the red curve is measured when a 100 mA AC current is passing through the calibration wire

To measure the effective field due to the field-like torque, the external magnetic field is applied in the *y*-*z* plane. The azimuthal and polar angles of the magnetic field are, respectively, $\varphi_H = 90°$ and $\theta_H = 85^\circ$. From Eq. (6.42), the change of the polar angle due to the effective field is proportional to the effective field $H_f$ from the field-like torque and Oersted field $H_{Oe}$. Because Ta is very resistive, $H_{Oe}$ is about 0.1 Oe in the measurement, which is, at least, one order smaller than $H_f$. We can neglect Oersted field in the calculation. Based on Eq. (6.19), (6.44) and (6.48), we can derive the formula to calculate the effective field due to field-like torque as

$$H_f = -\frac{\Delta V}{\Delta V_{cal}} H_{cal} \tan\theta_0 \tag{6.50}$$

Figure 6.11 shows the measured polar MOKE response as a function of the external magnetic field. Similarly, we performed the calibration which is shown in the red curve. The field-dependent symmetry is the same for the polar MOKE and calibration single because both effective field $H_f$ and calibration field $H_{cal}$ do not change their sign with the external magnetic field.

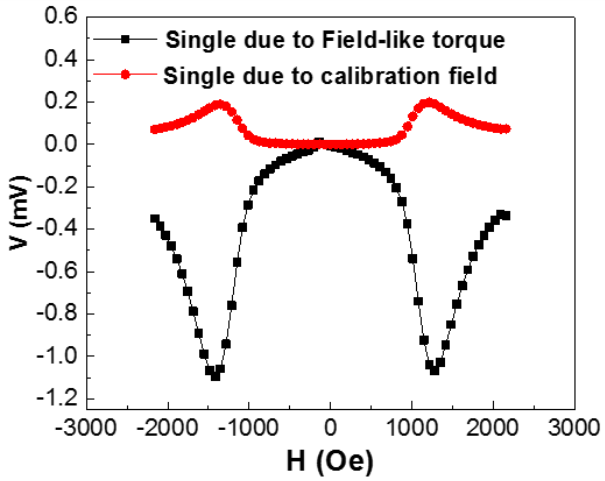


Figure 6.11 The polar MOKE signal when the external magnetic field applied in the *y*-*z* plane. The black curve is measured when a 1mA AC current is passing through the sample of Ta (3nm) /CoFeB (1nm)/MgO (3nm)/$SiO_2$(5nm), and the red curve is measured when a 100 mA AC current is passing through the calibration wire

From Figure (6.10) and (6.11), we calculated the SOT effective fields using Eqs. (6.49) and (6.50). The effective fields are normalized to the current density in the Ta layer. The polar angle at the certain external magnetic field is extracted from DC polar MOKE curve as shown in Figure 6.8. We plot the normalized effective field versus the polar angle in Figure 6.12. The amplitude of the $H_t$ is in the range between 1 to 8 Oe per $10^6$ A/cm$^2$, which is consistent with previously measured studies [18]. The field-like torque $H_f$ has large amplitude than the damping-like torque.

Both the field-like and damping-like torques show strong angle dependence. Theories based on bulk SHE predict no angular dependence of $H_f$ and $H_t$ [19]. The Rashba spin-orbital coupling can give rise to the angle dependence due to the Fermi surface distortion as well as the intrinsic Fermi sea contribution [13]. The angular dependence shown in Figure 6.12 suggests the interface Rashba spin-orbital interaction is a dominant contributor to the SOTs. The, even more, significant angular dependence in the field-like torque also implies the dominance of the Rashba effect. This is reasonable because the hybridization between Co or Fe and oxygen atom at the CoFeB/MgO interface is the origin of the PMA in the structure. It has been reported that the oxygen level at the interface can alter the magnitude, even the sign of SOTs [20]. The non-trivial angular dependence of SOTs is crucial for optimizing spin-torque switching in STT-MRAM. Theoretical simulation based on realistic band structure is necessary to understand the angular dependence. Experimentally, samples with well controlled CoFeB/MgO interface would help to understand the physics.

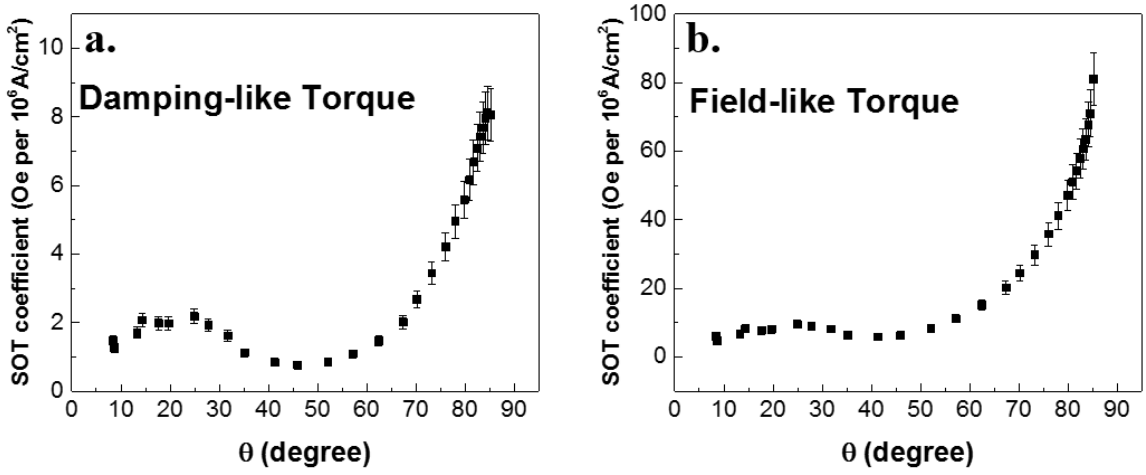


Figure 6.12 The angular dependence of SOT coefficient of (a) damping-like torque and (b) field-like torque. sample Ta (3nm) /CoFeB (1nm)/MgO (3nm)/ $SiO_2$(5nm).

## REFERENCES


[1] Y. Kato, R. Myers, A. Gossard, and D. Awschalom, "Observation of the spin Hall effect in semiconductors," Science, vol. 306, pp. 1910-1913, 2004.

[2] K. Weng, N. Chandrasekhar, C. Miniatura, and B.-G. Englert, "Spin-Orbit Interaction Induced Spin-Separation In Platinum Nanostructure," in Electron Transport in Nanosystems, J. Bonča and S. Kruchinin, Eds., ed: Springer Netherlands, 2008, pp. 49-58.

[3] A. Manchon, H. C. Koo, J. Nitta, S. M. Frolov, and R. A. Duine, "New perspectives for Rashba spin-orbit coupling," Nat Mater, vol. 14, pp. 871-882, 09//print 2015.

[4] N. F. Mott, "The Scattering of Fast Electrons by Atomic Nuclei," Proceedings of the Royal Society of London A: Mathematical, Physical and Engineering Sciences, vol. 124, pp. 425-442, 1929-06-04 00:00:00 1929.

[5] N. F. Mott, "The Polarisation of Electrons by Double Scattering," Proceedings of the Royal Society of London A: Mathematical, Physical and Engineering Sciences, vol. 135, pp. 429-458, 1932-03-01 00:00:00 1932.

[6] G. Vignale, "Ten years of spin Hall effect," Journal of superconductivity and novel magnetism, vol. 23, pp. 3-10, 2010.

[7] J. Wunderlich, B. Kaestner, J. Sinova, and T. Jungwirth, "Experimental Observation of the Spin-Hall Effect in a Two-Dimensional Spin-Orbit Coupled Semiconductor System," Physical Review Letters, vol. 94, p. 047204, 02/04/ 2005.

[8] K. Nomura, J. Wunderlich, J. Sinova, B. Kaestner, A. H. MacDonald, and T. Jungwirth, "Edge-spin accumulation in semiconductor two-dimensional hole gasses," Physical Review B, vol. 72, p. 245330, 12/21/ 2005.

[9] L. Liu, C.-F. Pai, Y. Li, H. Tseng, D. Ralph, and R. Buhrman, "Spin-torque switching with the giant spin Hall effect of tantalum," Science, vol. 336, pp. 555-558, 2012.

[10] L. Liu, T. Moriyama, D. Ralph, and R. Buhrman, "Spin-torque ferromagnetic resonance induced by the spin Hall effect," Physical review letters, vol. 106, p. 036601, 2011.

[11] L. Vila, T. Kimura, and Y. Otani, "Evolution of the spin Hall effect in Pt nanowires: size and temperature effects," arXiv preprint arXiv:0709.2756, 2007.

[12] I. M. Miron, G. Gaudin, S. Auffret, B. Rodmacq, A. Schuhl, S. Pizzini, et al., "Current-driven spin torque induced by the Rashba effect in a ferromagnetic metal layer," Nature Materials, vol. 9, pp. 230-234, 2010.

[13] K.-S. Lee, D. Go, A. Manchon, P. M. Haney, M. Stiles, H.-W. Lee, et al., "Angular dependence of spin-orbit spin-transfer torques," Physical Review B, vol. 91, p. 144401, 2015.

[14] J. Hamrlová, J. Hamrle, K. Postava, and J. Pištora, "Quadratic-in-magnetization permittivity and conductivity tensor in cubic crystals," Physica status solidi (b), vol. 250, pp. 2194-2205, 2013.

[15] X. Fan, A. R. Mellnik, W. Wang, N. Reynolds, T. Wang, H. Celik, et al., "All-Optical Vector Measurement of Spin-Orbit-Induced Torques Using Both Polar and Quadratic Magneto-Optic Kerr Effects," arXiv preprint arXiv:1509.01266, 2015.

[16] C. Dehesa-Martínez, L. Blanco-Gutierrez, M. Vélez, J. Díaz, L. Alvarez-Prado, and J. Alameda, "Magneto-optical transverse Kerr effect in multilayers," Physical Review B, vol. 64, p. 024417, 2001.

[17] J. Hamrlová, J. Hamrle, K. Postava, and J. Pištora, "Quadratic-in-magnetization permittivity and conductivity tensor in cubic crystals," Physica status solidi (b), vol. 250, pp. 2194-2205, 2013.

[18] K. Garello, I. M. Miron, C. O. Avci, F. Freimuth, Y. Mokrousov, S. Blugel, et al., "Symmetry and magnitude of spin-orbit torques in ferromagnetic heterostructures," Nat Nano, vol. 8, pp. 587-593, 08//print 2013.

[19] P. M. Haney, H.-W. Lee, K.-J. Lee, A. Manchon, and M. D. Stiles, "Current-induced torques and interfacial spin-orbit coupling: Semiclassical modeling," Physical Review B, vol. 87, p. 174411, 05/07/ 2013.

[20] X. Qiu, K. Narayana Pillai, Y. Wu, P. Deorani, D.-H. Yang, W.-S. Noh, et al., "Spin–orbit-torque engineering via oxygen manipulation," Nature Nanotechnology, vol. 10, pp. 333-338, 2015.

# Chapter 7

# TUNABLE MAGNETIC RESONANCE THROUGH EXCHANGE INTERACTION

## 7.1 Introduction

The magnetic resonance is a powerful technique to characterize the magnetic properties of materials to extract the saturation magnetization, magnetic anisotropy, and damping constant [1, 2]. Since the ferromagnetic resonance (FMR) frequency of a typical magnetic material, like Ni, Fe, and their alloys, is in the microwave frequency region, it is deployed in microwave applications such as microwave filters, insulators, and circulators [3-5]. With the development of spintronics, people have demonstrated microwave generators [6] and detectors [7] based on spintronics devices. The resonance frequency is determined by the total effective field that includes the external magnetic field, anisotropy field, exchange interaction and dipolar interaction [1, 8]. The quest for reduced energy consumption and enhanced integration density in the microwave and spintronic devices is demanding new techniques for controlling the magnetic resonance without applying a large external magnetic field, which is typically generated by a bulky and energy hungry electromagnet. Research efforts have been made to realize electric voltage control of magnetization dynamics using multiferroic materials [9, 10], where the magnetic dynamics is coupled with the ferroelectric properties. Another conventional method is to utilize the magnetoelastic effect to modify the magnetic anisotropy of a

magnetic thin film with a piezoelectric substrate [11-13]. Most recent the development of electric field controlled magnetic anisotropy via controlling the spin-orbital interaction has also opened a new route to tune electrically magnetism [14, 15]. All these techniques typically have a narrow window for materials selections and have a limited range to tune the resonance frequency. Exchange interaction exists inside every magnetic material and also at the interface of two different magnetic materials. In a typical ferromagnetic material, the exchange field arising from the Pauli Exclusion Principle can be as high as $10^3$ T [16], equivalent to a 28 THz frequency range. By engineering the interlayer exchange interaction in magnetic bilayer heterostructures, we show the great efficiency to design magnetic dynamics with a large tunable resonance frequency.

In a magnetic bilayer consisting of two different ferromagnetic thin films FM1/FM2, the exchange coupling at the interface generates an effective field that correlates the magnetization dynamics in FM1 and FM2 layers. The strength of the exchange coupling depends on the details of the interface and the thicknesses of individual layers. When the interface exchange coupling is finite but much weaker than the intralayer exchange coupling inside each ferromagnetic layer, the collective magnetization precession behaves much like inductively coupled LC resonators [17], where the magnetization precession is quasi-uniform in each layer [12]. The bilayer exhibits two microwave-resonance modes: acoustic mode with the magnetizations in two layers precessing in-phase and optical mode with two magnetizations precessing out-of-phase as illustrated in Figure 7.1. The optical mode is hard to be observed in most of FMR measurements because their excitation efficiencies are too small. In the simplest scenario when the two layers are identical and magnetic anisotropy is

negligible, the two resonance frequencies are respectively as

[12] $\omega_{acoustic} = \gamma\mu_0\sqrt{H(H+M_s)}$ and $\omega_{optical} = \gamma\mu_0\sqrt{\left(\frac{2J}{\mu_0 M_s d}+H\right)\left(\frac{2J}{\mu_0 M_s d}+H+M_s\right)}$,

where $J$ is the interface exchange constant in a unit of J/m$^2$, and $d$ is the layer thickness. Note that $J>0$ and $J<0$ correspond to ferromagnetic and antiferromagnetic couplings respectively. In the optical mode, the resonance frequency is enhanced as if there is an additional magnetic field due to the interface exchange interaction of $\frac{2J}{\mu_0 M_s d}$ when $J>0$. The non-collinear magnetization at the interface increases the energy during precession and hence the resonance frequency of the optical mode. It should be noted that the dipolar interaction, besides exchange interaction, also contributes to the effective field [18]. However, in our samples, the dipolar interaction is expected to be negligible due to the large aspect ratio of the lateral film size over the thickness.

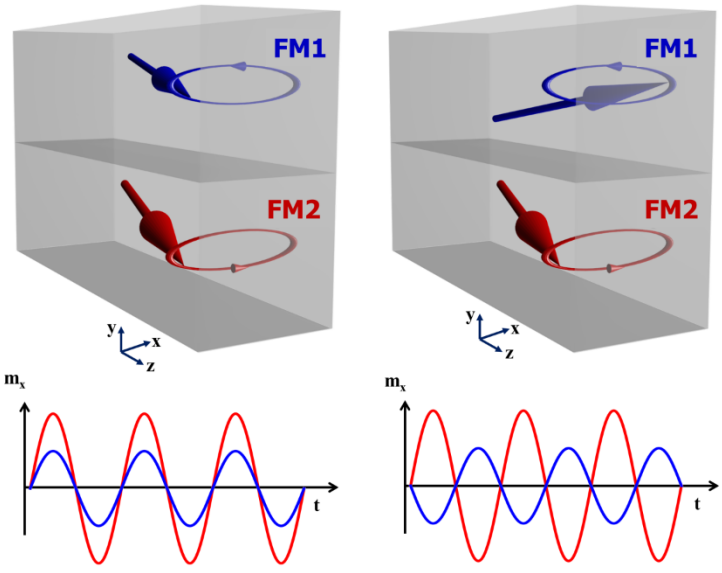


Figure 7.1 Illustration of the magnetization precession of the acoustic and optical modes. The two magnetizations precess in phase in the acoustic mode (left panel) and out of phase in the optical mode (right panel).

## 7.2 Analytical Model of Magnetic Dynamics in Exchange Coupled Multilayers

The LLG equation describes the time evolution of magnetization in ferromagnetic materials in effective magnetic fields. The solution of the LLG equation provides information of magnetic resonance. To understand the magnetic resonance in the magnetic bilayer, we perform simulations with the numerical method and analytical method.

### 7.2.1 Numerical Simulation

As we described in Chapter 4, the LLG equation can be numerically solved by the 4th order Runge-Kutta method. Here we use the same approach to solve the modified LLG equations:

$$\begin{cases} \dfrac{d\vec{M}_1}{dt} = -\gamma \vec{M}_1 \times \left( \vec{H}_{eff1} + A_{12}\vec{M}_2 \right) + \dfrac{\alpha_1}{M_{1s}} \vec{M}_1 \times \dfrac{d\vec{M}_1}{dt} \\ \dfrac{d\vec{M}_2}{dt} = -\gamma \vec{M}_2 \times \left( \vec{H}_{eff2} + A_{21}\vec{M}_1 \right) + \dfrac{\alpha_2}{M_{2s}} \vec{M}_2 \times \dfrac{d\vec{M}_2}{dt} \end{cases} \tag{7.1}$$

where $\gamma$ is the gyromagnetic ratio, $\vec{H}_{effi}$ is the other effective field in the *i*-th layer including the external field, anisotropy field and demagnetizing field, $\alpha_i$ is the damping constant of the *i*-th layer, and $M_{is}$ is the saturation magnetization of the *i*-th layer, $A_{12} = \dfrac{J_{12}}{M_{1s}M_{2s}t_1}$ and $A_{21} = \dfrac{J_{12}}{M_{1s}M_{2s}t_2}$ are the interlayer exchange stiffness of the 1st layer and 2rd layer.

The process to calculate the magnetic susceptibility spectrum is as follow:

1. At a certain microwave frequency and external field, the time dependent magnetization ***M1(t)*** and ***M2(t)*** are got from solving Eq. (5.1) by RK4 method described in Chapter 4.

2. The magnetic susceptibility of each layer $\chi_1$ and $\chi_2$ are calculated by Fourier transformation of ***M1(t)*** and ***M2(t)***.

3. The overall susceptibility $\chi_{total}$ of the bilayer is equal to the sum of $\chi_1$ and $\chi_2$.

4. Change the microwave frequency, and repeat step 1-3 to get $\chi_{total}$, $\chi_1$, and $\chi_2$ at this frequency.

5. The plot $\chi_{total}$, $\chi_1$, and $\chi_2$ versus microwave frequency.

The numerical simulation captures the basic physics information of the magnetic resonance in the magnetic bilayer. However, the code of the model is complex and the time needed to get the results is very long, usually 3-5 hours, depending on the accuracy of the calculation and number of the frequency points. Moreover, the modified LLG equation (7.1) is not valid when the interlayer exchange coupling is comparable with intralayer exchange coupling inside magnetic materials, which would require a multilayer model. To simulate the resonance modes in the multilayer, the numerical method becomes more complicated and time-consuming. An analytical model is developed to solve the LLG equation in magnetic multilayers.

### 7.2.2 Analytical simulation

Two requirements have to be fulfilled to solve LLG equation analytically. First, the magnetic film is aligned by the external magnetic field. The spin precession is uniform and coherent in the film plane. Therefore, each layer can be considered as a single spin in the model. The spin precession might be non-uniform along the direction normal to the film plane. Second, the precession amplitude (angle) is small, and the system is in the linear region so that the LLG equation can be simplified.

**Magnetic resonance in single magnetic layer**

We first derive the analytical solution to the LLG equation for the single magnetic layer. In this layer, the magnetization is aligned by the external magnetic field $H_{ext}$ in the $z$-axis and RF magnetic field is along the $x$-axis. The LLG equation has a simple expression as

$$\frac{d\vec{M}}{dt} = -\gamma\vec{M} \times \vec{H}_{eff} + \frac{\alpha}{M_s}\vec{M} \times \frac{d\vec{M}}{dt} \tag{7.2}$$

The magnetic film and field configuration is schematically illustrated in Figure 7.2. The external magnetic field aligns magnetization along the $z$-axis, and RF magnetic field $h_{rf}$ is along the $x$-axis. We can write the effective field as

$$\vec{H}_{eff} = \{0,0,H_{ext}\} + \{0,-4\pi m_y,0\} + \{h_{rf}e^{i\omega t},0,0\} \tag{7.3}$$

where the first, second and third terms correspond to the external magnetic field, demagnetization field, and RF field, respectively. The uniaxial magnetic anisotropy field in the soft magnetic material is subtle and is neglected here.

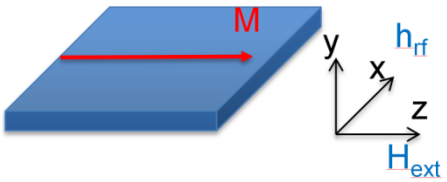


Figure 7.2 Illustration of magnetization and field configuration in single magnetic layer

As the magnetization is precessing around the $z$-axis with a small precessing angle, the magnetization is written as

$$\vec{M} = \{m_x e^{i\omega t}, m_y e^{i\omega t}, M_s\} \tag{7.4}$$

where $m_x$ and $m_y$ are the $x$ and $y$ component of the magnetization which is corresponding to magnetization precession, the $z$ component of magnetization is equal to the saturation magnetization $M_s$ due to the presence of external magnetic field along the $z$-axis.

The small-amplitude motion the magnetization is related to the excitation RF magnetic field with the Polder susceptibility tensor as

$$\begin{pmatrix} m_x \\ m_y \end{pmatrix} = \chi \begin{pmatrix} h_x \\ h_y \end{pmatrix} \tag{7.5}$$

where the Polder susceptibility tensor $\chi = \begin{pmatrix} \chi_{xx} & \chi_{xy} \\ \chi_{yx} & \chi_{yy} \end{pmatrix}$

Substituting Equation (7.3) and (7.4) into Equation (7.2), two matrix equations can be derived

$$\begin{vmatrix} \frac{i\omega}{\gamma} & H_{ext} + 4\pi M_s \\ -H_{ext} & \frac{i\omega}{\gamma} \end{vmatrix} = 0 \tag{7.6}$$

$$\begin{bmatrix} \frac{i\omega}{\gamma} & H_{ext} + 4\pi M_s + \frac{i\alpha\omega}{\gamma} \\ -H_{ext} - \frac{i\alpha\omega}{\gamma} & \frac{i\omega}{\gamma} \end{bmatrix} \begin{bmatrix} m_x \\ m_y \end{bmatrix} = \begin{bmatrix} 0 & 0 \\ -M_s & 0 \end{bmatrix} \cdot \begin{bmatrix} h_{rf} \\ 0 \end{bmatrix} \tag{7.7}$$

The dispersion relation is calculated by solving the first equation as $\omega = \gamma\sqrt{H_{ext}(H_{ext} + 4\pi M_s)}$, which is the Kittel equation for magnetic thin films with in-plane magnetic anisotropy.

Comparing Equation (7.7) and Equation (7.5), we can solve the magnetic susceptibility.

Define matrix

$$D_m = \begin{bmatrix} \frac{i\omega}{\gamma} & H_{ext} + 4\pi M_s \\ -H_{ext} & \frac{i\omega}{\gamma} \end{bmatrix} \qquad g = \begin{bmatrix} 0 & \frac{i\alpha\omega}{\gamma} \\ -\frac{i\alpha\omega}{\gamma} & 0 \end{bmatrix}$$

$$D = D_m + g \qquad \chi = \begin{bmatrix} \chi_{xx} \\ \chi_{xy} \end{bmatrix}$$

$$b = \begin{bmatrix} 0 \\ -Ms \end{bmatrix}$$

The susceptibility is calculated as

$$\chi = D^{-1} \cdot b \tag{7.8}$$

The susceptibility components $\chi_{yx}$ and $\chi_{yy}$ are not considered because the $y$-component of the RF magnetic field $h_y$=0.

**Magnetic resonance in magnetic bilayer**

The modified LLG equation for magnetic bilayer is the same as Eq. (7.1). We can follow the same procedure to solve the magnetic resonance from LLG equation as we described. The field configuration is the same as the previous section. First, we build the matrix

$$D_m = \begin{bmatrix} \frac{i\omega}{\gamma} & H_{ext} + 4\pi M_{1s} & 0 & 0 \\ -H_{ext} & \frac{i\omega}{\gamma} & 0 & 0 \\ 0 & 0 & \frac{i\omega}{\gamma} & H_{ext} + 4\pi M_{2s} \\ 0 & 0 & -H_{ext} & \frac{i\omega}{\gamma} \end{bmatrix} + \begin{bmatrix} 0 & A_{12}M_{2s} & 0 & -A_{12}M_{1s} \\ -A_{12}M_{2s} & 0 & A_{12}M_{1s} & 0 \\ 0 & -A_{21}M_{2s} & 0 & A_{21}M_{1s} \\ A_{21}M_{2s} & 0 & -A_{21}M_{1s} & 0 \end{bmatrix}$$

$$g = \begin{bmatrix} 0 & \frac{i\alpha_1\omega}{\gamma} & 0 & 0 \\ -\frac{i\alpha_1\omega}{\gamma} & 0 & 0 & 0 \\ 0 & 0 & 0 & \frac{i\alpha_2\omega}{\gamma} \\ 0 & 0 & -\frac{i\alpha_2\omega}{\gamma} & 0 \end{bmatrix} \qquad D = D_m + g$$

$$b_1 = \begin{bmatrix} 0 \\ -M_{1s} \\ 0 \\ 0 \end{bmatrix} \qquad b_2 = \begin{bmatrix} 0 \\ 0 \\ 0 \\ -M_{2s} \end{bmatrix}$$

The dispersion relation ω is calculated from

$$|D_m| = 0 \tag{7.9}$$

The magnetic susceptibility of each layer can be calculated by

$$\chi_1 = \begin{bmatrix} \chi_{x_1x_1} \\ \chi_{x_1y_1} \\ \chi_{x_1x_2} \\ \chi_{x_1y_2} \end{bmatrix} = D^{-1} \cdot b_1 \tag{7.10}$$

$$\chi_2 = \begin{bmatrix} \chi_{x_2x_1} \\ \chi_{x_2y_1} \\ \chi_{x_2x_2} \\ \chi_{x_2y_2} \end{bmatrix} = D^{-1} \cdot b_2 \tag{7.11}$$

The total magnetic susceptibility equals to the sum of susceptibility of each layer

$$\chi_{xx,total} = \chi_{xx1} + \chi_{xx2} = (\chi_{x_1x_1} + \chi_{x_1x_2}) + (\chi_{x_2x_1} + \chi_{x_2x_2}) \tag{7.12}$$

**Magnetic resonance in magnetic multilayer**

In a magnetic bilayer composed of FM1 and FM2, when the interlayer exchange coupling is much weaker than the exchange interaction inside FM1 and FM2, the magnetic dynamics is uniform and coherent in each magnetic layer. The model of bilayer we described above is valid. When the interlayer exchange coupling is comparable with the intralayer exchange coupling, the magnetic precession becomes non-uniform along the thickness direction. A multilayer model is needed to simulate the magnetic dynamics.

The magnetic bilayer can be discretized into the multi-atomic-layer system as shown in Figure 7.3. Assuming a uniform excitation in the film plane, we expect coherent precession inside each discretized layer. Due to the thin film geometry, the dipolar interaction among layers is negligible. The dominating interlayer interaction is the exchange coupling between two nearest neighboring layers. For a magnetic atomic layer *i*, the exchange coupling results in an effective field of $\vec{H}_{e\_i} = A_{i,i-1}\vec{M}_{i-1} + A_{i,i+1}\vec{M}_{i+1}$, where $A_{ij}$ denotes the interlayer exchange stiffness between layer *i* and layer *j*, and $\vec{M}_i$ is the magnetization vector of the *i*-th layer. The relation between exchange stiffness $A$ and exchange strength $J$ is $A = J \cdot t$, where $t$ is the thickness of the layer. The coupled magnetization dynamics can then be described by the modified Landau-Lifshitz-Gilbert (LLG) equation,

$$\frac{d\vec{\mathbf{M}}_i}{dt} = -\gamma\mu_0\vec{\mathbf{M}}_i \times \left(\vec{\mathbf{H}}_{eff\_i} + \vec{\mathbf{H}}_{e\_i}\right) + \frac{\alpha_i}{M_{s\_i}}\vec{\mathbf{M}}_i \times \frac{d\vec{\mathbf{M}}_i}{dt} \tag{7.10}$$

where $\gamma$ is the gyromagnetic ratio, $\vec{\mathbf{H}}_{eff\_i}$ is the other effective field on the *i*-th layer including the external field, anisotropy field and demagnetizing field, $\alpha_i$ is the

damping constant of the *i*-th layer, and $M_{s\_i}$ is the saturation magnetization of the *i*-th layer.

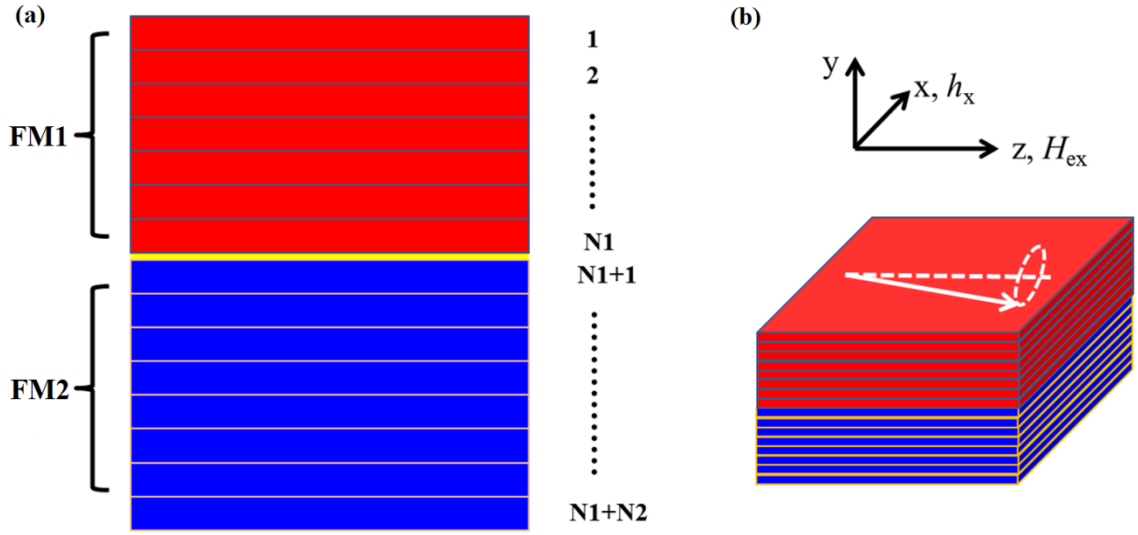


Figure 7.3Discretizing magnetic bilayer. (a) Illustration of separating a magnetic bilayer into N=N1+N2 layers, where N1 and N2 are the total numbers of atomic layers of the two magnetic layers, respectively. (b) Sketch of field geometry for the small angle precession approximation.

Using the same procedure, we can solve LLG equation of multilayer. We first build up the 2N×2N matrix for the total N layers of atomic layer

$$D_m = \begin{bmatrix} \frac{i\omega}{\gamma} & H_{ext}+4\pi M_{1s}+A_{12}M_{2s} & 0 & -A_{12}M_{1s} & 0 & \cdots & 0 & 0 \\ -H_{ext}-A_{12}M_{2s} & \frac{i\omega}{\gamma} & A_{12}M_{1s} & 0 & 0 & \cdots & 0 & 0 \\ 0 & -A_{21}M_{2s} & \frac{i\omega}{\gamma} & H_{ext}+4\pi M_{2s}+A_{21}M_{1s}+A_{23}M_{3s} & 0 & -A_{23}M_{2s}-A_{21}M_{1s} & & \\ A_{21}M_{2s} & 0 & -H_{ext}-A_{21}M_{1s}-A_{23}M_{3s} & \frac{i\omega}{\gamma} & A_{23}M_{2s}+A_{21}M_{1s} & 0 & & \\ . & . & . & . & . & . & & \\ . & . & . & . & . & . & & \\ 0 & 0 & 0 & 0 & 0 & 0 & & \\ 0 & 0 & 0 & 0 & 0 & 0 & & \end{bmatrix}$$

$$D = D_m + g$$

$$g = \begin{bmatrix} 0 & \frac{i\alpha_1\omega}{\gamma} & 0 & \dots & 0 \\ -\frac{i\alpha_1\omega}{\gamma} & 0 & 0 & \dots & 0 \\ 0 & 0 & 0 & \dots & 0 \\ \dots & \dots & & 0 & \frac{i\alpha_N\omega}{\gamma} \\ 0 & 0 & & -\frac{i\alpha_N\omega}{\gamma} & 0 \end{bmatrix} \qquad b_i = \begin{bmatrix} 0 \\ 0 \\ \cdot \\ \cdot \\ \cdot \\ 0 \\ -M_{is} \\ \cdot \\ \cdot \\ \cdot \\ 0 \\ 0 \end{bmatrix}$$

The dispersion relation ω is solved from Equation (7.9). The magnetic susceptibility vector of each layer can be calculated by

$$\chi_i = D^{-1} b_i \tag{7.13}$$

Then the susceptibility of *i*-th layer is

$$\chi_{xx_i} = \sum_j \chi_{x_j x_i} \tag{7.14}$$

The total susceptibility of the multilayer is calculated by

$$\chi_{xx,total} = \sum_i \chi_{xx_i} \tag{7.15}$$

Figure 7.4 shows the simulated the FMR spectrum of the susceptibility of 5nm CoFe/ 5nm NiFe bilayer, where the saturation magnetization of CoFe and NiFe are 1.8 T and 0.9 T, respectively. The unit of susceptibility is arbitrary. The external magnetic field is 300 Oe. The susceptibility of individual CoFe and NiFe layers are plotted as red and blue curves, and the back curve is the total susceptibility. When the interlayer exchange interaction is zero, the two layers will precess individually leading to two resonance peaks at 4.7GHz and 6.6GHz, which equal to the same frequencies determined by the Kittle equation of each layer. When the interlayer exchange coupling strength is increased to 0.25 mJ/m$^2$, the bilayer exhibits two microwave-

resonance modes: acoustic mode at 5.5GHz with the magnetizations in two layers precessing in-phase and optical mode at 12.2GHz with two magnetizations precessing out-of-phase. The magnetic susceptibility of NiFe and CoFe are all positive at acoustic mode; while the sign of susceptibility is opposite at optical mode. As a result, the intensity of the optical mode is smaller than that of the acoustic mode. However, the frequency of the optical mode is much higher than the uniform mode in CoFe shown in Figure 7.4 (a).

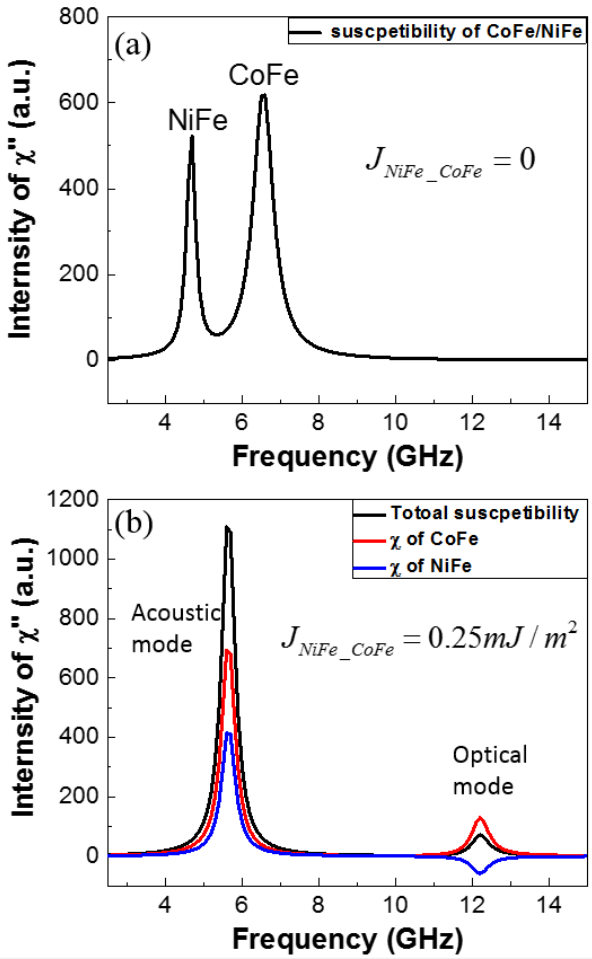


Figure 7.4 Imaginary part of magnetic susceptibility as a function of microwave excitation frequency for 5 nm CoFe/ 5nm NiFe bilayer with (a) interlayer exchange coupling strength $J_{CoFe\_NiFe}$=0 and (b) $J_{CoFe\_NiFe}$=0.25 J/m$^2$.

Figure 7.5 presents the evolution of the acoustic and optical modes as the interlayer exchange interaction increases. The intensity of the modes is indicated by the color bar. The frequency of the optical mode increases much faster with the interlayer exchange interaction than the frequency of the acoustic mode.

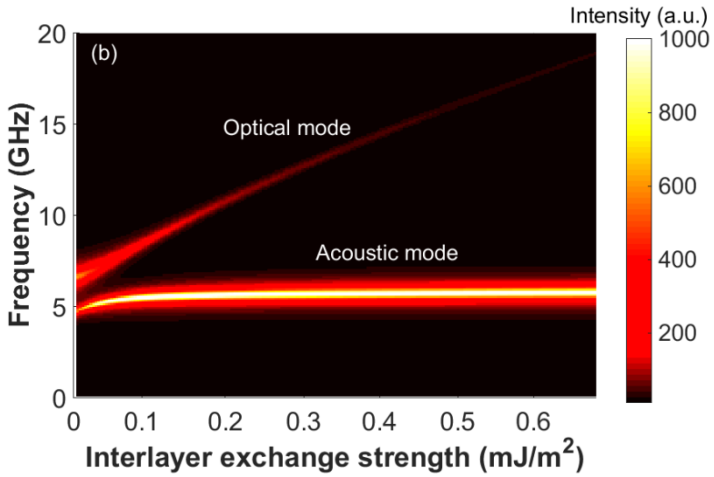


Figure 7.5 Calculated frequency of acoustic and optical modes as a function of the interlayer exchange strength for 5nm CoFe/ 5nm NiFe bilayer. Color bar indicates the intensity of the resonance modes.

With zero interlayer exchange interaction, the intensity of the optical mode is higher than that of the acoustic mode. This is because each layer precesses independently and the high-frequency mode is from the resonance in CoFe. As the exchange interaction increases, the precession energy in one is transmitted to the other layer. The intensity of the optical mode becomes smaller than that of the acoustic mode. For week exchange interaction (JCoFe_NiFe<0.05 mJ/m$^2$), the frequency of both optical mode and acoustic mode are enhanced with the increase of the interaction. At strong exchange interaction region, the optical mode intensity decreases very fast. Two mechanisms cause the intensity decrease. First, the magnetic susceptibility decrease as 1/f with frequency increase which is the nature of ferromagnetic resonance. The increase in the frequency of optical mode leads to a reduction in the intensity. Second, the precession in the CoFe and NiFe are out-of-phase at optical mode, leading to the cancelation of the total susceptibility. The intensity of the precession in CoFe and NiFe at optical mode becomes closer because the precession energy of CoFe

transmitted to NiFe with the increase of exchange interaction. Therefore, the amplitude of the optical mode is dramatically reduced.

To enhance the intensity of the optical mode, one can make the magnetic bilayer with a strong ferromagnetic (FM) layer and a week ferromagnetic (fm) layer. Therefore, the intensity of the optical mode is dominated by the precession in FM layer. Moreover, the frequency of the optical mode still can be enhanced by the interlayer exchange interaction. We choose NiFeCu as fm material. Its magnetization is reduced from NiFe by non-magnetic Cu doping. The value of Ms of is NiFeCu 0.35 T in the simulation. The FM material is CoFe. Figure 7.6 shows the optical mode of CoFe (5 nm)/ NiFe (5 nm) and CoFe(5 nm) / NiFeCu(5 nm) bilayers. For comparison purpose, we also show the resonance mode of single 5 nm CoFe layer. The interlayer exchange interaction is adjusted to make the optical modes of both bilayers appear at the same frequency at 12.2 GHz. The external magnetic field for both CoFe(5 nm) /NiFe(5 nm) and CoFe(5 nm) / NiFeCu(5 nm) bilayers is 300 Oe. And for single 5 nm CoFe layer the external magnetic field is 1000 Oe to make its FMR resonance at 12.2 GHz. The intensity of the optical mode in CoFe(5 nm) / NiFeC(5 nm) u is higher than that of the optical mode in CoFe(5 nm) / NiFe(5 nm) bilayer. Comparing the three resonance peaks in Figure 7.6, the intensity of the optical mode of CoFe(5 nm) / NiFeCu(5 nm) is 48% of the resonance mode in single CoFe layer, and is 26% more than that of the optical mode in CoFe(5 nm)/NiFe(5 nm) bilayer.

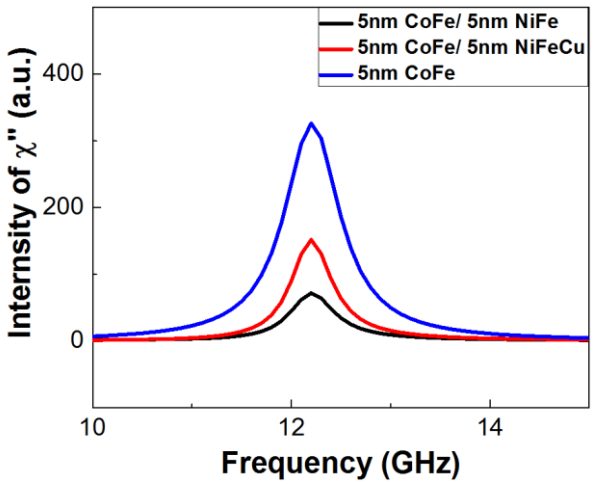


Figure 7.6 The resonance mode at 12.2 GHz in three structures. (1) The optical mode in 5 nm CoFe/5 nm NiFe bilayer (black). The interlayer interaction strength is 0.25 J/m$^2$. The external magnetic field is 300 Oe. (2) The optical mode in 5 nm CoFe/5 nm NiFeCu bilayer (red). The interlayer interaction strength is 0.21 J/m$^2$. The external magnetic field is 300 Oe. (3) The resonance mode in 5nm CoFe layer. The external magnetic field is 1000 Oe.

Figure 7.7 shows the frequency of the optical and acoustic mode in 5 nm CoFe/5 nm NiFeCu bilayer as a function of the interlayer exchange strength. Comparing Figure 7.7 with Figure 7.5, we can find that the optical mode intensity is higher in Figure 7.7. Moreover, we observe an increase in the frequency shift of the optical mode when the exchange interaction is changed. This effect is due to the smaller magnetization of NiFeCu than NiFe. The effective interlayer exchange field is given by $H_{ex} = \frac{J}{M_s t}$ , where Ms is the saturation magnetization. Since Ms of NiFeCu is lower than Ms of NiFe, with the same interlayer exchange strength J, NiFeCu feels a larger Hex, leading to a greater shift in optical mode frequency.

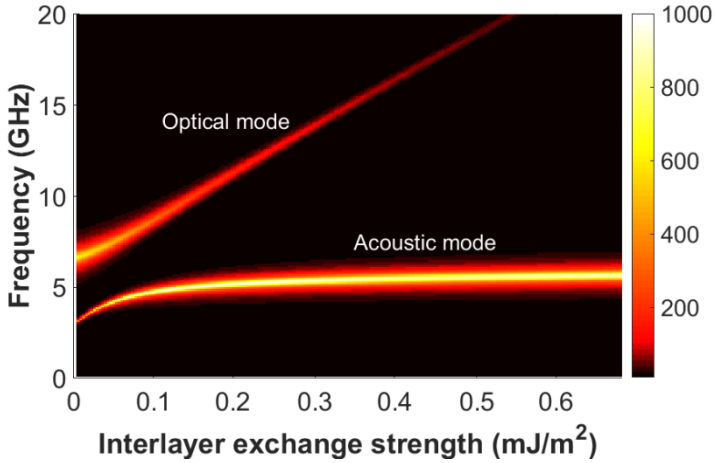

Figure 7.7 The frequency as a function of the interlayer exchange strength in 5nm CoFe/ 5nm NiFeCu bilayer. Color bar indicates the intensity of oscillation of each mode.

## 7.3 Experimental Results of Magnetic Resonance Modes in Bilayer System

### 7.3.1 The Acoustic and Optical Modes in CoFe/Nife Bilayer

Both acoustic and optical modes can be observed in $Co_{90}Fe_{10}/Ni_{80}Fe_{20}$ bilayers. The saturation magnetization of $Co_{90}Fe_{10}$ and $Ni_{80}Fe_{20}$ are 1.8 T and 0.9 T respectively. The exchange coupling strength between CoFe and NiFe is also strong when they are directly contacted with each other. The frequency of optical mode is higher than our measurement capability. To observe the optical mode, we deposited a dust layer of nonmagnetic material in between two magnetic layers, which effectively reduces the exchange coupling strength. Here we studied magnetic bilayer separated by a Ta spacer layer: Cu(2)/$Co_{90}Fe_{10}$(30)/Ta(1)/$Ni_{80}Fe_{20}$(30)/Ta(5) (the numbers in parentheses are thicknesses in nanometers), labeled as Ta(1). The 1 nm Ta is a discontinuous spacer layer that reduces the direct contact area between the two magnetic layers and thus adjusts the interface coupling strength. We fabricated Cu(2)/$Co_{90}Fe_{10}$(30)/Ta(3)/$Ni_{80}Fe_{20}$(30)/Ta(5), labeled as Ta(3), as a control sample,

where the magnetization dynamics in the two magnetic layers are completely decoupled. The resonance modes are detected with flip-chip field-swept FMR spectroscopy. As shown in Figure 7.8, the control sample Ta(3) shows two resonance peaks in the effective susceptibility spectra at 8 GHz, corresponding to the resonance of $Co_{90}Fe_{10}$ and $Ni_{80}Fe_{20}$ layers, respectively. The Ta(1) sample has a weak ferromagnetic coupling between the two magnetic layers and thus shows acoustic and optical modes that are significantly different from the individual resonance modes of the control sample.

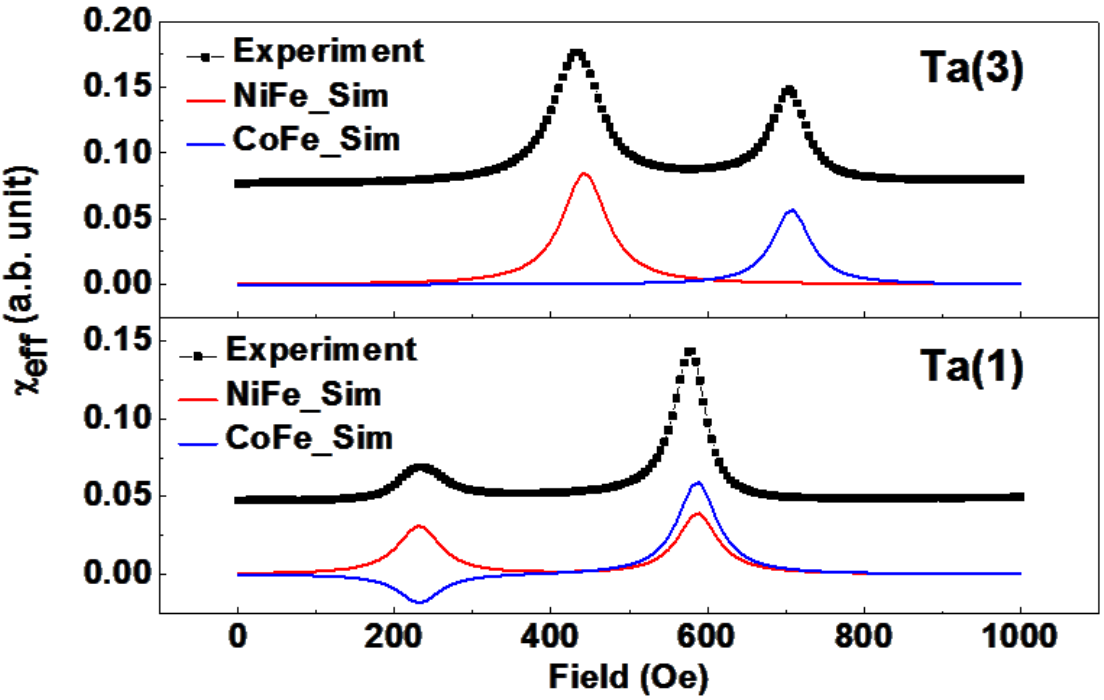


Figure 7.8 Observation of the acoustic modes and optical modes in CoFe/NiFe bilayer. The ferromagnetic resonance susceptibility spectra measured at 8 GHz of the Ta(3): Cu(2)/$Co_{90}Fe_{10}$(30)/Ta(3)/$Ni_{80}Fe_{20}$(30)/Ta (5) (top panel) and Ta(1): Cu(2)/$Co_{90}Fe_{10}$(30)/Ta(1)/$Ni_{80}Fe_{20}$(30)/Ta(5) (bottom panel) are shown in black curves. The red and blue curves are the simulated curves based on our model for $Ni_{80}Fe_{20}$ and $Co_{90}Fe_{10}$ layer, respectively. In the Ta (3) sample where the interlayer coupling is negligible, the two magnetic layers precess independently of each other. In

the Ta (1) sample with interlayer coupling, the two resonance modes shifted resulting in a high field (low frequency) acoustic mode and a low field (high frequency) optical mode. The parameters are used for simulating the resonance modes of both samples: $M_{s\_NiFe} = 0.9T$, $M_{s\_CoFe} = 1.8T$, $\alpha_{\mathrm{NiFe}} = 0.01$ and $\alpha_{\mathbf{CoFe}} = 0.012$. The extracted interlayer exchange coupling is $1.7\times10^{-4}$ J/m$^2$.

### 7.3.2 The Acoustic and Optical Mode in CoFe/NiFeCu Bilayer

Though we can observe the high-frequency optical mode in CoFe/NiFe, the optical mode is much weaker than the acoustic mode, because the total magnetization precession responding to a uniform microwave averages out due to the out-of-phase precession at optic mode. Therefore, the tiny optic mode is completely not applicable in anywhere that requires moderate microwave response. To efficiently excite the optical mode in a magnetic bilayer with a uniform microwave magnetic field, it is crucial to induce an asymmetry in the bilayer by using dissimilar magnetic films. As we discussed in Section 7.2, such magnetic bilayer can be designed with a magnetic layer FM1 with low saturation magnetization, and another magnetic layer FM2 with high saturation magnetization. The resultant magnetic bilayers will have a high resonance frequency that arises from the exchange interaction at the FM1/FM2 interface and a high effective susceptibility that arises from the high saturation magnetization in FM2.

Fe, Ni, and Cu are all miscible and form alloys at room temperature [19]. The saturation magnetization of $Ni_{80}Fe_{20}$ (permalloy) decreases when it alloys with Cu. The damping of NiFeCu alloy is weakly affected by Cu addition. This unique property is very useful in this study. The NiFeCu films were deposited by co-sputtering of $Ni_{80}Fe_{20}$ and Cu targets, and the composition is controlled by controlling the relative sputtering rate of $Ni_{80}Fe_{20}$ and Cu targets. The saturation magnetization and damping

of NiFeCu alloy film with different compositions measured by FMR are listed in Table 7.1.

**Table 7.1 The saturation magnetization and damping constant of various NiFeCu alloys**

| Sample composition | Ms(T) | damping |
|---|---|---|
| Ni80Fe20Cu0 | 0.9 | 0.009 |
| Ni70Fe18Cu12 | 0.78 | 0.015 |
| Ni63Fe16Cu21 | 0.66 | 0.016 |
| Ni57Fe14Cu29 | 0.54 | 0.019 |
| Ni52Fe13Cu35 | 0.40 | 0.016 |
| Ni43Fe10Cu47 | 0.35 | 0.019 |

To determine the exchange stiffness constant, we performed two measurements. First, we measure the temperature dependence of magnetization from which we can extract the exchange stiffness. At the temperature range much lower than the Curie temperature, the temperature dependence of magnetization is described by the Bloch $T^{3/2}$ power law [20]:

$$\Delta M / M_0 = (0.0587/v)(k_B T / 2 < S > J)^{3/2} \tag{7.16}$$

where the $\Delta M$ and $M_0$ are the change of magnetization due to temperature and magnetization at 0 K, respectively, $v$ is the number of atoms in a unit cell, $k_B$ is the Boltzmann constant, $T$ is temperature, $< S >$ is the average spin at one lattice, $J$ is the exchange energy. The exchange stiffness constant can be calculated by

$$A_{ex} = \frac{vJ < S >^2}{a} \tag{7.17}$$

where $a$ is the lattice constant which is determined by X-ray diffraction.

X-ray diffraction (XRD) measurements were performed using Rigaku Ultima IV X-ray diffractometer with CuK$\alpha$ source. Figure 7.9 shows the XRD patterns

of $Ni_{80}Fe_{20}$, $Ni_{43}Fe_{10}Cu_{47}$ and $Co_{90}Fe_{10}$ thin films with thickness of 40nm. In the XRD patterns of NiFe and NiFeCu, the (111) peak is observed, indicating a face-centered cubic (fcc) structure. For CoFe, the (110) peak at 44.6° is present, revealing a body-centered cubic (bcc) structure. The values of lattice constants are extracted from Eq. (3.1) as 0.361 nm, 0.363 nm, 0.290 nm for the NiFe, NiFeCu and CoFe thin film, respectively.

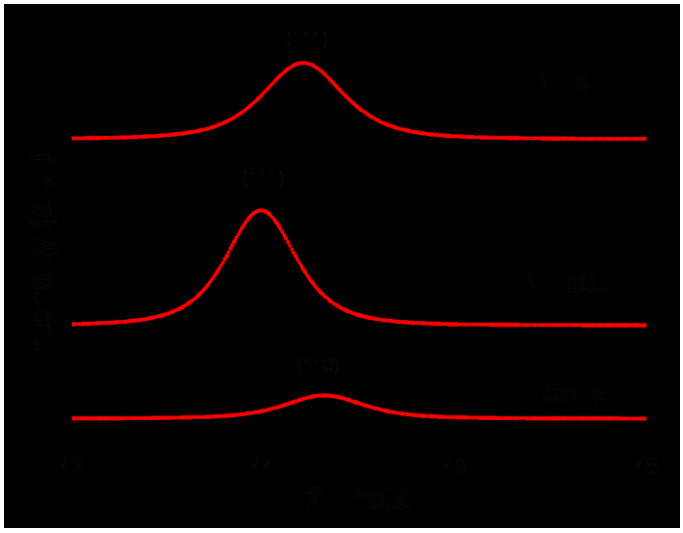

Figure 7.9 X-ray diffraction pattern of NiFe, NiFeCu and CoFe. The read lines are the fitting of the X-ray pattern.

Figure 7.10 presents the magnetization-temperature curve of NiFe, NiFeCu, and CoFe thin films from 50 K to 210 K. As expected, the temperature dependence of the magnetization follows Bloch $T^{3/2}$ power law. The extracted exchange stiffness from Eq. (7.16) are $(1.2\pm0.1)\times10^{-11}$ J/m, $(0.20\pm0.01)\times10^{-11}$ J/m, and $(2.5\pm0.2)\times10^{-11}$ J/m for NiFe, NiFeCu and CoFe, respectively.

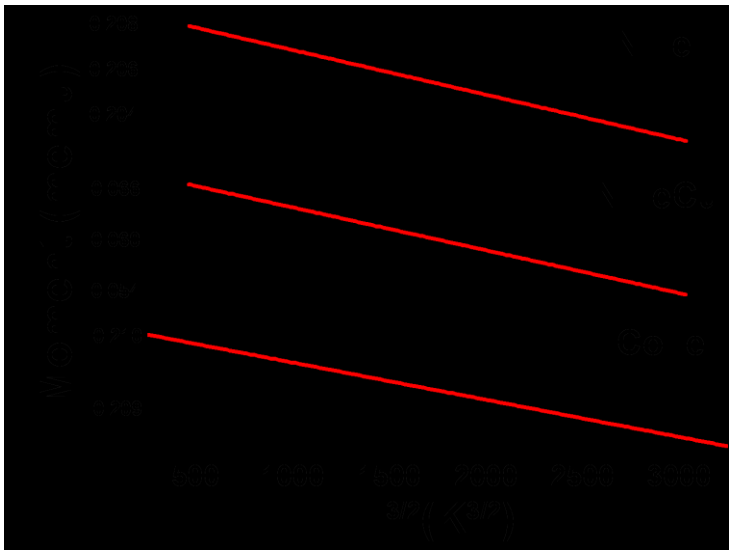

Figure 7.10 Temperature dependence of the magnetization in between 50 K and 210 K.

Figure 7.11 (a) shows the simulated magnetization precession profiles of acoustic mode and an optical mode in a bilayer composed of a week magnetic $Ni_{43}Fe_{10}Cu_{47}$ and a strong magnetic $Co_{90}Fe_{10}$. For the optical mode, the precession profile is quasi-antisymmetric, arising from the asymmetric bilayer. Since the saturation magnetization is low in NiFeCu, the effective susceptibility is dominated by the high saturation magnetization of CoFe. By summing over the precession across the entire film, the calculated effective susceptibility at 14 GHz of both optical and acoustic modes is shown in Figure 7.11 (b). The parameters used in simulation are: $M_{s\_CoFe}$=1.8 T, $M_{s\_NiFeCu}$=0.36 T, exchange stiffness $A_{CoFe}=2.5\times10^{-11}$ J/m, $A_{NiFeCu}=3.5\times10^{-12}$ J/m, interlayer exchange energy $J_{int}=4.2\times10^{-4}$ J/m$^2$. The exchange stiffness of CoFe ($2.5\times10^{-11}$ J/m) and NiFeCu ($0.2\times10^{-11}$ J/m) are determined from the temperature dependence of the saturation magnetization. To get the best fit, a slightly larger value of $3.5\times10^{-12}$ J/m for NiFeCu is used in the simulation. These parameters are consistent with reported values [19, 21]. Experimentally, the effective susceptibility is extracted from the microwave transmission loss[22],

as $\chi_{eff} = ia \log \frac{S_{21}}{S_{21\_ref}}$, where $S_{21}$ is the microwave transmission and $S_{21\_ref}$ is the $S_{21}$ measured at saturation field. The pre-factor $a$ is related to the sample geometry, fixture geometry, and frequency. Since the samples under test have identical lateral geometry and are measured in the same fixture, we neglect the pre-factor in this comparison. The experimental result agrees very well with the simulation. The total effective susceptibility of the optical mode is 40% of the FMR of the single CoFe layer. This is much larger than the susceptibility of the optical mode for $Co_{90}Fe_{10}/Ni_{80}Fe_{20}$ bilayer which is only 10% of the susceptibility of the single CoFe layer at FMR. Figure 7.11 (c) shows the resonant field as a function of the resonant frequency for single $Co_{90}Fe_{10}$ film and $Co_{90}Fe_{10}/Ni_{43}Fe_{10}Cu_{47}$ bilayer. At 14 GHz, the resonant field for the optical mode is 110 mT lower than that for the FMR of the single $Co_{90}Fe_{10}$ film. The enhancement of resonance frequency is 9 GHz in a constant 20 mT external field, due to the equivalent 110 mT exchange field from the interface. The tunable range here is limited by our FMR measurement setup, which is far from the theoretical limit of our approach. Due to its substantial susceptibility, the optical mode can be used in conventional microwave devices that based on FMR, such as microwave isolators and filters.

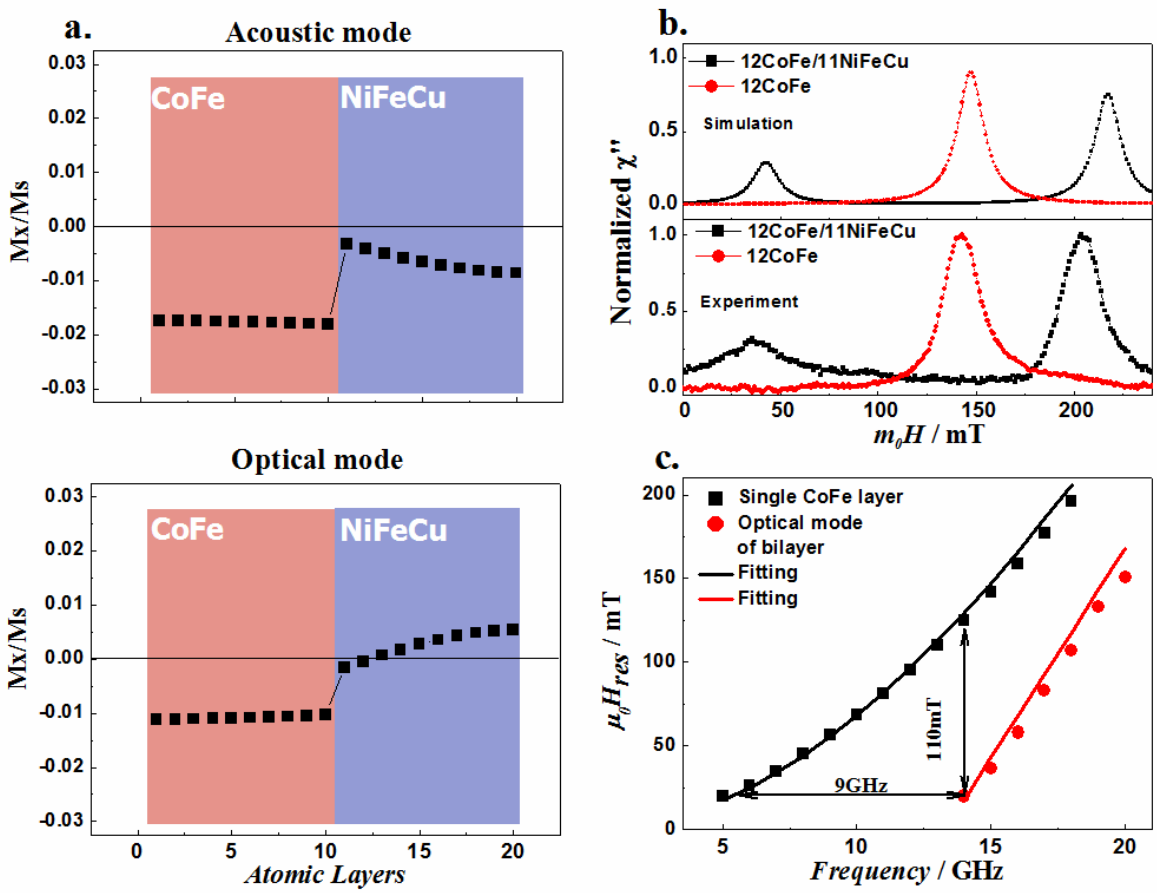


Figure 7.11 Magnetic resonance modes under uniform excitation. (a) Distribution of magnetization precessions in the bilayer at acoustic mode and optical mode. (b) Simulated and experimental measured effective susceptibility for $Co_{90}Fe_{10}$ (12 nm) and $Co_{90}Fe_{10}$ (12 nm)/$Ni_{43}Fe_{10}Cu_{47}$ (11 nm) at 14 GHz. (c) Comparison of resonance frequency and field between FMR mode of single CoFe and optical mode of the bilayer. The dots are experimental data, and the lines are from the simulation.

## 7.4 Application of Tunable Magnetic Resonance in Spintronic Devices

One immediate application is in emerging spintronics microwave devices which also demands high operating resonance frequency of the magnetic layer [23-26]. Although the magnetization precessions of the two magnetic layers are out-of-phase at the optical mode, it is still suitable for the application of spintronics microwave

devices, because only the ferromagnetic layer near the nonmagnetic/insulator interface governs the performance of the devices [27]. Therefore, when an exchange-coupled bilayer is used in the spintronics microwave device, the sensitivity will not suffer from the reduced effective susceptibility due to the antisymmetric distribution of magnetization precession in optical mode.

### 7.4.1 Rectifying Effect in Spin Valves and Interface Effect

The top panel of Figure 7.12 (a) illustrates the configuration of the spin valve stripe with the single free layer as part of the CPW centerline. An RF current, $I_{rf} = I_0 \cos(\omega t)$, flows in the *z*-direction, which generates transverse RF magnetic field $H_{rf}$ in the *y*-direction. The magnetization of the reference layer in SV is fixed at the *x*-direction. The $H_{rf}$ excites the precession of the magnetization and alters the magnetization angles between the free layer and reference layer as $\theta(t) = \phi + \theta_0 \cos(\omega t - \varphi)$, where $\phi$ is the initially set to be 90°, $\theta_0 \approx \frac{m_x}{M_s}$ is the precession angle, and $\varphi$ is the phase difference between magnetization precession and RF current. $m_x$ is the *x* component of magnetization and $M_s$ is the saturation magnetization. The resistance of the structure oscillates due to the giant magnetoresistance effect (GMR) as

$$R(t) = R_P + 1/2\Delta R[1 - \cos(\theta)] \tag{7.18}$$

where $R_P$ is the resistance at the parallel state, and $\Delta R$ is the resistance difference between parallel and antiparallel states.

The DC voltage on the SV can then be calculated from the average product of the RF current and resistance. The expression is written as

$$V_{\mathrm{dc}} = \int I_{rf}(t) \times R(t) dt = \frac{1}{4} \left\langle I_{\mathrm{rf}} \Delta R \frac{m_{\mathrm{x}}}{M_{\mathrm{s}}} \right\rangle \sin\phi \tag{7.19}$$

Although the free layer of the SV is made of a magnetic bilayer, the DC voltage only depends on the magnetization precession of the layer close to Cu spacer layer. Therefore the magnetization in Eq. (7.16) is attributed to the free layer near the 3nm Cu layer. This property of SV rectification effect can be examined by purposely reversing the layer sequence of the free layers. We tested two SV samples with stack structures as CoFe(6)/ Ta(1.5)/ NiFe(6)/ Cu(3)/ CoFe(4)/ IrMn(15) (sample I) and NiFe(6)/ Ta(1.5)/ CoFe(6)/ Cu(3)/ CoFe(4)/ IrMn(15) (sample II). The measured rectified voltage as a function of the magnetic field is plotted in Figure 7.12 (b). The red and blue arrows in the graph indicate the precession states of NiFe and CoFe, respectively. Comparing the precession phase between acoustic mode and optical mode, the phase of CoFe is the same, but NiFe shows 180° phase difference. In sample I where NiFe is near the Cu spacer, the acoustic mode, and optical mode are out of phase because the rectification voltage is corresponding to the precession in NiFe; while, for sample II, the acoustic mode and optical mode are in phase which matches the precession of CoFe.

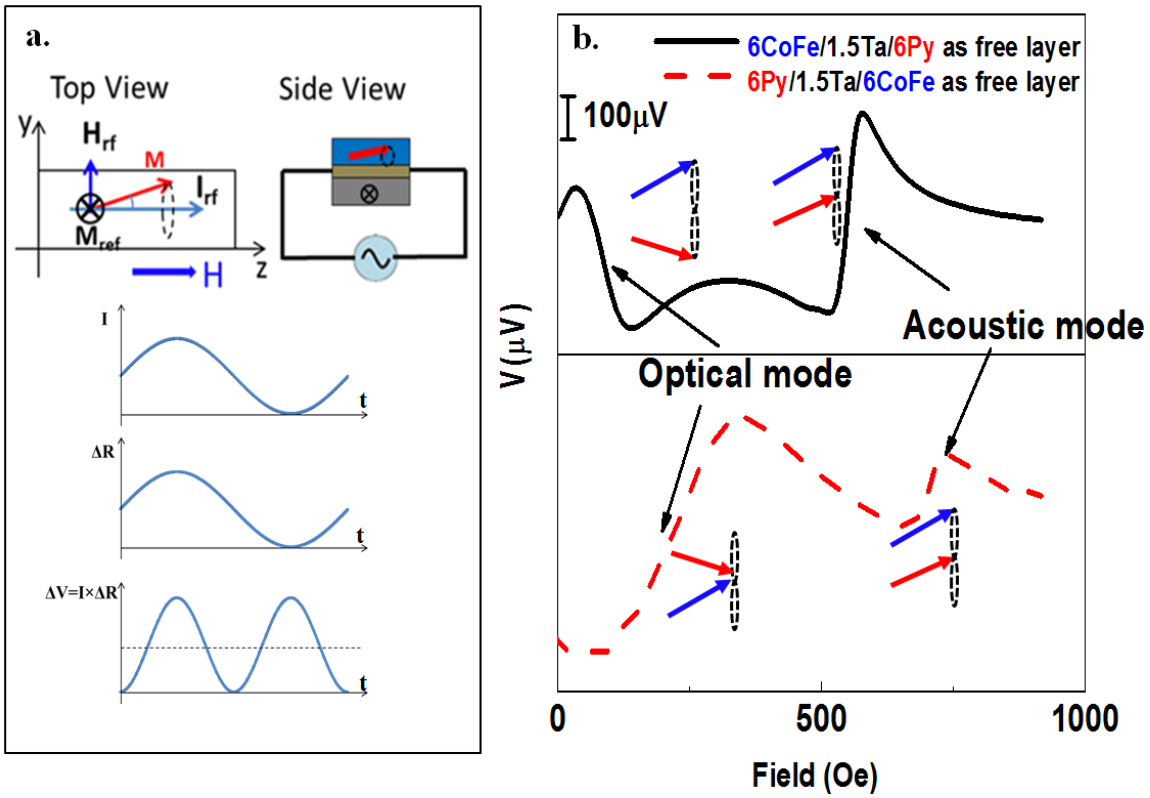


Figure 7.12 Spintronic rectification effect and interface effect. (a) Illustration of the spin valve rectification effect. (b) Measured rectified voltage as a function of the external magnetic field. The black solid curve is for the sample with CoFe(6)/Ta(1.5)/NiFe(6) as the free layer and the red dashed curve is for the sample with NiFe(6)/Ta(1.5)/CoFe(6) as the free layer, where the second layer is the sensor layer next to Cu. The blue and red arrows indicate the magnetic moments in CoFe and NiFe (Py), respectively.

### 7.4.2 Giant Tunability of Magnetic Resonance by Controlling of the Film Thickness

To efficiently tune the resonance frequency of the optical mode, one can adjust the interlayer exchange coupling *J* by engineering the interface. Tantalum (Ta) spacer layer was deposited in between two FM layers. The interlayer exchange coupling can be adjusted by the thickness of the Ta layer. We developed a spin valve (SV) based microwave detector to demonstrate the effect of the optical mode in the microwave detections. As shown in Figure 7.13 (a), the SV is patterned as a part of the

coplanar waveguide (CPW). A microwave is fed into the CPW through a bias tee. A voltmeter measures the rectified DC voltage at the DC branch of the bias tee. The inset shows the SV structure, which has the free layer aligned along the *z*-direction by an external field of 50 Oe and the reference layer is pinned along the *x*-direction. The detector is a strip of the spin valve (SV), in which the free magnetic layer is composed of exchange coupled ferromagnetic bilayer with a nonmagnetic layer of varying thickness in between to tune the strength of exchange coupling. The structure of the SV is Cu (2nm)/$Co_{10}Fe_{90}$ (4nm)/Ta (0.4-2.0nm)/$Ni_{80}Fe_{20}$ (4nm)/ Cu(3nm) /$Co_{10}Fe_{90}$ (4nm) /IrMn (15nm)/Ta (5nm). The microwave magnetic field excites the acoustic mode as well as the optical mode in the bilayer. The precession of the magnetization in the bilayer results in a SV with alternating resistance that rectifies the microwave field and generates a DC voltage as Eq. (7.19). The DC voltage is proportional to the microwave power and attains a maximum value at the acoustic mode and the optical mode resonances. The measured voltage peaks corresponding to the acoustic mode and the optical mode with opposite phase are shown in Figure 7.13 (b). By varying the thickness of the Ta spacer layer, the resonance frequency due to the optical mode can be shifted from 5 GHz to 25 GHz as shown in Figure 7.13 (c). The corresponding effective field change is 4000 Oe. The magnitude of the resonance peaks inversely scale with the resonance frequency following the nature of magnetic resonance, as shown in the inset of Figure 7.13 (c).

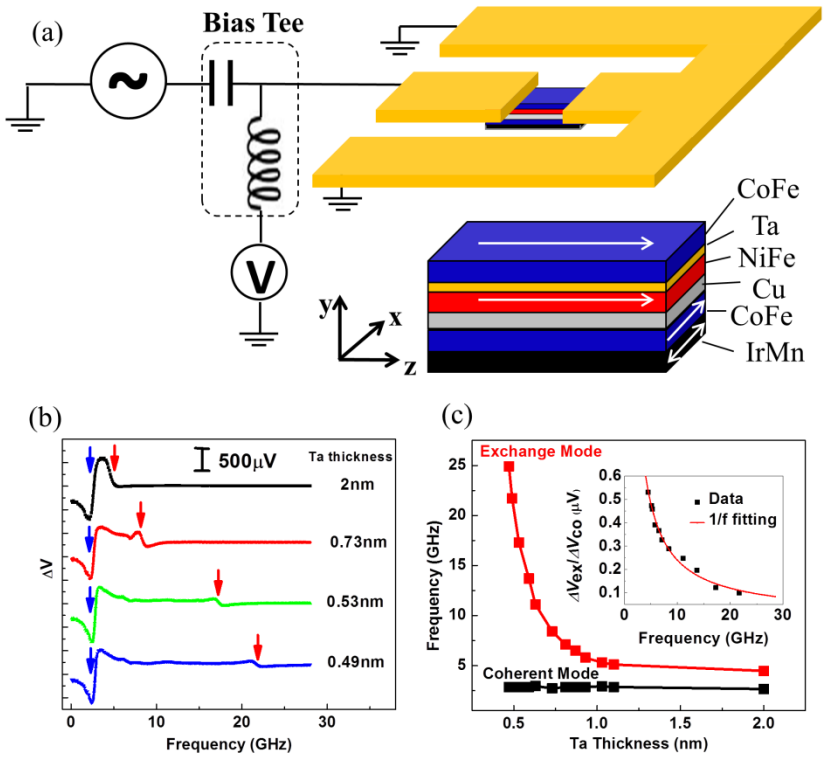


Figure 7.13 (a) Experimental setup of the spin valve-based microwave detector. (b) Rectified voltage response to the microwave input at various frequencies. (c) Optical mode and acoustic mode frequencies with respect to Ta thickness. The inset shows that voltage sensitivity is inversely proportional to the frequency. Here the acoustic mode is used to calibrate the input microwave power.

### 7.4.3 In-Situ Thermal Tuning of Magnetic Resonance Frequency

The in-situ tuning of FMR, through temperature or electric field, is highly desirable in applications. Our idea is to replace the Ta spacer layer by materials with temperature or electric field induced phase transition. For temperature control, some materials, such as NiCu alloys and Gd, show a ferromagnetic to paramagnetic phase transition around room temperature. We realize an in-situ tuning of the exchange coupling by deploying the magnetic phase transition of $Ni_xCu_{1-x}$ alloys. In the

demonstration, a $Co_{90}Fe_{10}/Ni_{40}Cu_{60}/Ni_{80}Fe_{20}$ trilayer is used to replace the single ferromagnetic sensing layer in a SV. The NiCu has a Curie temperature slightly above room temperature. In the trilayer, the temperature can serve as a convenient tool to adjust the effective exchange coupling between CoFe and NiFe layers.

The Curie temperature of $Ni_xCu_{1-x}$ alloy can be controlled by changing the composition. $Ni_{70}Cu_{30}$ alloys have a Curie temperature at 273K. However, as the $Ni_xCu_{1-x}$ layer is deposited next to a strong ferromagnetic layer, its Curie temperature becomes higher due to the proximity effect [28]. We investigated the temperature dependence of the interlayer exchange coupling by measuring the magnetization hysteresis of NiFe (4)/$Ni_{40}Cu_{60}$ (10 or 4)/CoFe (4)/IrMn (15)/Ta (5). Two strong FM layers, NiFe, and CoFe are coupled through the weak ferromagnetic NiCu layer. The magnetization of the CoFe layer is fixed by the antiferromagnetic IrMn layer. The magnetic hysteresis loop was measured by a vibrating sample magnetometer (VSM) at a temperature from 273 K to 330 K. When the two FM layers are strongly coupled with each other, their magnetizations switch at the same field. In Figure 7.14 (a), the black (300 K) and red (323 K) curves have shown only one switching, indicating strong interlayer exchange coupling. When the temperature is increased to 330 K, two separate switchings appear in the hysteresis loop, suggesting the two FM layers are decoupled. The exchange coupling is reduced as the temperature increases. Moreover, the coercivity of CoFe increases with temperature, which also signifies the reduction of interlayer exchange coupling. In the other sample with a thinner NiCu spacer, shown in Figure 7.14 (b), only one switching can be observed throughout the temperatures because the interlayer exchange coupling is stronger due to the thinner

spacer layer. The slightly increased coercivity indicates the reduction of exchange coupling with the rise of temperature.

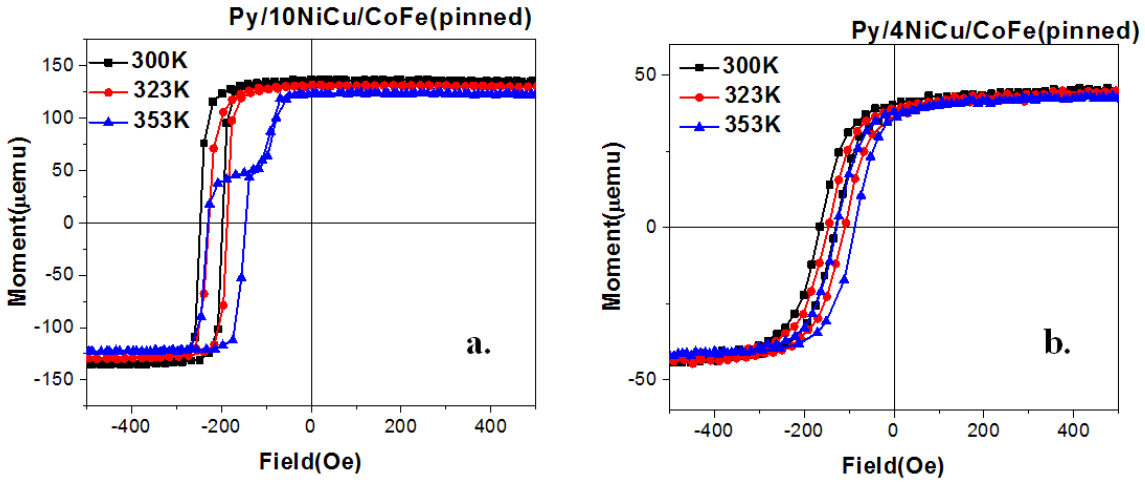


Figure 7.14 Magnetic hysteresis loops at several temperatures for samples of (a) NiFe (4nm)/NiCu (10mm)/CoFe (4nm)/IrMn (15nm)/Ta (5nm) and (b) NiFe (4nm) /NiCu (10nm)/ CoFe (4nm)/IrMn (15nm) /Ta (5nm).

In real device demonstration, a free layer composed of $Ni_{80}Fe_{20}$ (4nm)/$Ni_{40}Cu_{60}$ (4nm)/$Co_{90}Fe_{10}$ (4nm) is used to replace the free layers of the SV in Figure 7.13 (a). The whole stack of the SV is Ta(10nm)/ IrMn(15nm)/ $Co_{90}Fe_{10}$(4nm)/ Cu(3nm)/ $Ni_{80}Fe_{20}$(4nm)/ $Ni_{40}Cu_{60}$(4nm)/ $Co_{90}Fe_{10}$(4nm)/ Ta(5nm), depicted in Figure 7.15(a). Because of the precession in the NiFe layer, the resistance of the SV varies due to the giant magnetoresistance effect and rectifies with the microwave current to generate a DC voltage following Eq. (7.19).

Figure 7.15 (b) shows two voltage resonances, which have opposite phases, corresponding to the acoustic and optical modes, respectively. When the temperature changes from 263 K to 358 K, the resonance frequency of the acoustic mode does not alter while that of the optical mode shifts from 21 GHz to 11 GHz, suggesting a change in the strength of the interlayer exchange coupling. It should be noted that the

changes in the magnetic properties of individual CoFe and NiFe layers are negligible in this temperature range. The reduction of the voltage at the acoustic mode and the emerging broad resonance near 8 GHz (the insert in Figure 7.15 (b)) with increasing temperature suggest the reduction of the antiferromagnetic coupling in the pinned layer. It is estimated in Figure 7.14 (c) that the effective interlayer exchange coupling changes from $1.28\times10^{-3}$ J/m$^2$ to $0.35\times10^{-3}$ J/m$^2$ from 263 K to 358K. It is important to notice that the 1/f frequency dependence of the voltage response in the optical mode is only caused by the nature of FMR, reduction of susceptibility following 1/f dependence. Therefore, the sensitivity of the device is not reduced by the quasi-antisymmetric distribution of magnetic precession at optical mode. It is also worth pointing out that the damping of the spacer layer (NiCu layer) in this application is not crucial, which is a technical advantage for the selection of the intermediate material to *in-situ* tune the interlayer exchange coupling.

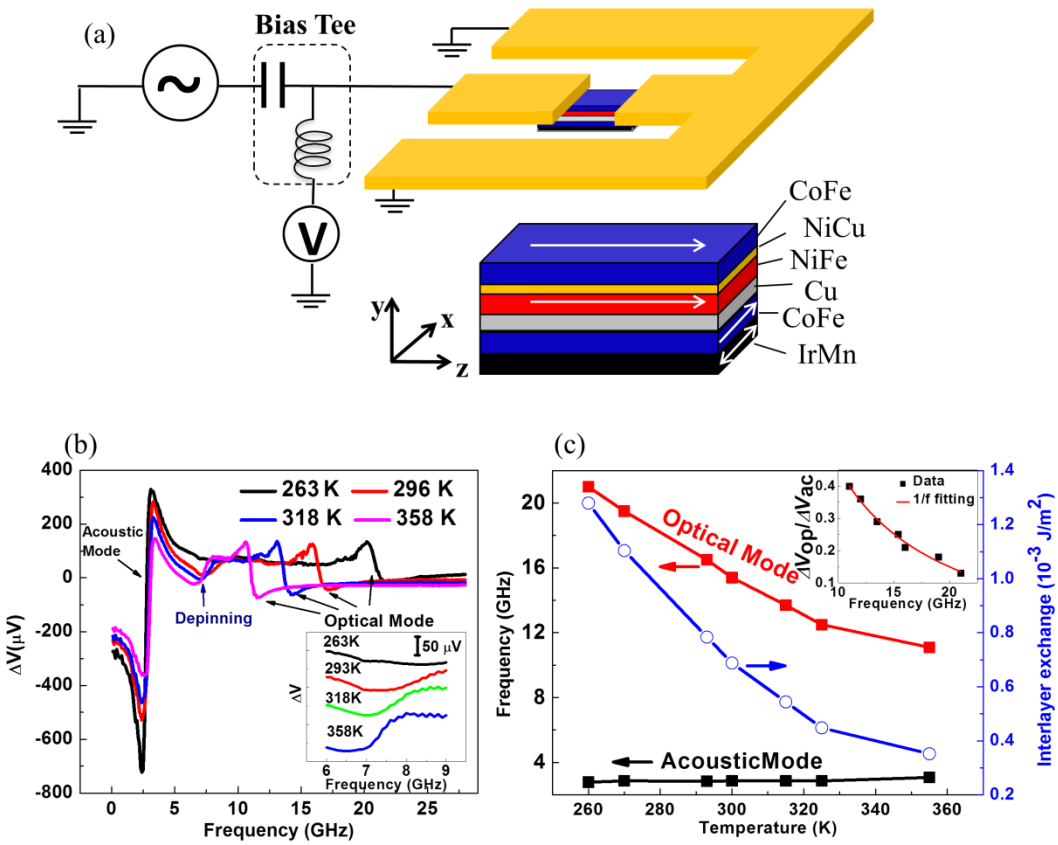


Figure 7.15 Magnetic resonance modes in spin valves. (a) Illustration of the spin valve-based microwave detector. (b) The SV responses at different temperatures. (c) The resonant frequency for acoustic and optical modes and extracted interlayer coupling strength as a function of the temperature. The parameters used for simulation are $\mu_0 M_{NiFe} = 1T, A_{NiFe} = 1.2\times10^{-11} J/m, \mu_0 M_{CoFe} = 1.8T, A_{CoFe} = 2.5\times10^{-11} J/m$. The inset shows that the voltage sensitivity is inversely proportional to the frequency. Here the acoustic mode is used to calibrate the input microwave power which is unknown due to the variation of device impedance at different frequencies, and the ratio between the acoustic mode voltage $\Delta V_{ac}$ and optical mode voltage $\Delta V_{op}$ is used to show the $1/f$ dependence (red curve).

The magnetization direction of the reference layer is fixed along the *x*-direction, which is parallel to the microwave magnetic field. In this case, the precession of the reference layer cannot be excited. However, a misalignment of the reference magnetization will introduce an additional peak in rectifying measurement shown in Figure 7.15 (b). The voltage peak due to the reference layer can be

distinguished by measuring the rectified voltage spectra in various external static magnetic fields in the *x*-direction that reduces the misalignment. Figure 7.16 (a) shows the SV response to microwaves of 0 dBm intensity. The essential structure of the SV microwave detector is CoFe (6)/Ta (0.5)/NiFe (6)/Cu(3)/CoFe (4)/IrMn (15)/Ta (5). The voltage peaks around 3 GHz correspond to the acoustic mode of the free layers and the peaks around 9 GHz correspond to the resonance of the reference layer. The inset is the magnified view of the resonance mode of the reference layer. The magnitude of the acoustic mode increases when the external field is tuned from -13.5 mT to 5 mT, while the peak due to the reference layer reduces. In 5 mT bias field, the peak due to the reference layer vanishes, indicating the relative angle between the free layer and the reference layer, $\phi$, is near 90°. The pinning field in the *x*-direction $H_{\perp}$ is measured to be 25 mT (Figure 7.16 (a)).By changing the external magnetic field, the relative angle can be tuned as

$$\phi = \arctan\left(\frac{\mu_0 H_{\perp}}{\mu_0 H_{ex} - 5}\right) \tag{7.17}$$

Base on Eq. (7.16), the rectified voltage of the acoustic mode is proportional to $\sin\phi$ and the voltage due to the resonance of the reference layer is proportional to $\cos\phi$. This is confirmed by the experimental data shown in Figure 7.16 (b).

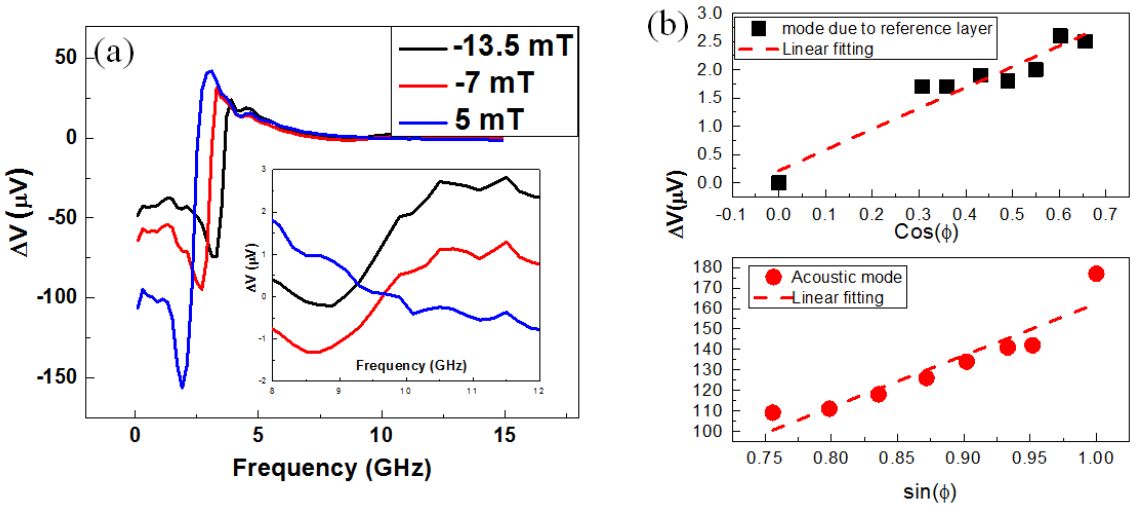


Figure 7.16 The additional peak due to the precession of the reference layer. (a) The voltage response of spin valves as a function of the frequency in an external field of -13.5mT, -7mT, and 5mT. To compensate the magnetization misalignment of the reference layer, the external magnetic field is applied in the z-direction from -13.5 mT to 5 mT. When the field equals to 5 mT, the magnetization of the reference layer is aligned exactly perpendicular to that of the free layer. The mode due to the reference layer is absent, and the acoustic mode is at its maximum response. (b) The magnitude of FMR modes as a function of the relative angle. The mode of the reference layer is linear with $\cos\phi$, and the acoustic mode is linear with $\sin\phi$.

We used the analytical model developed in Section 7.2 to simulate the magnetic resonance in magnetic trilayer consisting of NiFe(4)/NiCu(4)/CoFe(4), the middle layer NiCu near its magnetic phase transition was modeled as a tunable interfacial exchange interaction. However, the NiCu layer should be treated as a third magnetic layer in the dynamic process. Here we show the comparison between the bilayer model and trilayer model. The parameters we chose for the simulation is as follows: $M_{s\_NiFe} = 0.9T$, $\alpha_{\mathbf{NiFe}} = 0.01$, $A_{\mathbf{NiFe}} = 1.2\times10^{-11} J/m$, $M_{s\_CoFe} = 1.8T$, $\alpha_{\mathbf{CoFe}} = 0.015$, $A_{\mathbf{CoFe}} = 2.5\times10^{-11} J/m$, $M_{s\_NiCu} = 0.2T$, $\alpha_{\mathbf{NiCu}} = 0.01$, $A_{\mathbf{NiCu}} = 2.0\times10^{-12} J/m$, $H_{ext} = 50Oe$.

We assume the interlayer exchange coupling strength is as strong as the interlayer exchange coupling strength for CoFe/NiFeCu bilayer

$J_{\text{NiFe\_NiCu}} = J_{\text{CoFe\_NiCu}} = 5.7 \times 10^{-3} J/m^2$. For simplicity, we neglect the anisotropy of all layers. For bilayer simulation, the NiCu layer is simply treated as an interface with an interface exchange coupling strength of $J_{\text{NiFe\_NiCu\_CoFe}} = 4.2 \times 10^{-4} J/m^2$. The simulated results are shown in Figure 7.17. Both of the effective susceptibility and the precession pattern have a similar profile in NiFe and CoFe layer. This suggests that it is reasonable to effectively treat the NiCu layer as an interface. The changes in the saturation magnetization, intralayer exchange interaction, and the interlayer exchange interaction can be treated as an effective interlayer exchange interaction. This simplification is valid because of two reasons: (1) it is the CoFe or NiFe layer that is of particular interest to the applications in spintronics microwave devices; and (2) the NiCu layer has very small saturation magnetization and exchange interaction such that the resonance modes are predominantly determined by the CoFe and NiFe layers. It is also found that the damping in NiCu does not play a significant role in the precession modes. Shown in Figure 7.18, the amplitude of the optical mode in NiFe is sensitive to the damping of NiFe and CoFe but varies slowly with the damping of NiCu. This is also because of the low saturation magnetization in NiCu. Damping serves as an energy dissipation channel that balances with the pumping energy from microwaves and maintains the equilibrium state of precession. Most of the energy are dissipated in NiFe and CoFe because of their large saturation magnetization. Therefore, a small change of damping in NiCu does not significantly affect the overall damping of the system and, therefore, does not render significant perturbation on the precession. This is practically useful because it is not common for a magnetic material to maintain a small damping near its phase transition. The trilayer system has much tolerance on the damping of this spacer layer that makes the choice of materials more flexible.

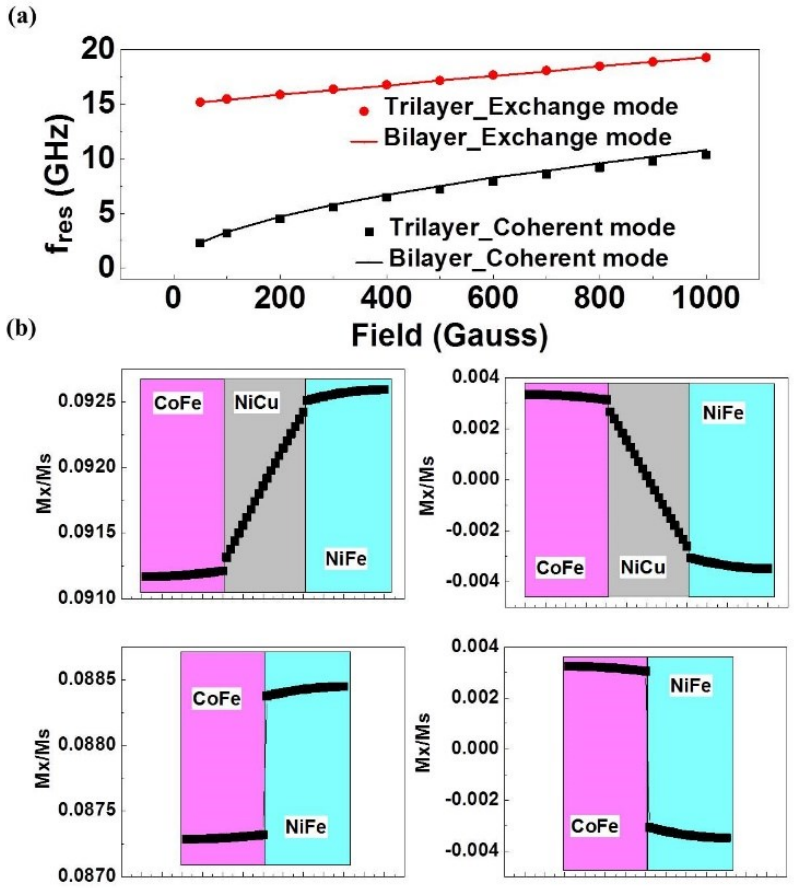


Figure 7.17 Comparison between trilayer simulation and bilayer simulation. (a) Simulated resonance frequencies at various fields using trilayer model and bilayer model. The bilayer model agrees well with the trilayer model using one single parameter $J_{\text{NiFe\_NiCu\_CoFe}} = 4.2\times10^{-4} J/m^2$. (b) Trace of precession angle across the entire sample for the acoustic modes (left two graphs) and the optical modes (right two graphs).

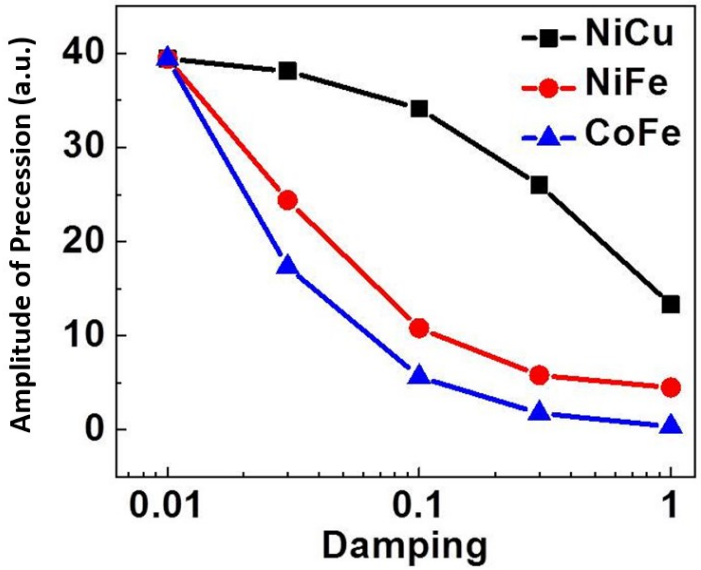


Figure 7.18 The amplitude of the optical mode in NiFe as a function of the damping constant in each layer. When changing the damping in one layer, the damping constant of the other two layers is fixed at 0.01.

## REFERENCES


[1] C. Kittel, "On the theory of ferromagnetic resonance absorption," *Physical Review,* vol. 73, p. 155, 1948.

[2] B. Heinrich, K. Urquhart, A. Arrott, J. Cochran, K. Myrtle, and S. Purcell, "Ferromagnetic-resonance study of ultrathin bcc Fe (100) films grown epitaxially on fcc Ag (100) substrates," *Physical review letters,* vol. 59, p. 1756, 1987.

[3] N. Cramer, D. Lucic, R. Camley, and Z. Celinski, "High attenuation tunable microwave notch filters utilizing ferromagnetic resonance," *Journal of Applied Physics,* vol. 87, pp. 6911-6913, 2000.

[4] M. Pardavi-Horvath, "Microwave applications of soft ferrites," *Journal of Magnetism and Magnetic Materials,* vol. 215, pp. 171-183, 2000.

[5] M. Darques, J. De la Torre Medina, L. Piraux, L. Cagnon, and I. Huynen, "Microwave circulator based on ferromagnetic nanowires in an alumina template," *Nanotechnology,* vol. 21, p. 145208, 2010.

[6] O. Prokopenko, E. Bankowski, T. Meitzler, V. Tiberkevich, and A. Slavin, "Spin-torque nano-oscillator as a microwave signal source," *Magnetics Letters, IEEE,* vol. 2, pp. 3000104-3000104, 2011.

[7] X. Fan, R. Cao, T. Moriyama, W. Wang, H. Zhang, and J. Q. Xiao, "Magnetic tunnel junction based microwave detector," *Applied Physics Letters,* vol. 95, p. 122501, 2009.

[8] M. Farle, "Ferromagnetic resonance of ultrathin metallic layers," *Reports on Progress in Physics,* vol. 61, p. 755, 1998.

[9] N. A. Spaldin and M. Fiebig, "The renaissance of magnetoelectric multiferroics," *Science,* vol. 309, pp. 391-392, Jul 15 2005.

[10] N. Hur, S. Park, P. A. Sharma, J. S. Ahn, S. Guha, and S. W. Cheong, "Electric polarization reversal and memory in a multiferroic material induced by magnetic fields," *Nature,* vol. 429, pp. 392-395, May 27 2004.

[11] J. Lou, M. Liu, D. Reed, Y. Ren, and N. X. Sun, "Giant Electric Field Tuning of Magnetism in Novel Multiferroic FeGaB/Lead Zinc Niobate-Lead Titanate (PZN-PT) Heterostructures," *Advanced Materials,* vol. 21, p. 4711, Dec 11 2009.

[12] T. X. Nan, Z. Y. Zhou, J. Lou, M. Liu, X. Yang, Y. Gao*, et al.*, "Voltage impulse induced bistable magnetization switching in multiferroic heterostructures," *Applied Physics Letters,* vol. 100, Mar 26 2012.

[13] M. Liu, Z. Zhou, T. Nan, B. M. Howe, G. J. Brown, and N. X. Sun, "Voltage Tuning of Ferromagnetic Resonance with Bistable Magnetization Switching in Energy-Efficient Magnetoelectric Composites," *Advanced Materials,* vol. 25, pp. 1435-1439, Mar 13 2013.

[14] S. Ikeda, K. Miura, H. Yamamoto, K. Mizunuma, H. D. Gan, M. Endo*, et al.*, "A perpendicular-anisotropy CoFeB-MgO magnetic tunnel junction," *Nature Materials,* vol. 9, pp. 721-724, Sep 2010.

[15] W.-G. Wang, M. Li, S. Hageman, and C. L. Chien, "Electric-field-assisted switching in magnetic tunnel junctions," *Nature Materials,* vol. 11, pp. 64-68, Jan 2012.

[16] R. C. O'Handley, "Modern Magnetic Materials: Principles and Applications," p. chap. 3.7, 1999.

[17] A. Kurs, A. Karalis, R. Moffatt, J. D. Joannopoulos, P. Fisher, and M. Soljacic, "Wireless power transfer via strongly coupled magnetic resonances," *Science,* vol. 317, pp. 83-86, Jul 6 2007.

[18] O. Dmytriiev, T. Meitzler, E. Bankowski, A. Slavin, and V. Tiberkevich, "Spin wave excitations of a magnetic pillar with dipolar coupling between the layers," *Journal of Physics: Condensed Matter,* vol. 22, p. 136001, 2010.

[19] S. Mathias, C. La-O-Vorakiat, P. Grychtol, P. Granitzka, E. Turgut, J. M. Shaw*, et al.*, "Probing the timescale of the exchange interaction in a ferromagnetic alloy," *Proceedings of the National Academy of Sciences of the United States of America,* vol. 109, pp. 4792-4797, Mar 27 2012.

[20] C. J.M.D., *Magnetism and Magnetic Materials*: Cambridge University 2009.

[21] D. V. Berkov and N. L. Gorn, "Spin-torque driven magnetization dynamics in a nanocontact setup for low external fields: Numerical simulation study," *Physical Review B,* vol. 80, p. 064409, 08/14/ 2009.

[22] Y. P. Chen, X. Fan, Q. Lu, and J. Q. Xiao, "Damping dependence in microwave assisted magnetization reversal," *Journal of Applied Physics,* vol. 110, Sep 1 2011.

[23] X. Fan, R. Cao, T. Moriyama, W. Wang, H. W. Zhang, and J. Q. Xiao, "Magnetic tunnel junction based microwave detector," *Applied Physics Letters,* vol. 95, p. 3, Sep 2009.

[24] L. Fu, Z. X. Cao, S. Hemour, K. Wu, D. Houssameddine, W. Lu*, et al.*, "Microwave reflection imaging using a magnetic tunnel junction based spintronic microwave sensor," *Applied Physics Letters,* vol. 101, p. 4, Dec 2012.

[25] D. Houssameddine, U. Ebels, B. Delaet, B. Rodmacq, I. Firastrau, F. Ponthenier*, et al.*, "Spin-torque oscillator using a perpendicular polarizer and a planar free layer," *Nature Materials,* vol. 6, pp. 447-453, Jun 2007.

[26] J. Zhu, J. A. Katine, G. E. Rowlands, Y.-J. Chen, Z. Duan, J. G. Alzate*, et al.*, "Voltage-Induced Ferromagnetic Resonance in Magnetic Tunnel Junctions," *Physical Review Letters,* vol. 108, p. 197203, 05/09/ 2012.

[27] A. G. Gurevich, and G A. Melkov, *Magnetization Oscillations and Waves*: Boca Raton: CRC Press, 1996.

[28] S.-Y. Huang, X. Fan, D. Qu, Y. Chen, W. Wang, J. Wu*, et al.*, "Transport magnetic proximity effects in platinum," *Physical review letters,* vol. 109, p. 107204, 2012.

# APPENDIX

## A. NUMERICAL SIMULATION OF THE MAGNETIC DYNAMICS IN TIME DOMAIN

A code to solve LL equation in time domain was written in Mathematica as follow.

```
h={0,0,-10};(*external magnetic field)
f0=2*10^9;(*microwave frequency)
hrf=10;(*amplitude of microwave field*)
g=28*10^5*2Pi; (*gyromagnetic ratio*)
Ms=15000;(*saturation magnetization*)
damping=0.02; (*damping constant*)
dt=10^(-12); (*time step*)
p={5000,0,14142};(*initial magnetization*)
rs=10;
tt=5000; (*total time*)
Hk=15; (*effective anisotropy field*)
For[i=0,i tt,
 ht=h+{hrf*Cos[2Pi*f0*i*dt],0,0}+{0,0,Hk*p[[3]]/Ms}+{0,-
p[[2]],0};(*total effective field*)
 k1=g*(Cross[ht,p]+damping*Cross[p,Cross[ht,p]]/Ms);

ht1=h+{hrf*Cos[2Pi*f0*(i+0.5)*dt],0,0}+{0,0,Hk*(p[[3]]+0.5
*k1[[3]]*dt)/Ms}+{0,-(p[[2]]+0.5*k1[[2]]*dt),0};

k2=g*(Cross[ht1,(p+0.5*k1*dt)]+damping*Cross[(p+0.5*k1*dt)
,Cross[ht1,(p+0.5*k1*dt)]]/Ms);

ht2=h+{hrf*Cos[2Pi*f0*(i+0.5)*dt],0,0}+{0,0,Hk*(p[[3]]+0.5
*k2[[3]]*dt)/Ms}+{0,-(p[[2]]+0.5*k2[[2]]*dt),0};

k3=g*(Cross[ht2,(p+0.5*k2*dt)]+damping*Cross[(p+0.5*k2*dt)
,Cross[ht2,(p+0.5*k2*dt)]]/Ms);

ht3=h+{hrf*Cos[2Pi*f0*(i+1)*dt],0,0}+{0,0,Hk*(p[[3]]+k3[[3
]]*dt)/Ms}+{0,-(p[[2]]+k3[[2]]*dt),0};
```

```
k4=g*(Cross[ht3,(p+k3*dt)]+damping*Cross[(p+k3*dt),Cross[h
t3,(p+k3*dt)]]/Ms);
 p=p+1/6*(k1+2*k2+2*k3+k4)*dt;
 If[p[[3]]<0,hrf=0,hrf=0];
 If[Mod[i,rs] 0,j=i/rs;M[j]=p];
 i++]
```

## B. ANALYTICAL SOLUTION OF LL EQUATIONS

We study the dispersion relation and the relation between resonance frequency and interlayer exchange interaction in magnetic bilayer. The analytical algorithm to solve LL equations has been described in Chapter 7. Here is the Matlab code to calculate the dispersion relation.

```
syms w A12 A21 a
gama=28;% gyromangetic ratio=28GHz/T
hext=0.005;%external magnetic field 0.005 T
m1s=1.8; %saturation magnetization of the first layer 1.8
T
m2s=0.9; %saturation magnetization of the first layer 0.9
T
A=eye(4)./gama*i*w;
M1=[0,hext+m1s;-hext,0];
M2=[0,hext+m2s;-hext,0];
g=[0,-i*a*w;i*a*w,0];
M=blkdiag(M1,M2);
G=blkdiag(g,g);
J11=[0,A12*m2s;-A12*m2s,0];
J12=[0,-A12*m1s;A12*m1s,0];
J21=[0,-A21*m2s;A21*m2s,0];
J22=[0,A21*m1s;-A21*m1s,0];
J=[J11,J12;J21,J22];
Dm=M+A+J;
eqn=det(Dm)==0;
solv=solve(eqn,w);
n=70;
k=1:n;
f1=1:n;
f2=1:n;
for j=1:1:n
    A12=j*0.001;
```

```
    A21=A12;
    f1(j)=eval(solv(1));
    f2(j)=eval(solv(3));
end
```

The code to calculate the susceptibility in magnetic bilayer with interlayer exchange interaction.

```
syms w hext a A12 A21
gama=28;
m1s=0.9;
m2s=0.9;
a1=0.008;
a2=0.008;
hext=0.03;

A=eye(4)./gama*i*w;%frequency matrix
M1=[0,hext+m1s;-hext,0];
M2=[0,hext+m2s;-hext,0];
g1=[0,i*a1*w/gama;-i*a1*w/gama,0];
g2=[0,i*a2*w/gama;-i*a2*w/gama,0];
M=blkdiag(M1,M2);
G=blkdiag(g1,g2);
J11=[0,A12*m2s;-A12*m2s,0];
J12=[0,-A12*m1s;A12*m1s,0];
J21=[0,-A21*m2s;A21*m2s,0];
J22=[0,A21*m1s;-A21*m1s,0];

J=[J11,J12;J21,J22];
b1=[0;-m1s;0;0];
b2=[0;0;0;-m2s];
Dm=M+A+J;
D=Dm+G;
s=inv(D)*(b1);
ss=inv(D)*(b2);
n=100;
k=1:1:n
s1=1:1:n;
s2=1:1:n;
r11=zeros(n);
r12=zeros(n);
r13=zeros(n);
r14=zeros(n);
```

```
r21=zeros(n);
r22=zeros(n);
r23=zeros(n);
r24=zeros(n);
for m=1:1:n
    A12=-(m-1)*0.001;
    A21=A12;
for j=1:1:n
    w=j*0.1;
    s11(j)=eval(s(1));
    s12(j)=eval(s(2));
    s13(j)=eval(s(3));
    s14(j)=eval(s(4));
    s21(j)=eval(ss(1));
    s22(j)=eval(ss(2));
    s23(j)=eval(ss(3));
    s24(j)=eval(ss(4));
end
r11(:,m)=imag(-s11);
r12(:,m)=imag(-s12);
r13(:,m)=imag(-s13);
r14(:,m)=imag(-s14);
r21(:,m)=imag(-s21);
r22(:,m)=imag(-s22);
r23(:,m)=imag(-s23);
r24(:,m)=imag(-s24);
end
```